TAMPERE UNIVERSITY OF TECHNOLOGY

JUKKA-PEKKA ALANKO

PULSED AND POLARIZATION-STABILISED GaSb DISK LASERS FOR 2.0–2.35 μm WAVELENGTH RANGE

Master of Science Thesis

Examiners: Professor Mircea Guina and
D.Sc. (Tech.) Antti Härkönen
Examiners and topic approved in
the Faculty of Science and
Environmental Engineering
council meeting 3rd November 2010

ABSTRACT

TAMPERE UNIVERSITY OF TECHNOLOGY
Master's Degree Programme in Science and Engineering
ALANKO, JUKKA-PEKKA: Pulsed and polarization-stabilized GaSb disk lasers for 2.0–2.35 μm wavelength range
Master of Science Thesis, 92 pages, 3 appendix pages
May 2011
Major: Technical Physics
Examiners: Professor Mircea Guina and D.Sc. (Tech.) Antti Härkönen
Keywords: optically-pumped semiconductor disk laser, polarization selection, guided-mode resonance grating, semiconductor saturable absorber mirror, passive mode-locking

Optically-pumped semiconductor disk lasers are light sources that offer an outstanding variety of methods in controlling the emission. They are capable of producing laser radiation in power levels of tens of watts with excellent, near-diffraction limited beam, and the fundamental emission wavelength can be controlled with band gap engineering of the semiconductor material. Moreover, the laser architecture gives the opportunity to generate high-brightness visible light via nonlinear frequency-conversion and to produce ultra-short pulses through mode-locking. Due to the high-quality output beam and the flexibility in the design, this laser type is a truly interesting alternative in finding illumination for several applications.

The focus of this thesis is on research and development of semiconductor disk lasers based on gallium-antimonide (GaSb) material system. Two different kind of semiconductor lasers emitting in the near-infrared were built and characterized. It was shown that a novel grating mirror fabricated out of germanium (Ge) can be used as a partially transparent cavity mirror in a semiconductor disk laser. The polarization-selective nature of the grating resulted in controllability of the polarization direction in laser output, which is a crucial property of lasers in several applications. This indicates that small-size, easily processable low-cost gratings could be used to replace traditional, thick dielectric laser cavity mirrors in certain applications. With an enhanced design, the reflectance spectrum of the grating can be tailored to result in distinguished performance.

The other part of this work concerned the first GaSb disk laser producing femtosecond pulses. The laser was passively mode-locked with a semiconductor saturable absorber mirror. For ultra-short pulse duration measurement, an interferometric autocorrelator based on two-photon absorption was built and successfully used. In the mid-infrared wavelengths such short pulse lasers are applicable for optical clocking or as seeders for optical amplifiers and supercontinuum lasers.

TIIVISTELMÄ

TAMPEREEN TEKNILLINEN YLIOPISTO
Teknis-luonnontieteellinen koulutusohjelma
ALANKO, JUKKA-PEKKA: Pulsed and polarization-stabilized GaSb disk lasers for 2.0–2.35 µm wavelength range
Diplomityö, 92 sivua, 3 liitesivua
Toukokuu 2011
Pääaine: Teknillinen fysiikka
Tarkastajat: Professori Mircea Guina ja TkT Antti Härkönen
Avainsanat: optisesti pumpattu puolijohdekiekkolaser, polarisaation valinta, johdetun muodon resonanssi-hila, saturoituva puolijohdeabsorbaattoripeili, passiivinen muotolukitus

Laserien merkitys nyky-yhteiskunnassa on valtava puhuttaessa niin terveydenhuollosta, teollisuudesta, tietoliikenteestä kuin viihteestäkin. 50 vuodessa laserien käyttö on noussut miljardeihin kertoihin päivässä, ja kysyntä yhä tehokkaamista, hyötysuhteeltaan paremmista ja edullisemmista lasereista kasvaa alati.

Optisesti pumpatut puolijohdekiekkolaserit ovat valonlähteitä, joiden rakenne mahdollistaa tuotetun valon ominaisuuksien muokkaamisen eri tavoin. Tällaisilla lasereilla on erinomainen säteenlaatu, ne kykenevät suuren optisen tehon tuottamiseen, ja emittoidun valon aallonpituuteen pystytään vaikuttamaan puolijohteen energiatasoerojen suunnittelulla. Ulkoiseen laserkaviteettiin voidaan asettaa valon ominaisuuksia muokkaavia optisia elementtejä, minkä ansiosta voidaan tuottaa näkyvää valoa taajuusmuunnoksen avulla tai synnyttää ultralyhyitä optisia pulsseja muotolukitsemalla laser. Monipuolisten ominaisuuksiensa, erityisesti korkealaatuisen emissionsa ja suunnittelun joustavuutensa, ansiosta puolijohdekiekkolaserit ovat erittäin mielenkiintoinen tutkimuskohde etsittäessä valonlähteitä useisiin erilaisiin sovelluksiin, kuten laservalaisuun ja optiseen pumppaukseen.

Tässä työssä tutkittiin ja kehitettiin gallium-antimoni(GaSb)-materiaaleihin perustuvia, lähi-infrapuna-alueen puolijohdekiekkolasereita. Työ koostui kahdesta osasta, joista ensimmäisessä osoitettiin, että germaniumista (Ge) valmistettua hilaa voidaan käyttää puolijohdekiekkolaserin ulostulopeilinä. Hilan polarisaatiovalikoivista ominaisuuksista johtuen laservalon polarisaation suunta pystyttiin valitsemaan hilan avulla. Tämän työn pohjalta voidaan todeta, että pienikokoisilla, yksinkertaisesti valmistettavilla ja materiaaliltaan edullisilla hiloilla voidaan korvata tietyissä tapauksissa ulkoisen laserkaviteetin peileinä käytettyjä, suurikokoisia dielektrisiä peilejä. Edistyneellä suunnittelulla hilan heijastavuuskaistan leveyttä pystytään säätämään, jolloin laserissa voidaan saavuttaa aallonpituudeltaan laajalti viritettävissä oleva toiminta. Työn toinen osuus koski tiettävästi ensimmäistä kestoltaan femtosekuntiluokan pulsseja tuottavaa GaSb-kiekkolaseria, joka muotolukittiin passiivisesti saturoituvan puolijohdeabsorbaattoripeilin avulla. Ultralyhyiden pulssien mittaamiseen käytettiin itse rakennettua interferometristä, kaksifotoniabsorptioon perustuvaa autokorrelaattoria.

PREFACE

This work was carried out at the Optoelectronics Research Centre (ORC), Tampere University of Technology.

I am grateful to Dr. Pekka Savolainen, Director of ORC, for giving me the opportunity to be a part of the dynamic science community of ORC.

My greatest gratitude for completing this thesis goes to my supervisor Dr. Antti Härkönen. With your vast experience and knowledge of the field, you have given indispensable guidance and support in learning process and overcoming problems. I truly appreciate your capability to handle things on short notice. The ideas and hints you have given me regarding the renovation have also been a huge help. I want to express my sincere compliments to Prof. Mircea Guina, my other supervisor, for being such a team leader with a relaxed but incredibly efficient attitude, whether it's in the laboratory or football field. I also want to thank Dr. Petteri Uusimaa, President & CEO of Modulight, Inc., for employing me into your competitive team and for giving the final motivation to finish this thesis.

The GaSb-team of Dr. Soile Suomalainen, M.Sc. Jonna Paajaste and Riku Koskinen made this work possible by growing the semiconductor materials. The outstanding expertise of Prof. Günter Steinmeyer and Dr. Christian Grebing in pulsed light was irreplaceable indeed. I give notable credits to Prof. Tapio Niemi and M.Sc. Juha Kontio for providing the germanium grating and helping with the physical questions. Thanks to Dr. Lasse Orsila, Dr. Tomi Leinonen, M.Sc. Esa Saarinen, M.Sc. Antti Rantamäki and B.Sc. Jari Nikkinen for all-around help. In the end, a warm commendation to the whole ORC crew.

My family and friends have been a major factor in finishing the studies and reminding me of the outside world. Thanks to my parents' advice, I have learned to understand the value of both hard work and rest. I want to thank my sister Katja for proofreading this thesis. Both you and my brother Ville-Matti have been helpful in sharing ideas. I owe Tuukka and Janne for dragging me to the running trails and spectator sport sessions. My best friend and dance partner Hanna-Kaisa has been a significant person to talk to. I also acknowledge the interest of Merja and Esko towards my studies.

Most of all, I'm thankful to my dear partner Sanni for love and patience. You were the reminder that kept me going throughout this work.

Tampere, May 29th, 2011

Jukka-Pekka Alanko

CONTENTS

ABBREVIATIONS AND SYMBOLS

Abbreviations

a.u.	Arbitrary unit
AC	Autocorrelator/Autocorrelation
Ag	Silver
Al	Aluminium
AlAsSb	Aluminium arsenide antimonide
AlGaAsSb	Aluminium gallium arsenide antimonide
AlGaSb	Aluminium gallium antimonide
AR	Antireflective
As	Arsenic
Bi	Bismuth
BS	Beam splitter
c.c.	Complex conjugate
CO_2	Carbon dioxide
CW	Continuous wave
DBR	Distributed Bragg reflector
FP	Fabry–Pérot
FSR	Free spectral range
FWHM	Full width at half maximum
Ga	Gallium
GaSb	Gallium antimonide
Ge	Germanium
GMR	Guided-mode resonance
Ho	Holmium
HR	Highly reflective
IAC	Intensity autocorrelation
IFAC	Interferometric autocorrelation
In	Indium
InGaAsSb	Indium gallium arsenide antimonide
InGaSb	Indium gallium antimonide
IR	Infrared
LASER	Light amplification by stimulated emission of radiation
MBE	Molecular beam epitaxy
Nd	Neodymium
NIL	Nanoimprint lithography
NIR	Near-infrared

OC	Output coupler
OP-SDL	Optically-pumped semiconductor disk laser
OPS-VECSEL	Optically-pumped-semiconductor vertical-external-cavity surface-emitting laser
ORC	Optoelectronics Research Centre, Tampere University of technology
QD	Quantum dot
QW	Quantum well
RF	Radio frequency
RoC	Radius of curvature
RPG	Resonant periodic gain
Sb	Antimony
SESAM	Semiconductor saturable absorber mirror
SDL	Semiconductor disk laser
SHG	Second-harmonic generation
SHGA	Second-harmonic-generation autocorrelation
Si	Silicon
SiC	Silicon carbide
SiO_2	Silicon dioxide
SNR	Signal-to-noise ratio
TE	Transverse electric
TEM	Transverse electric and magnetic
TM	Transverse magnetic
TPA	Two-photon absorption
TPAAC	Two-photon absorption autocorrelation
VBG	Volume Bragg grating
VECSEL	Vertical-external-cavity surface-emitting laser
Yb	Ytterbium

Symbols, Greek alphabet

α	Absorption loss coefficient
β	Propagation constant
β_2	Group velocity dispersion paramater
δ	Phase shift
ϵ	Relative permittivity
$\Delta\epsilon$	Modulation amplitude of relative permittivity

θ	Angle
κ	Numerical factor describing pulse shape
λ	Wavelength
λ_0	Center wavelength
λ_B	Bragg wavelength
$\Delta\lambda$	Spectral width / Free spectral range
Λ	Grating period
ν	Frequency
$\Delta\nu$	Spectral width in frequency domain
$\Delta\nu_\mathrm{L}$	Full spectral width at half of maximum intensity (FWHM)
σ_A	Absorption cross section
τ_A	Saturable absorber recovery time
τ_p	Pulse repetition rate
$\Delta\tau_\mathrm{p}$	Pulse duration
ϕ	Phase
φ	Phase
φ_l	Phase of a mode l
$\chi^{(2)}$	Second-order nonlinear optical susceptibility
ω	Angular frequency / Instantaneous angular frequency
ω_0	Center frequency
ω_l	Angular frequency of a mode l
$\Delta\omega$	Frequency chirp
$\Delta\omega_\mathrm{L}$	Laser gain bandwidth (angular frequency)

Symbols, Other

A	Amplitude of electric field / Element of ABCD matrix
$\tilde{A}$	Slowly varying amplitude of an electric field
A_0	Peak amplitude of a Gaussian pulse
$\mathscr{A}$	Jones matrix
B	Element of ABCD matrix
c	Speed of light
C	Chirp factor / Element of ABCD matrix
d	Medium thickness
D	Laser cavity dimension / Element of ABCD matrix
E	Electric field
$\boldsymbol{E}$	Electric field vector
E_c	Conduction band energy

E_g	Band gap energy
E_v	Valence band energy
ΔE_c	Conduction band well
ΔE_v	Valence band well
$\mathscr{E}$	Elliptical state of polarization
f	Focal length
F_p	Pulse fluence
F_sat	Saturation fluence
$\mathscr{F}$	Finesse
g	Stability parameter of a laser cavity
h	Planck's constant
H	Hermite polynomial
I	Intensity
I_sat	Saturation intensity
$\mathscr{J}$	Jones vector
k	Wave number
$\boldsymbol{k}$	Wave vector
L	Resonator length
$\mathscr{L}$	Left-circular state of polarization
$\mathscr{M}$	Jones matrix of birefringent element
$\mathscr{M}_\mathrm{RT}$	Jones matrix for round trip in cavity
M^2	Beam quality parameter
n	Refractive index
Δn	Refractive index contrast
N	Effective refractive index of a waveguide
$\mathscr{P}$	Linear state of polarization
q	Complex radius of curvature of a spherical wave
q_0	Unsaturated power loss
r	Optical ray displacement from optical axis
r'	Angle of propagation of an optical ray, derivative of the radial displacement
$\boldsymbol{r}$	Optical ray vector
R	Reflectivity / Radius of curvature of a wave front / Rotation matrix
ΔR	Modulation depth
ΔR_ns	Non-saturable reflectivity losses
$\mathscr{R}$	Right-circular state of polarization
$\hat{S}(z)$	Amplitude of an inhomogeneous plane wave
t_p	Full width of an optical pulse

t_{SHGA}	Fringe period in second-harmonic generation autocorrelation
T_0	Width of a chirped pulse
u	Slowly varying function
w	Beam radius

1. INTRODUCTION

Lasers have a significant role in modern society when it comes to health care, industrial processing, surveillance and even entertainment. In their 50-year history, lasers have made such devices as barcode scanners and DVD-players possible and e.g. eye surgery and material processing much faster and more accurate. Despite the fact that billions of lasers are used daily, the demands to enhance laser output power, efficiency and lifetime and to simultaneously reduce both costs and size are constantly growing.

The principle of laser operation was introduced by the Charles Townes' group in 1954, when they presented microwave oscillation in ammonia [1]. The following year, in context to further results, they used the acronym MASER (Microwave Amplification by Stimulated Emission of Radiation) [2], which springs from the phenomenon of stimulated emission that was theorized by Albert Einstein in 1917 [3]. Stimulated emission occurs in an active gain medium when a photon stimulates the birth of another photon. The new photon has the same electric field and polarization as the original. In addition, the propagation direction is preserved, whereupon the radiant field emitted by a laser is coherent and parallel [4]. As the significance and possibilities of applying stimulated emission to visible wavelengths was realized, the expression LASER (Light Amplification by Stimulated Emission of Radiation) was emerged. It was used for the first time in 1957 by Gordon Gould, who published his work in 1959 [5]. There is an ongoing controversy over the very first scientist to build a laser since Theodore Maiman's article about a ruby laser [6] was published contemporarily.

The active medium is placed inside a cavity formed by two or several mirrors, which enable a standing or circulating wave between them depending on the cavity configuration. When the excited states of the gain medium decay, spontaneous emission or non-radiative recombination occurs. By reflecting these spontaneously emitted photons with the cavity mirrors back to the amplifying medium, one is able to generate stimulated emission. In order to achieve actual lasing, more atoms must be in higher energy states compared to lower, i.e. population inversion must be achieved. This is done by feeding energy into the gain medium. This pumping can be done optically or electrically and it excites atoms or charge carriers to higher energy states. Laser cavity mirrors have typically a reasonable reflectivity in order

to provide sufficient feedback and to avoid excessive losses. The eventual output is accomplished by choosing one of the cavity mirrors to be partially transparent.

Different laser types are grouped according to gain medium, which can basically be any material able to generate optical amplification. The most important ones are gas lasers, traditional solid-state lasers and fiber lasers, as well as the most common laser type, the semiconductor laser. Gas ion lasers refer to amplifying media like helium-neon, CO_2 and argon ions, and they are usually pumped with electrical discharge. Conventional solid-state lasers are based on crystals or glass material, which are doped with rare earth elements or transition metal ions, for example Nd, Ho,Yb and Bi. Fiber lasers are a special type of solid-state lasers based on optical fibers, where the total internal reflection traps the light inside the fiber waveguide. A doped fiber core acts as the gain medium, and thereby the gain region can be remarkably long, which permits the end reflection to be relatively low, and even a cleaved fiber end can provide sufficient feedback for lasing. A long fiber also acts a good channel for heat extraction. Other figures of merit for fiber lasers are good beam quality and wide gain bandwidth, which allows for wavelength tuning and ultra-short pulses.

Most common type of semiconductor lasers are laser diodes based on differently doped semiconductor layers forming a pn-junction. N-type area is named after the bulk of negatively charged electrons. Correspondingly, p-type area has a majority of vacancies for electrons, which are considered as holes (free space for an electron) and thus have a positive charge. When these n- and p-type semiconductors are brought close together, their band structures are mixed forming a depletion layer, or the active region. Due this simple composition, laser diodes are small and cheap to fabricate. Since the laser diodes can be directly controlled with current and their efficiency is good, their enormous use in consumer electronics and telecommunications has revolutionized the laser business.

One aspect in laser development is to fill existing gaps in the currently quite discrete spectral coverage. Several laser types emitting at specific wavelengths have been assorted for certain applications and in some cases the application itself has been built based on the laser availability. Semiconductor lasers jump out from the variety of different laser types with their wavelength flexibility. Band gap engineering of the semiconductor structure gives one the possibility to choose the emission wavelength within certain limits.

There are many excellent solid state and semiconductor gain materials emitting at 800–1500 nm wavelengths. Diode lasers in this near-infrared (NIR) wavelength region are inexpensive to fabricate and they are commercially available in large numbers. As NIR lasers also have a long lifetime and are capable of producing high powers, the NIR region has gained an important role in several applications in the

photonics field such as spectroscopy, sensing, surgery and telecommunications [7–13]. However, there is also a strong call in e.g. spectroscopic applications for compact lasers emitting at longer wavelengths.

In e.g. directed energy applications, distant sensing and range finding the need for high power lasers is growing firmly [14, 15]. However, beams propagating long distances in the atmosphere may experience reflections and scattering, which create the risk of eye exposure [15]. Wavelengths above 1.4 µm are considered "eye-safe", as the light is absorbed into the eye's cornea and lens, and therefore doesn't penetrate into the eye and cause "blind spots" by damaging the retina [16]. The objective of this thesis is to study semiconductor disk lasers based on GaSb material system and emitting at the eye-safe region, of 2.0–2.35 µm to be exact. The concept of Optically-Pumped Semiconductor Disk Laser (OP-SDL) used in this thesis is introduced in chapter two, where the fundamental elements and characteristic properties of this laser type are discussed. The main focus of the chapter is on the issues important in experimental performance.

Two different experimental setups were studied in this work. The other one was a polarization-stabilized laser that combines the features of stable linearly-polarized and single-mode emission. These properties of light are vital within applications mentioned earlier. In addition, the motivation to miniaturize optical components is invariably growing, and therefore the setup was realized with the use of a novel grating structure, whose polarization- and reflectivity related properties will be discussed in chapter three. In chapter four one becomes acquaint with pulsed lasers. The methods to achieve pulsed operation and the principle and a description of adjustment of a device used to measure short pulses, an optical autocorrelator, are introduced. Chapter four aims to be an introductory to the other setup, the very first femtosecond passively mode-locked laser based on GaSb material system [17].

Chapter five is devoted to experimental results and, finally, chapter six summarizes the achieved results and considers further development in the field and studied matters themselves.

2. SEMICONDUCTOR DISK LASER

2.1 Introduction

Optically-pumped semiconductor disk laser (OP-SDL) or optically-pumped-semiconductor vertical-external-cavity surface-emitting laser (OPS-VECSEL) utilizes, as the latter term implies, the use of external cavity mirrors to provide feedback to a surface emitting gain medium as illustrated in Figure 2.1. Effectively the gain mirror resembles a thin multilayer disk, from which the name SDL originates. OP-SDLs were demonstrated already in the early 1990's, when Le et al. published their work on an optically pumped semiconductor laser, in which a bulk GaAs wafer was placed between external mirrors [18]. Coincidently, Jiang et al. reported how they had provided the feedback by assembling a gold coating underneath a multiple quantum well gain material [19]. Laser emission required intense cooling to temperature of 77 K. In 1997, the first high power, multiple quantum well SDL operating at room temperature was presented [20].

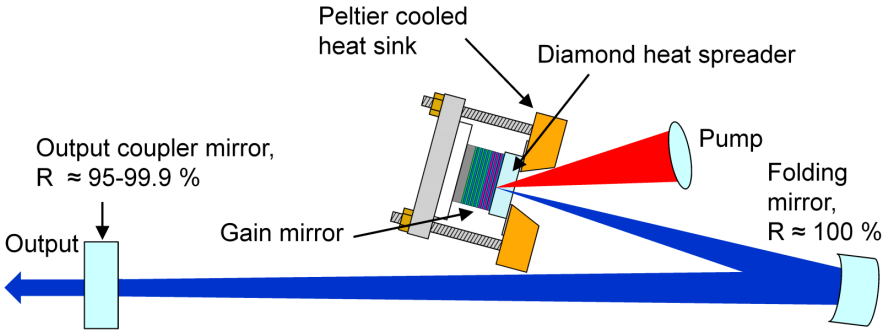

Figure 2.1: Example of a semiconductor disk laser. The pump light is focused onto the gain region to provide energy for the amplification of cavity light. The external cavity is formed between the gain mirror and the dielectric mirrors.

Optical pumping is a beneficial method, since the pump diode laser technology is advanced and economical, the spatial distribution of charge carriers created on the gain medium is uniform, and no absorption-increasing doping is required. In addition, the pumped gain area can be enlarged, which results in power scaling up to tens of watts. In edge-emitting lasers power levels of hundreds of watts can be reached by increasing the stripe width, but such bar-based lasers are strongly multimodal. In an SDL, high powers are achievable simultaneously maintaining single-

or near single-mode operation, since the cavity geometry gives one the possibility to adjust the fundamental transversal laser mode of the cavity to match the pump spot size. Moreover, the SDL concept enables single-frequency and ultra-short pulse operation [21]. The wavelength and line width can be tuned with intra-cavity elements, which enables adjusting laser behaviour accurately. For example, by placing a nonlinear crystal inside the external cavity, the laser emission can be frequency doubled through second-harmonic generation [22]. With a birefringent filter the wavelength can be tuned in a wide range [23], and by exploiting a volume Bragg grating (VBG) as an output coupler, narrow-band operation at a fixed wavelength can be achieved [24].

2.2 The state of the art

In two decades, SDL research and development has been active and the threshold of commercialization has already been crossed. So far, SDLs have been reported to operate at different wavelengths in the range 338–5000 nm [23, 25–28]. This work concentrates on the GaSb material system, and the current GaSb-SDL wavelength range is enumerated in Table 2.1.

GaSb-based material system has been studied during the recent years in growing numbers because it can cover the spectral band 1.6–6.1 µm [42–47]. Edge-emitting, high power diode lasers at these wavelengths have been fabricated, but their demerit is the elliptical output beam with poor quality [48]. It has already been demonstrated that GaSb-based SDLs operating at around 2 µm can exhibit multi-watt, continuous wave (CW) output power and broad tunability [30]. With molecular beam epitaxy (MBE, will be discussed in subchapter 2.3.3) high quality devices in the range 2.0–2.9 µm can be manufactured [49].

Actively mode-locked operation in a GaSb disk laser has been achieved [50], but to the best of my knowledge, prior to this work ultra-short, sub-picosecond pulses in this wavelength range obtained by passive mode-locking have not been demonstrated. One of the reasons for the slow progress is the lack of suitable semiconductor saturable absorber mirrors (SESAMs) in this wavelength range. In this work the aim was to study new, fast GaSb-based SESAMs in order to mode-lock GaSb disk lasers and reach ultra-short pulse operation.

Table 2.1: GaSb-SDL: state of the art

Wavelength (nm)	Output power (W)	Operating temperature (°C)	Year	Notes
1.902–2.056	Max. 1.2	-15–30	2008 [29]	Tunable
1.924–2.080	Max. 0.4	10–15	2009 [30]	Tunable
1.947–2.026	Average > 1	15	2008 [31]	Tunable
1.97	3.6	Room temp.	2009 [30]	
1.97	4.2	10	2009 [30]	
2.02	6.0	-15	2008 [32]	
2.02	3.3	21	2008 [32]	
2.1	N/A	27	2003 [33]	
2.25	3.3	20	2009 [34]	Two gain elements
2.25	3.4	-10	2008 [35]	
2.25	1.7	20	2008 [32]	
2.3	1.5	-20	2007 [36]	
2.3	0.35	15	2007 [37]	
2.3	1.7 (Peak)	Room temp.	2007 [38]	Pulsed pump
2.34	0.0015	15	2010 [39]	Electrically pumped
2.35	>3	-15	2008 [32]	
2.35	3.2	-15	2007 [40]	In-well pumped
2.35	0.2	10	2007 [41]	
2.35	2	15	2007 [40]	In-well pumped
2.8	0.12	20	2008 [32]	

2.3 Elements of a semiconductor disk laser

The heart of an SDL is the gain mirror, which is an integrated ensemble of the emission producing active medium and a low-loss mirror providing feedback. A schematic structure of a gain mirror is presented in Figure 2.2, and the following subchapters give a principled description on the SDL components and their fabrication.

2.3.1 Distributed Bragg reflector

To enable high reflectivity and efficient feedback to the other end of the gain medium, a Distributed Bragg reflector (DBR) can be used. DBR is a multilayer thin film structure that can be grown on the substrate prior to the gain medium in the same epitaxial process as the rest of an SDL gain mirror.

In an SDL, the DBR is typically processed out of transparent semiconductor layers with an optical thickness of a quarter of the target wavelength λ. Optical thickness is defined as the product of refractive index n and the physical thickness d of the medium, which thus results in [4]

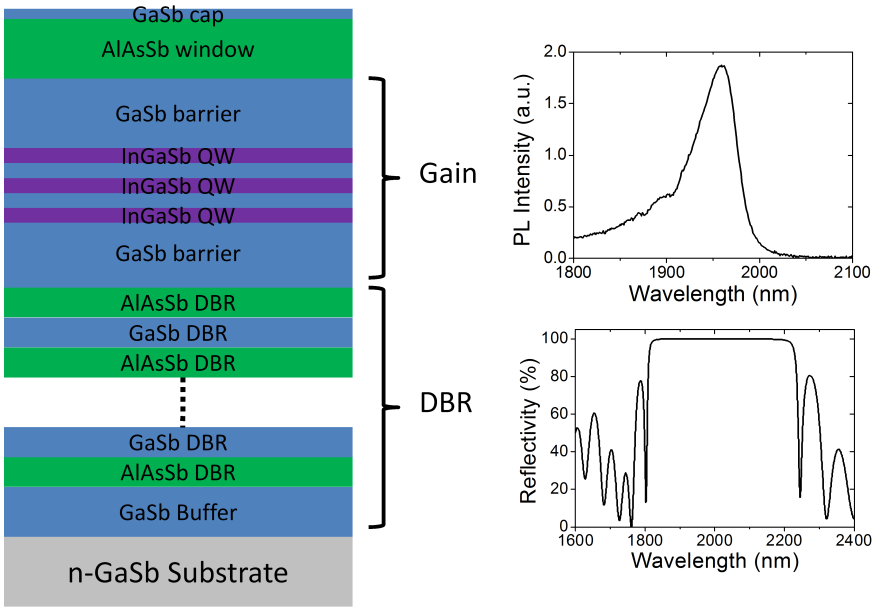

Figure 2.2: Structural layers of an SDL gain mirror. The gain region provides a photoluminescence illustrated in the upper spectral figure. The lower spectrum presents the reflectivity design of the feedback mirror. Courtesy of Antti Härkönen.

$$d = \frac{\lambda_{\mathrm{B}}}{4n\left(\lambda_{\mathrm{B}}\right)}, \tag{2.1}$$

where $n\left(\lambda_{\mathrm{B}}\right)$ is the refractive index of the layer at Bragg wavelength i.e. target wavelength of the maximum reflectivity. The films have alternating high (n_{H}) and low (n_{L}) refractive indices, whereupon the incident light is Fresnel reflected at each interface.

The principle level structure of a DBR is represented in Figure 2.3. As each optical path between reflections from adjoining interfaces corresponds to $\lambda/2$, a 180°phase shift is induced at each reflection. In addition, due to the refractive index contrast, the phase of the incident light experiences another 180°phase shift when passing from a low index layer to high index layer, and no phase shift in the contrary situation. Therefore, all the reflected beams will interfere constructively at the front surface, which results in high reflectivity [51].

Since in an SDL the DBR end of the cavity is not desired to have output, the reflectivity should be as high as possible to minimize losses. Theoretically 100 % reflectivity is possible, and as high as 99.99984 % reflectivities have been reported [52].

The DBR reflectivity depends on the amount of the thin films N, index contrast $\Delta n{=}n_{\mathrm{H}}{-}n_{\mathrm{L}}$ and the refractive indices of the semiconductor substrate n_{S} and the surrounding medium n_{i}. The respective reflectivity formulae for even number of layers and for odd number of layers are [53]

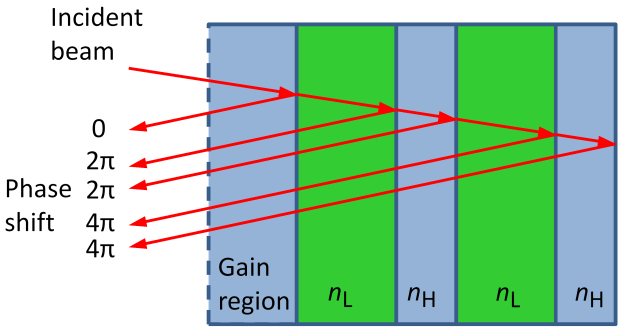

Figure 2.3: Principle of a distributed Bragg reflector. The reflected waves experience a phase shift of multiple of 2π and interfere constructively.

$$R_{\mathrm{DBR,odd}} = \left(\frac{1 - \left(\frac{n_\mathrm{S}}{n_\mathrm{i}}\right)\left(\frac{n_\mathrm{H}}{n_\mathrm{L}}\right)^{2N}}{1 + \left(\frac{n_\mathrm{S}}{n_\mathrm{i}}\right)\left(\frac{n_\mathrm{H}}{n_\mathrm{L}}\right)^{2N}} \right)^2 \tag{2.2}$$

and

$$R_{\mathrm{DBR,even}} = \left(\frac{1 - \left(\frac{{n_\mathrm{H}}^2}{n_\mathrm{i} n_\mathrm{S}}\right)\left(\frac{n_\mathrm{H}}{n_\mathrm{L}}\right)^{2N}}{1 + \left(\frac{{n_\mathrm{H}}^2}{n_\mathrm{i} n_\mathrm{S}}\right)\left(\frac{n_\mathrm{H}}{n_\mathrm{L}}\right)^{2N}} \right)^2 . \tag{2.3}$$

Ultimately the DBR reflectivity is limited by the number of layers. This is due to the stack thickness, which is sensible to be kept within certain practical limits as increasing strain in the semiconductor crystal lattice is undesired due to the risk of thermal relaxations and lower damage threshold.

The reflectivity band is limited to a certain width, which is determined by the index contrast according to the following equation [23]:

$$\Delta\lambda < 4\frac{\lambda_\mathrm{B}}{\pi} \arcsin\left(\frac{n_\mathrm{H} - n_\mathrm{L}}{n_\mathrm{H} + n_\mathrm{L}}\right). \tag{2.4}$$

Figure 2.4 presents the simulated DBR reflectivity of the 2.0 µm gain mirror used in this work. The simulation shows typical typical shape of the reflectivity curve with a highly reflective stopband and multiple side peaks. The structure of the DBR can be found in Appendix A.

The different alloys forming the DBR structures used in this work have a large index contrast of ∼1.2 in the 2.0–2.7 µm wavelength range, and therefore a highly reflective DBR can be fabricated with a small number of ∼20 pairs [54].

2.3.2 Gain structure

The energy band theory is used to describe the electronic states of semiconductor materials. The energy levels can be considered to be divided into forbidden and

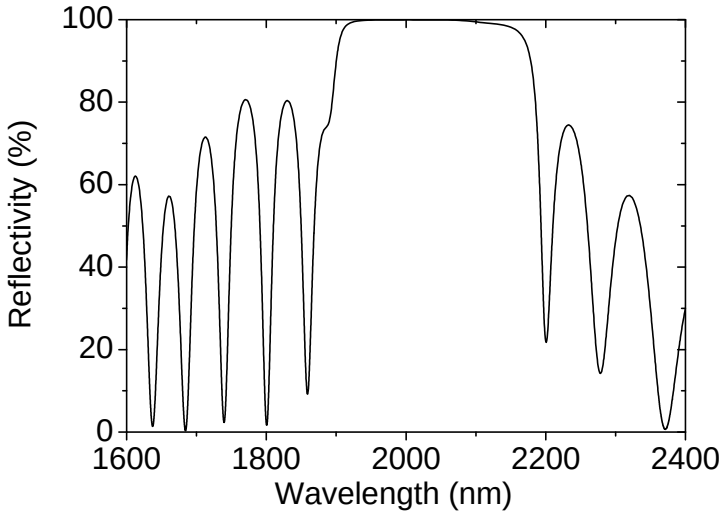

Figure 2.4: Simulated reflectivity spectrum of a DBR designed for wavelength 2.0 µm. Courtesy of Jonna Paajaste.

allowed bands. In semiconductor physics, the energy band filled with electrons is called the valence band, and the empty band, which is higher at energy, is called the conduction band. The energy separation between these bands is called the band gap energy E_g.

The behaviour of different types of solids in terms of temperature clarifies the origin of the term 'semiconductor'. The electrical conductivity of metals arises from the conduction band inhabited by electrons. Insulators, on the other hand, have a high band gap and thus an empty conduction band at all temperatures. Similarly, semiconductors act as insulators at zero kelvin. However, as the temperature rises, electrons can be excited from the valence band to the conductivity band due to the low band gap energy of the semiconductors. This process creates two charge carriers: the excited electron with a negative charge in the conduction band, and the hole considered as a positive charge left in the valence band. [55]

The excitation of electrons from the valence band to the conduction band can also be done optically, which is the idea in optical pumping of SDLs. Under intense optical pumping the occupation of the conduction band exceeds that of the valence band, and population inversion is achieved. As mentioned in chapter 1, this allows the gain medium to act as an optical amplifier. In a semiconductor laser cavity, the electron-hole pairs recombine through stimulated emission and a photon with energy corresponding to the band gap is emitted at a wavelength λ defined by the band gap energy [4]:

$$\lambda = \frac{c}{\nu} = \frac{hc}{E_g}, \tag{2.5}$$

where c is the speed of light, ν is frequency and h is Planck's constant.

The gain structures used in this work consist of quantum wells (QWs), which are composed of a very thin layer of semiconductor material with a small band gap E_{g1} between two barrier layers of larger band gap E_{g2} as illustrated in Figure 2.5. Due to the difference in band gap energies, the charge carriers are confined in potential wells of the QWs, namely valence-band well ΔE_v for the holes and conduction-band well ΔE_c for the electrons [4].

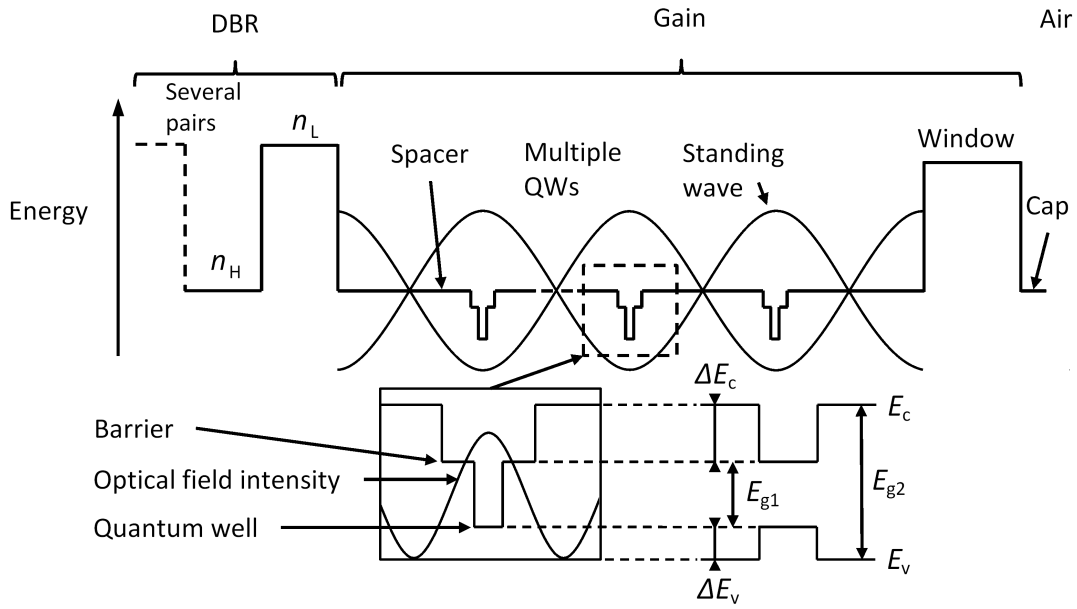

Figure 2.5: The structure of an SDL gain mirror. The illustration above is the conduction band energy profile and the one below shows the quantum well structure with respect to energy levels and the optical field intensity.

In laser operation, a standing wave is generated into the SDL gain region, which forms a Fabry–Pérot (FP) resonator between the DBR and the air boundary. This optical resonator is also called micro-cavity. In order to maximize the confinement factor [56] and the gain efficiency [57], the quantum well positions are aligned at the antinodes of the standing wave. Such a resonant periodic gain (RPG) structure is achieved using spacer layers so that the QWs overlap with the optical field maxima [56]. A window layer, which is designed to be transparent at both the pump and laser wavelength and has a large band gap on top finishes the gain mirror entity. The purpose of the window is to prevent charge carriers from drifting to gain medium surface, which would result in surface recombination and losses. Also a cap layer can be grown on top to protect the window from surface oxidation [58, 59]. A gain mirror formed of QWs is illustrated in Figure 2.5. Also quantum dots (QDs) [60] or bulk material [18] can be used as the active region of an SDL.

2.3.3 Fabrication

The gain mirrors used in this work were grown at ORC by molecular beam epitaxy, which is based on deposition of atomic layers in ultra-high vacuum of about 10^{-9} mbar in pressure. In this epitaxial growth process the lattice structure of an atomic layer is copied into that grown on top of the original. The vacuum is necessary to avoid impurities and to achieve high crystal quality. The materials for multi-layer structures are heated to point where they sublimate. Each material is in a separate containers, and the material flows or molecular beams are directed on the heated substrate. The thickness of each layer is controlled with shutters. [61, 62]

2.4 Cavity design

The simplest case of a laser cavity with two parallel plane mirrors corresponds to a Fabry–Pérot resonator with a highly reflective end and a partially transparent end mirror. In an SDL, DBR forms the highly reflective end, but the output coupler mirror, e.g. a dielectric mirror, is usually concave to provide stability to the cavity design as presented in Figure 2.6.

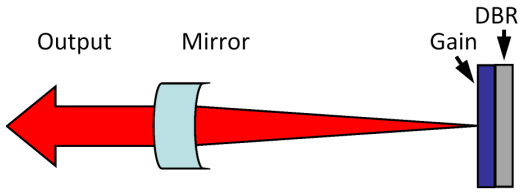

Figure 2.6: A simple laser cavity with a highly reflective DBR immediately after the active gain region, and a partially transparent external cavity mirror.

The electric field propagating inside a laser cavity satisfies the wave equation, and each solution is called a mode, which is determined by the cavity properties. The existence of the modes is possible only if the optical rays stay inside the cavity after N round trips i.e. the cavity is stable. The modeling of the fundamental transversal mode diameter and the external cavity stability in this work were performed using a commercial software WinLase Professional 2.1. It uses ray vectors and ABCD matrix formalism to describe the cavity properties. Using the software makes the cavity design process easy, since the theoretical mode diameter can be calculated and matched to the pump spot size. Usually the simulated cavity properties are found to be quite close to optimal also in practice, and thus the final cavity optimization can be done by slightly moving the cavity mirrors around their simulated positions.

2.4.1 Ray optics

The ABCD formalism is valid under paraxial ray approximation, which means that the direction of propagating rays inside the cavity is more or less parallel to the optical axis and that the small angle approximation $\sin\theta \approx \tan\theta \approx \theta$ holds. With this approximation, any optical system can be described by an ABCD matrix. [4]

Let us consider a propagating, approximately paraxial ray with a displacement r with respect to optical axis as illustrated in Figure 2.7. The derivative of the radial displacement corresponds to the angle of propagation θ with respect to optical axis. Since the small angle approximation can be applied, the derivative of the radial displacement becomes

$$\theta = \frac{\mathrm{d}r}{\mathrm{d}z} \approx r'. \tag{2.6}$$

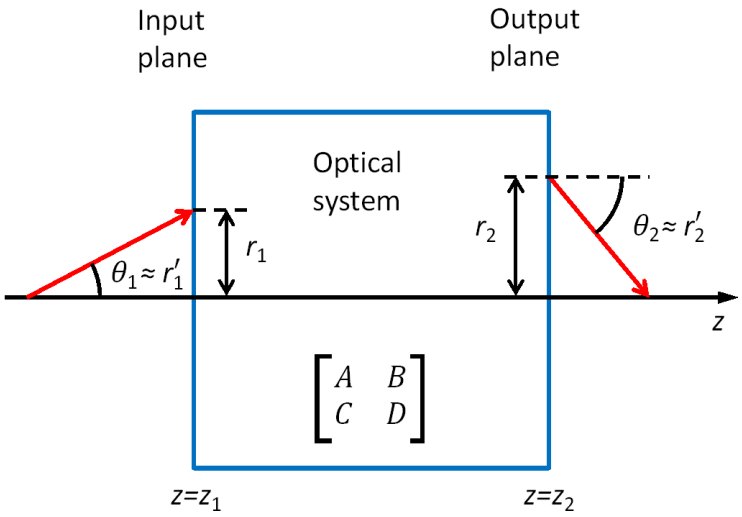

Figure 2.7: An optical element described with an ABCD matrix.

Therefore, an optical ray at the input plane $z = z_1$ of an optical element is defined as [63]

$$\boldsymbol{r}(z_1) = \boldsymbol{r}_1 = \begin{bmatrix} r_1 \\ r_1' \end{bmatrix}, \tag{2.7}$$

where r_1 and r_1' are the radial displacement and the propagation angle of the ray with respect to optical axis, respectively. When the ray propagates through an optical system, the output ray is given as a matrix product

$$\begin{bmatrix} r_2 \\ r_2' \end{bmatrix} = \begin{bmatrix} A & B \\ C & D \end{bmatrix} \begin{bmatrix} r_1 \\ r_1' \end{bmatrix} \tag{2.8}$$

with the assumption that the paraxial approximation still holds after the optical element.

If the laser cavity is characterized with an ABCD matrix, the ray vector after n round trips is [4]

$$\begin{bmatrix} r_n \\ r'_n \end{bmatrix} = \begin{bmatrix} A & B \\ C & D \end{bmatrix}^n \begin{bmatrix} r_1 \\ r'_1 \end{bmatrix}. \tag{2.9}$$

The resonance cavity will be stable only if the matrix

$$\begin{bmatrix} A & B \\ C & D \end{bmatrix}^n \tag{2.10}$$

does not diverge. This condition requires the inequality [4]

$$-1 < \frac{A+D}{2} < 1 \tag{2.11}$$

to hold.

2.4.2 Wave optics

If the paraxial wave approximation is applied to a diffractively propagating wave, the electric field is defined as [4]

$$\tilde{E}(x,y,z) = u(x,y,z)\exp(-jkz), \tag{2.12}$$

where u is a slowly varying function on the wavelength scale and k is the wave number (for optical waves propagating in one dimension, the magnitude of the wave vector $\boldsymbol{k}$ is called the wave number). The solution for this electric field is given by the paraxial wave equation [4]

$$\left(\frac{\partial^2}{\partial x^2} + \frac{\partial^2}{\partial y^2}\right) u - 2jk\frac{\partial u}{\partial z} = 0. \tag{2.13}$$

A generalized solution in integral form for this electric field propagating from an input plane described by Cartesian coordinates x, y, z into output plane x_1, y_1, z_1 through an optical element characterized by an ABCD matrix is provided by [4]

$$\begin{aligned} u(x,y,z) = &\frac{j}{B\lambda}\iint_{\mathrm{S}} u(x_1,y_1,z_1)\cdot \\ &\exp\left[-jk\frac{A({x_1}^2+{y_1}^2)+D(x^2+y^2)-2x_1x-2y_1y}{2B}\right]\mathrm{d}x_1\,\mathrm{d}y_1. \end{aligned} \tag{2.14}$$

If it is assumed that there are no limiting apertures smaller than the transversal

mode diameter of the wave, an eigensolution for the equation 2.14 can be obtained by directly substituting a Gaussian function into the equation. This solution retains its functional form during propagation through the optical system, and it takes the form

$$u(x_1, y_1, z_1) \propto \exp\left(-jk\frac{{x_1}^2 + {y_1}^2}{2q}\right), \tag{2.15}$$

where $q = q(z)$ is the complex parameter describing the complex radius of curvature of a spherical wave. It is defined as [4]

$$\frac{1}{q} = \frac{1}{R} - j\left(\frac{\lambda}{\pi w^2}\right), \tag{2.16}$$

where $R = R(z)$ and $w = w(z)$ being the radius of curvature and the radius of the beam, respectively. To be exact, radius of the beam w is defined as the beam radius corresponding to $\frac{1}{e^2}$ of the maximum intensity of the beam (at the center).

At the output plane of the optical system the Gaussian beam becomes [4]

$$u(x, y, z) = \frac{1}{A + \frac{B}{q_1}} \exp\left(-jk\frac{x^2 + y^2}{2q}\right), \tag{2.17}$$

where q and q_1 fulfill the equation

$$q = \frac{Aq_1 + B}{Cq_1 + D}. \tag{2.18}$$

For a stable cavity $q = q_1$ after each round trip. Using this equality in equation 2.18 yields

$$Cq^2 + Dq - Aq - B = 0. \tag{2.19}$$

Roots for this equation are [64]

$$\frac{1}{q} = \frac{D - A}{2B} - \frac{j}{2B}\sqrt{4 - (A + D)^2}. \tag{2.20}$$

WinLase defines the stability of a laser cavity as [65]

$$g = 1 - \left(\frac{A + D}{2}\right)^2, \tag{2.21}$$

and with formalism a stable cavity has a value $g = [0, 1]$ with higher values donating increasing stability. Values close or equal to unity are desired, since in that case the modes are less sensitive to perturbations such as thermal lensing. This is directly related to the flexibility in changing cavity parameters mentioned in subchapter 2.1, such as arm lengths. This makes the cavity alignment relatively easy.

Providing that the ABCD matrix of an optical system is known, by using the equations 2.16 and 2.20 the radius of curvature and radius for the beam can be calculated.

2.4.3 Laser modes

Longitudinal modes

If a standing wave is formed between the resonator ends, the emission wavelengths of the laser match to the resonator dimensions by relation

$$\lambda = \frac{2L}{m}, \tag{2.22}$$

where m is a positive integer and L is the resonator length. The corresponding frequencies of this oscillation are called longitudinal modes, which are defined by [4]

$$\nu = m\left(\frac{c_0}{2nL}\right), \tag{2.23}$$

where c_0 is the speed of light in vacuum and n is refractive index of the resonator. The spacing between two such consecutive longitudinal resonance frequencies in the angular frequency domain is [66]

$$\Delta\omega = 2\pi\Delta\nu = \pi\frac{c_0}{nL} \tag{2.24}$$

where $\Delta\nu$ is the frequency spacing between the resonance frequencies.

Laser emission doesn't cover every possible wavelength defined in equation 2.22, but consists always of a range of specific wavelengths, which are determined by the laser's gain bandwidth as illustrated in Figure 2.8.

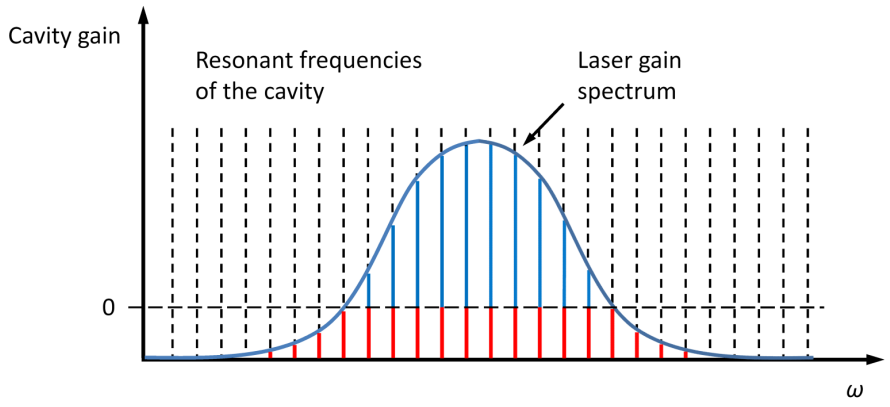

Figure 2.8: Longitudinal modes of an SDL. Blue lines inside the gain spectrum envelope represent the laser's longitudinal modes. Red lines underneath them illustrate the resonance frequencies in the cavity that are not provided with sufficient gain and do not lase.

Let us assume that there are $2n$ longitudinal modes in the gain spectrum. If a uniform amplitude distribution is assumed (usually the distribution is Gaussian), the time-dependent electric field associated with a mode is given as [4]

$$E_l(t) = E_0 \exp(j\omega_l t) \exp(j\varphi_l(t)), \tag{2.25}$$

where E_0 is the constant amplitude for all values of l, ω is the angular frequency and φ_l the respective phase of the mode.

From equation 2.24 one can obtain the angular frequency for mode l as

$$\omega_l = \omega_0 + l + \Delta\omega. \tag{2.26}$$

The total electric field associated with all the longitudinal modes inside the cavity is given as a superposition of the electric fields described in equation 2.25:

$$E(t) = \sum_{l=-n}^{n} = E_0 \exp\left[j\left(\omega_0 + l\Delta\omega\right)t\right] \exp\left(j\varphi_l(t)\right), \tag{2.27}$$

where ω_0 is the central frequency of the gain spectrum. If there is no coherence between the phases of different modes and the laser is in CW operation, the total field intensity is defined as [67]

$$\begin{aligned} I \sim < |E(t)|^2 > &= \sum_{l,m} {E_0}^2 < \exp\left[i(\varphi_l - \varphi_m)\right] > \exp\left[(i(l-m)\Delta\omega t)\right] \\ &= \sum_{l} {E_0}^2 + \sum_{l \neq m} {E_0}^2 < \exp\left[i(\varphi_l - \varphi_m)\right] > \exp\left[i(l-m)\Delta\omega t\right]), \end{aligned} \tag{2.28}$$

where the notation <> is the stochastic average. Since the nature of the term $\varphi_l - \varphi_m$ is random due to uncorrelated phases, the last exponential in equation 2.28 tends to zero and the total intensity is thus given by [67]

$$I \sim (2n+1){E_0}^2, \tag{2.29}$$

where the integer $2n+1$ refers to the total number of longitudinal modes.

Transversal modes

The eigensolution 2.17 is not the only complex solution for equation 2.14. Other useful solutions can be obtained with the product of a Hermite polynomial and the Gaussian function with the complex beam parameter q_1 [4]:

$$u(x_1, y_1, z_1) = H_l\left(\frac{\sqrt{2}x_1}{w_1}\right) H_m\left(\frac{\sqrt{2}y_1}{w_1}\right) \exp\left(-jk\frac{{x_1}^2 + {y_1}^2}{2q}\right), \tag{2.30}$$

where H_l and H_m are Hermite polynomials of order l and m, and w_1 is the beam radius. Substituting equation 2.30 into 2.14 to replace $u(x_1, y_1, z_1)$, the result is [4]

$$u(x, y, z) = \left(\frac{1}{A + \frac{B}{q_1}}\right)^{1+l+m} H_l\left(\frac{\sqrt{2}x}{w}\right) H_m\left(\frac{\sqrt{2}y}{w}\right) \exp\left(-jk\frac{x^2 + y^2}{2q}\right), \tag{2.31}$$

where q is the complex beam parameter after the optical system given in 2.18, and w is the corresponding beam radius.

Note that integer m in equations 2.22 and 2.31 refers to different properties of the electric field. In equation 2.22, m determines the field nulls of the standing wave along the resonator axis. Transverse modes on their behalf are defined by variations of the electric and magnetic field in the transversal direction. For example, the resonant frequencies of a symmetric confocal resonator are [4]

$$\nu_{lmn} = \frac{c}{4L}\left[2n + (1 + l + m)\right], \tag{2.32}$$

where c is the speed of light, L is the resonator length and l, m an n are integers that specify a mode.

It should be noted that the terms longitudinal and transverse modes do not refer to the existence of two different type of modes, but to the directions, in which the fields of an electromagnetic wave fluctuate. In the presentation represented in equation 2.32, each resonant frequency associated with a particular value of n corresponds to field variations in the axial direction (resonator axis) and thus a longitudinal mode. Correspondingly, a transversal mode stands for field changes in the transversal direction, and the equivalent resonant frequency is associated with values of l and m. The lowest order transversal mode ($l = m = 0$) has no components of electric or magnetic fields in the direction of propagation and it is called TEM_{00} (transverse electric and magnetic). It corresponds to a Gaussian beam and is a single circle in profile. Any other transversal mode is called a higher order mode.

Figure 2.9 represents some usual higher order transversal modes. Such beam profiles are a simple way for rough evaluation of the beam quality of a laser. However, a single look at the beam profile does not give the whole truth, since a beam looking like TEM_{00} can in fact be a superposition of several transverse modes and still have a Gaussian profile.

The actual beam quality can be determined by measuring the M^2 value, which

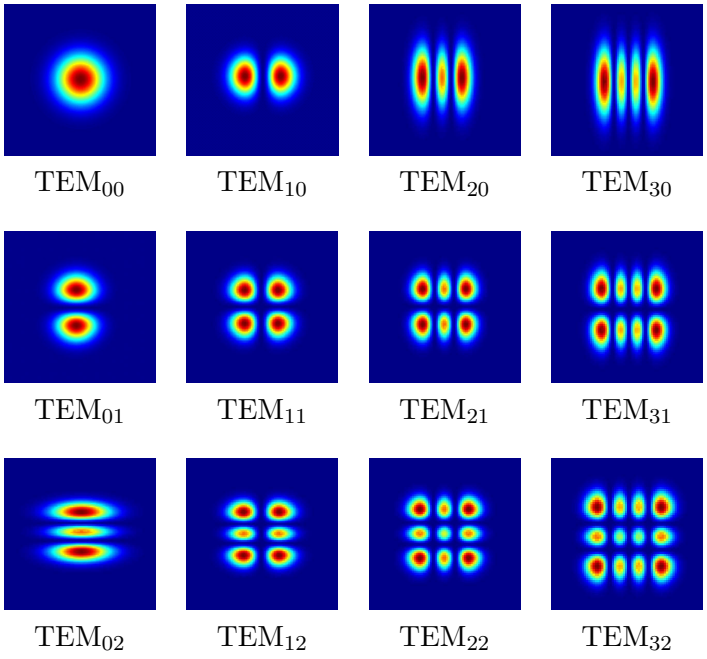

Figure 2.9: Different transversal laser modes simulated with MATLAB.

is a figure of merit describing the factor that the beam is above diffraction limit. The beam radius (transverse size of the beam spot) w_x of an arbitrary laser beam evolves in free-space propagation as [68]

$$w_{\mathrm{x}}{}^2(z) = w_{0\mathrm{x}}^2 + M_{\mathrm{x}}^2 \left(\frac{\lambda}{\pi w_{0\mathrm{x}}}\right)^2 (z - z_{0\mathrm{x}})^2, \tag{2.33}$$

where $w_{0\mathrm{x}}$ is the minimum beam radius at $z = z_{0\mathrm{x}}$. With the value of $M^2 = 1$, equation 2.33 describes the free-space propagation of diffraction-limited Gaussian beam. Figure 2.10 demonstrates the physical interpretation of M^2 value.

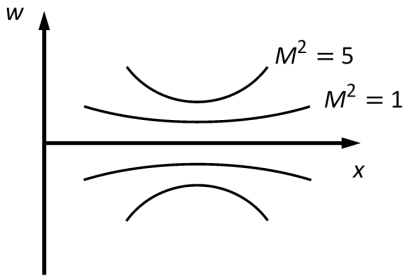

Figure 2.10: Radius of a focused laser beam as a function of distance. $M^2 = 1$ corresponds to a diffraction-limited beam, while with a value of $M^2 = 5$ the beam waist is larger and the divergence is much stronger.

Evaluating the M^2 value is done by measuring the radius of a focused beam at a few locations along the beam waist. By fitting the data to equation 2.33, one can derive values for the M_{x}^2 factor, the waist radius $w_{0\mathrm{x}}$ and its location $z_{0\mathrm{x}}$. No M^2

measurements were taken in this work.

While accurate M^2 measurements can be very time consuming, a quick way to asses the beam quality is to carefully tilt the output coupler mirror of the cavity, whereupon the transformation from TEM_{00} to higher transversal modes is easily observed in the beam profile. If a fierce tilt results only in a smooth termination of lasing, the laser can fairly be regarded operating close to a single mode.

2.5 Thermal management

Temperature is an important factor in semiconductor disk laser performance, since the peak of the gain spectrum and the position of the micro-cavity resonance are strongly dependent on temperature [69]. The pump radiation is typically absorbed into QWs, barriers and spacers and the pump wavelength needs to be shorter than the laser wavelength so that the pump photons have enough energy to excite charge carriers. The energy difference between the pump and laser photons is known as the quantum defect. This difference in photon energy is transferred to phonons, which heats the gain region. All the non-radiative processes, like Auger recombination, contribute to heating. Excess heating results in reduced carrier confinement and decrease in the band gap energy, which causes the QW emission to shift to longer wavelengths. Other effects of the temperature elevation are an increase of the gain material refractive index and also a minor thermal expansion, which lengthens the micro-cavity. Therefore, according to equation 2.23, the resonance frequencies of the micro-cavity become smaller. In addition, both the center frequency of the DBR and the resonant frequency of the resonant periodic gain experience a shift. Since these spectral shifts are likely not to compensate each other, the quantum wells' emission moves away from the peak gain spectrum and eventually thermal roll-over happens [70].

Temperature rise also causes carriers to leak out of the confining QWs, which reduces the amount of population inversion and gain, and they are more likely to recombine non-radiatively [8,21]. At threshold powers spontaneous recombination is the dominant process for carrier loss, but at higher temperatures Auger recombination takes over [71]. In addition, as the Auger recombination increases as band gap energy decreases [72–74], this process a significant factor in long wavelength lasers' performance. Moreover, the temperature profile in the gain medium isn't uniform and this leads to different refractive indices causing a thermal lens, which has an influence on the mode selection and stability of the cavity [75, 76].

It is a fact that extra heat on the gain mirror is generated, so an effective method for heat extraction from the sample is necessary in SDLs aiming for high performance. In this work, the sample was attached to a copper mount of approximately $50\times50\times4$ mm^3 in size. The idea for the copper plate is to act as a heat sink, from

which the heat is transferred further by e.g. a thermoelectric cooler. In this work, a Peltier-element was used to extract heat into an aluminum piece with channels for circulating water. However, since the gain chip dimensions are so small, an effective channel is required for efficient heat removal from the point source under optical pumping. Table 2.2 compares the thermal conductivities of some materials. It shows that transparent materials, such as silicon carbide (SiC) and diamond, are excellent heat conductors, whereupon they are widely used as heat spreaders [77].

Table 2.2: Thermal conductivities for different materials

Material	**Thermal conductivity** $\left(\frac{\mathbf{W}}{\mathbf{mK}}\right)$	**Reference**
GaAs	45.5	[78]
GaSb	37.8	[78]
Ge	60.6	[78]
Stainless steel	18–27	[79]
Copper	391–400	[79]
Sapphire	50	[80]
SiC	400	[81]
Diamond, natural IIa	2190	[82]
Diamond, synthetic , enriched with 0.5 % ^{13}C	2600	[82]

In addition to decrease in laser performance also physical damage incurred by excessive temperature rise is possible. Due to heat expansion, the gain mirror dimensions change with temperature. If pumping is initiated with already high powers, and as the gain chip is relatively small channel for watt-level heat transfer, the thermal shock can be too strong, which may in some cases result in cracks and defects on the sample. Therefore, moderate adjustment of pump levels is essential.

2.5.1 Intra-cavity diamond

Intra-cavity heat spreader approach is a method based on the fact, that the closer the heat transferring channel is to the heated area, the more effective the heat extraction is. As presented in Figure 2.11, the diamond heat spreader is placed on the top surface of the gain region, where most of the heat is generated. The bonding process is rapid. The diamond is placed on a copper mount to encompass the circular aperture of about 1.5 mm in diameter. Capillary bonding [83] is used to attach the gain mirror into the heat spreader, which is done by pipetting a drop of water or other suitable liquid with a high surface tension on the diamond. Then the gain mirror is placed on top of the diamond, and the surface tension of the liquid pulls the surfaces into close contact. The structure is completed by pressing the gain

chip to the copper heat sink with a metal clamp, when capillary action in the liquid pulls the surfaces together by Van der Waals force. Indium foil is placed between the copper mount and the diamond surrounding the aperture, and teflon sheet is used in between the gain chip and the metal clamp in order to balance the pressure throughout the gain chip area and to avoid mechanical damage.

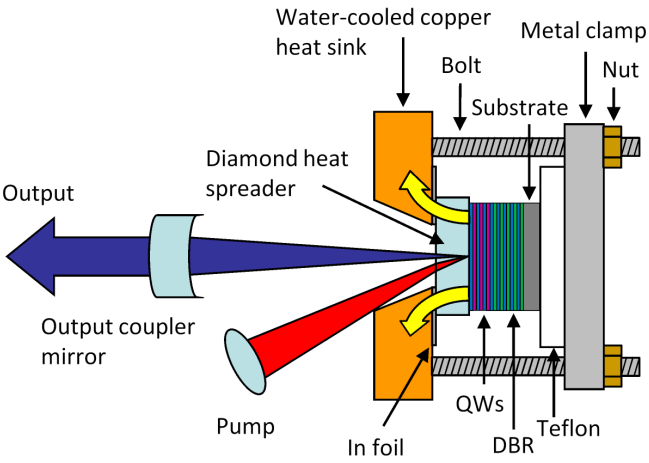

Figure 2.11: A semiconductor disk laser utilizing the intra-cavity diamond heat spreader method. The yellow arrows express the route and direction of heat flow.

Diamonds are optically transparent from ultraviolet to far-IR, superior to transparency bands of any other solid [84]. In addition, diamonds have no absorption peaks in the region of 0.5–2.5 µm [85], which makes them ideal heat spreader windows for SDLs in the most studied region. The use of intra-cavity diamonds has enabled SDLs with output powers more than 10 W [86–88].

Intra-cavity diamonds do, however, cause some issues with the laser performance. Although diamonds are considered to be isotropic, in some circumstances birefringence can exist in considerable amounts [89]. Depending on the amount of birefringence and the diamond dimensions, the heat spreader can act as a wave plate. As to be shown in subchapter 3.2, linear polarization is usually inherent for SDLs. Therefore, this phase retardation can cause considerable effects on the laser behaviour. Especially, if polarization selective elements, such as a Brewster plates, are used as intra-cavity elements, consequent Brewster losses can be substantial. Van Loon et al. [90] studied the effect, and the samples they analyzed showed that in natural diamonds the birefringence was either negligible or low with uniform orientation. For single-crystal synthetic diamonds this wasn't the case, as non-uniform orientations in the birefringence did exist. They measured the effect by placing a Brewster plate into the external cavity, and rotated the polarization direction with a half-wave plate. The result was that even a few degree misalignment between the laser's polarization and the orientation of the diamond birefringence causes percent level

losses in a single round trip.

Another, at the same time useful and annoying feature of heat spreader diamonds is that if planar, they act as FP etalons, which cause undesired fringes into the emission spectrum due to the FP filtering effect. At normal incidence, the free spectral range (FSR) i.e. the difference between the peaks is defined as [91]

$$\Delta\lambda \approx \frac{\lambda_0^2}{2nd}, \tag{2.34}$$

where λ_0 is the center wavelength, n is the refractive index of the etalon and d is the etalon thickness. An example of etalon fringes in an optical spectrum of a laser is presented in Figure 2.12.

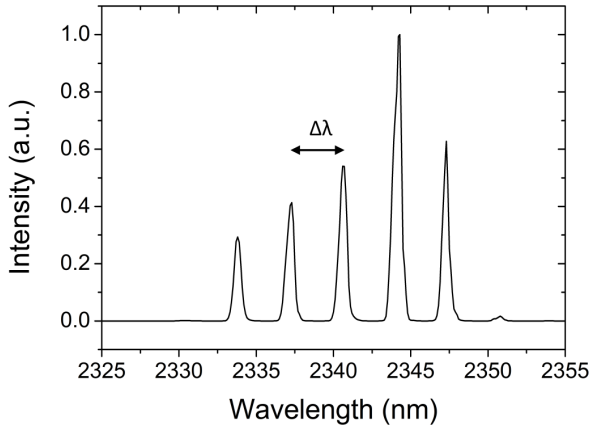

Figure 2.12: Etalon fringes in laser spectrum caused by the intra-cavity diamond. The free spectral range is 3.5 nm.

The FSR and the full bandwidth at half of the maximum intensity (FWHM) of the etalon transmission band are linked by a relation called finesse, and it is defined as [91]

$$\mathscr{F} = \frac{\Delta\lambda}{\Delta\lambda_c}, \tag{2.35}$$

where $\Delta\lambda_c$ is the transmission band's FHWM.

The phenomenon can be decreased by attenuating the surface reflections in the diamond by fabricating an antireflective coating (AR) on the diamond or using a wedged diamond. On the other hand, if the FSR is large, the filtering effect can be used to induce single-mode operation [92], or to tune the laser wavelength of a broadband laser by selecting a narrow peak with a Brewster plate [93]. Similar tuning can also be achieved with a simple air gap as an etalon in a short I-cavity, where the output coupler is a relatively thick plano-convex mirror [94]. In such a cavity, the outer, convex surface of the mirror provides the feedback, and the air

gap etalon is between the gain mirror and the mirror rear surface. The FSR of the etalon is directly chosen by altering the air gap.

2.5.2 Flip-chip method

In another thermal management approach that utilizes no intra-cavity heat spreaders, the gain mirror elements are grown on the substrate in reversed order and the substrate is removed by etching. Since the gain chip is eventually flipped upside down, the method is called flip-chip bonding. The flip-chip sample is bonded onto a heat spreader, such as diamond, leaving the DBR as the bottom layer. Being substantially thinner than the substrate, the DBR acts as a better heat conductor. A two-mirror cavity with a flip-chip bonded gain mirror is presented in Figure 2.13.

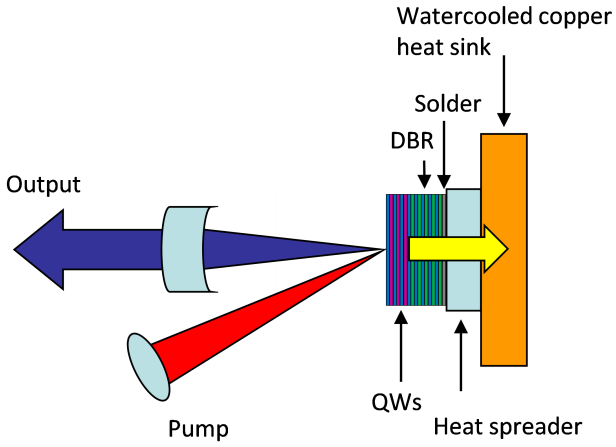

Figure 2.13: A semiconductor disk laser utilizing the flip-chip bonding approach. The yellow arrow expresses the route and direction of heat flow.

The bonding process requires much more exactitude compared to intra-cavity heat spreader bonding. Different type of solders can be used depending on the application, but e.g. aiming for high powers and high reliability enforces to use hard or semi-hard solders. When the solder elasticity is unsubstantial, the coefficients of thermal expansion for the heat spreader and the sample need to be almost equal to avoid damage. Although the bonding process is more demanding compared to that of intra-cavity diamonds, with this approach problems related to optical heat spreaders can be avoided, since no birefringent or etalon-forming elements are included. In addition, lower cost non-optical heat spreader diamonds can be used.

2.5.3 Thermal management in GaSb-disk lasers

As pointed out in equation 2.1, the physical thickness of a layer in a semiconductor DBR is directly proportional to the target wavelength of the stopband design.

Therefore, the longer the wavelength is, the thicker the DBR becomes. Concerning the thermal management in GaSb SDLs, the DBR design quickly leads to great thicknesses, and choosing the optimal heat extraction method between intra-cavity heat spreader and flip-chip approach becomes even more relevant.

Kemp et al. studied the thermal management in a 2.3 µm SDL [95]. The DBR structure was very similar to that of the 2.35 µm SDL used in this thesis. In their simulations, they used thermal conductivities of 20 $\frac{\mathrm{W}}{\mathrm{mK}}$ (radial) and 14 $\frac{\mathrm{W}}{\mathrm{mK}}$ (axial) for the DBR layer. The values for diamonds given in Table 2.2 are more than 100 times larger. As the heat spreader diamonds used in this work have a physical thickness of 300 µm, and the DBR being approximately 7 µm thick, it can be roughly estimated that for GaSb SDLs, the intra-cavity diamond approach provides a heat extraction two times more efficient than that of flip-chip bonding. This is also the implication Kemp et al. concluded.

It is a fact that both aforementioned SDL bonding methods described in subchapters 2.5.1 and 2.5.2 have their pros and cons. The etalon effect and heat spreader absorption are avoided with the use of flip-chips, but the bonding process with intra-cavity heat spreaders is substantially more simple. Nevertheless, when it comes to thermal issues, using diamonds as intra-cavity heat spreaders leads supposedly to better results with the GaSb material system, which emphasizes the significance of the heat transfer channel proximity to the center of heat generation.

3. POLARIZATION

3.1 Physical definition of polarization

Light can be treated as a transverse electromagnetic wave, whose electric field consists of the vector sum of two orthogonal components and is given as [91]

$$\begin{aligned} \boldsymbol{E}(z,t) &= \boldsymbol{E}_{\mathrm{x}}(z,t) + \boldsymbol{E}_{\mathrm{y}}(z,t) \\ &= \hat{\boldsymbol{x}} E_{0\mathrm{x}} \exp\left[j(kz - \omega t)\right] + \hat{\boldsymbol{y}} E_{0\mathrm{y}} \exp\left[j(kz - \omega t + \phi)\right], \end{aligned} \tag{3.1}$$

where $\hat{\boldsymbol{x}}$ and $\hat{\boldsymbol{y}}$ are the orthogonal unit vectors, $E_{0\mathrm{x}}$ and $E_{0\mathrm{y}}$ are the respective amplitudes of the orthogonal components, k is the wave number, ω is the angular frequency of the wave and ϕ is the phase difference between the components. The direction of this electric field is called polarization, and the state of this polarization is described by the two orthogonal components, as illustrated in Figure 3.1.

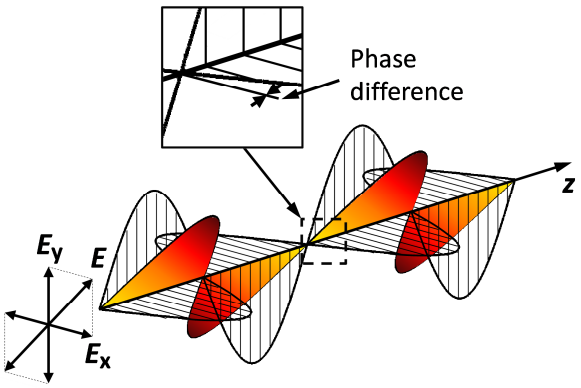

Figure 3.1: Polarization of light. The gradient filled curve represents the oscillating electric field, and the riddle curves are its horizontal and vertical components. The framed magnification shows the phase difference between the two propagating field components. In this case the phase difference is zero, and the field components oscillate symmetrically in their respective planes.

If the two components oscillate in phase, the polarization is said to be in $\mathscr{P}$-state or linearly polarized as presented in Figure 3.2(a). The relation of the orthogonal amplitudes determines the direction of polarization. For instance, if all the energy

of the electric field is focused to oscillate in the x-direction, light is said to be horizontally polarized. Analogically, y-polarized light is vertically polarized.

The case of phase difference being $\pi/2$ denotes that the constituent waves oscillate in opposite phases. If the amplitudes of the orthogonal components are equal, the resultant electric field vector rotates in time at the angular frequency ω and with a constant amplitude. When looking at the light in direction back to the source, a wave with a polarization rotating clockwise is said to be in $\mathscr{R}$-state or right-circularly polarized. $\mathscr{L}$-state or left-circular polarization refers to anti-clockwise rotation, which is illustrated in Figure 3.2(c).

Both linear and circular polarization are special cases of elliptical polarization ($\mathscr{E}$-state), in which the phase difference is $0 < \phi < \pi/2$. In this case, the electric field vector rotates, but also the amplitude changes. Mathematically, in one round of rotation the endpoint of the vector draws an ellipse as presented in Figure 3.2(b). The direction of polarization, angle θ is given by [91]

$$\theta = \frac{\arctan \frac{2E_{0x}E_{0y}\cos(\phi)}{{E_{0x}}^2 - {E_{0y}}^2}}{2}. \tag{3.2}$$

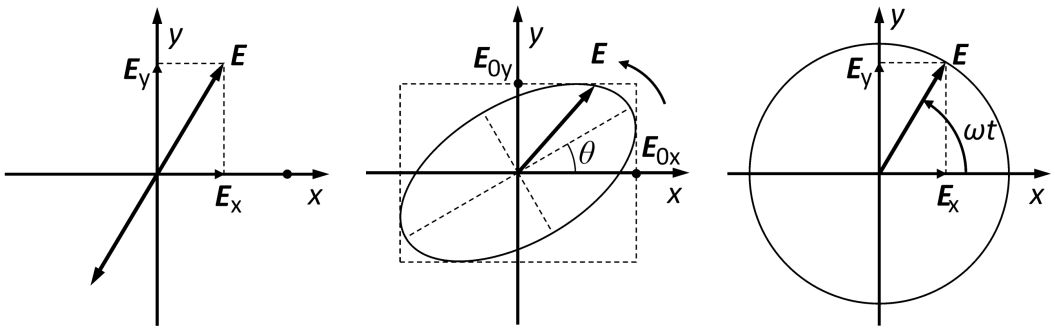

(a) Linear polarization. (b) Elliptical polarization. (c) Left-circular polarization.

Figure 3.2: Different polarization types.

3.2 Polarization of a semiconductor disk laser

It has been shown, that a few percent dichroism can exist between the [110] and [1$\bar{1}$0] crystal axis [54] in QWs of a semiconductor gain material. A dichroic material has selective absorption of the other orthogonal $\mathscr{P}$-state component, which causes linear polarization to stabilize along [110] axis. Therefore, this circular symmetry breakdown makes SDLs usually linearly polarized by nature [96].

3.3 Jones calculus

Jones calculus is similar to ray optics formalism dealt with in subchapter 2.4.1 and it can be used to describe the polarization of light. Jones vector is a 2×1 array that represents the polarization state itself. Jones vector holds the information about the amplitudes of the orthogonal electric field components and their phases. In complex form the Jones vector is [91]

$$\mathscr{J} = \begin{bmatrix} E_{0\mathrm{x}} e^{j\varphi_{\mathrm{x}}} \\ E_{0\mathrm{y}} e^{j\varphi_{\mathrm{y}}} \end{bmatrix}, \tag{3.3}$$

where $E_{0\mathrm{x}}$ and $E_{0\mathrm{y}}$ are the amplitudes of the instantaneous scalar components of the Jones vector, and φ_{x} and φ_{y} are the respective phases.

The Jones matrix or a transform matrix is used to represent an optical element

$$\mathscr{A} = \begin{bmatrix} a_{11} & a_{12} \\ a_{21} & a_{22} \end{bmatrix}, \tag{3.4}$$

and similarly to ABCD formalism, by multiplying the Jones vector of incident light with the Jones Matrix of the optical element, the state of polarization for the transmitted light after the optical element is given as

$$\mathscr{J}_{\mathrm{t}} = \mathscr{A}\,\mathscr{J}_{\mathrm{i}}. \tag{3.5}$$

3.3.1 Birefringent elements

Optically anisotropic materials have a repetitive arrangement in their atomic or molecular structure, and hence their optical properties vary depending on the direction of propagation. This directionality manifests itself in different refractive indices for different polarization components [91]. This section briefly reviews how the effects of such a birefringent element can be determined using Jones vectors and matrices.

Due to the orientated crystal structure, the effect of a birefringent material on an optical wave depends strongly on the polarization of the incident light. When polarized light interacts with a birefringent medium, it experiences a phase shift between the two orthogonal polarization components [97]

$$\delta = \frac{2\pi d \Delta n}{\lambda}, \tag{3.6}$$

where d is the medium thickness and $\Delta n = n_{\mathrm{e}} - n_{\mathrm{o}}$ is the birefringence i.e. difference between extraordinary and ordinary refractive indices. The phase shift changes the state of polarization and thus the outgrowth is different depending on the original polarization. For example, if the phase retardation is π radians, the electric field

components experience a half-wave phase shift with respect to each other, which corresponds to a flip of the other component presented in Figure 3.1. Therefore, the vector sum of the two components is changed and polarization direction is rotated according to Figure 3.3(a). Correspondingly, a quarter-wave plate presented in Figure 3.3(b) generates a phase retardation of $\pi/2$ and transforms linear polarization into circular polarization and vice versa.

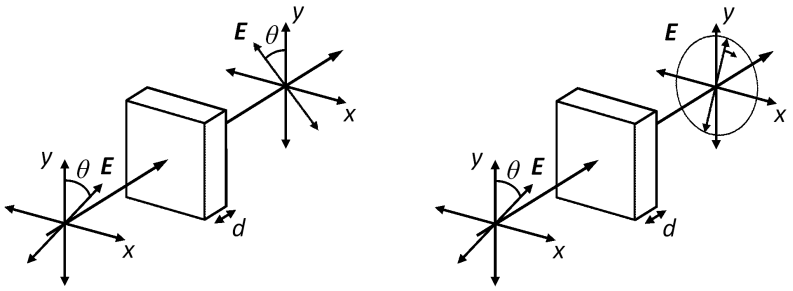

(a) A half-wave plate rotates the direction of polarization.

(b) A quarter-wave plate transforms linearly polarized light into left-circularly polarized light.

Figure 3.3: Two types of wave plates. Direction y corresponds to optical axis of the wave-plate.

For a birefringent wave plate the Jones matrix is [90]

$$\mathscr{M} = \begin{bmatrix} e^{\frac{j\delta}{2}} & 0 \\ 0 & e^{\frac{-j\delta}{2}} \end{bmatrix}. \tag{3.7}$$

As shown above, the polarization direction of light after passing a birefringent element is dependent on the polarization direction of incident light. If the light's fundamental direction of polarization differs from the orientation of the birefringence, the Jones matrix needs to be multiplied by a rotation matrix [90]

$$R(\theta) = \begin{bmatrix} \cos(\theta) & -\sin(\theta) \\ \sin(\theta) & \cos(\theta) \end{bmatrix}, \tag{3.8}$$

where θ is the misorientation between the birefringence axis and the direction of polarization of the incident beam. If the case of a wave plate in a laser cavity is considered and losses are ignored, the Jones matrix corresponding to a round trip in the cavity (the wave traverses the wave plate twice) becomes

$$\mathscr{M}_{\mathrm{RT}} = R(-\theta) \cdot M(\theta) \cdot R(\theta) \cdot R(-\theta) \cdot M(\theta) \cdot R(\theta). \tag{3.9}$$

With this relatively simple formalism effects of e.g. birefringence in diamond heat spreaders (to be discussed in chapter 2.5.1) to the laser performance can be estimated.

3.4 Highly reflective gratings

Dielectric gratings are an interesting element in the photonics field due to their spectrally selective properties, small size and the wide availability of materials having good transparency for certain wavelengths. Dielectric gratings based on guided-mode resonance (GMR) can be used to replace thick distributed Bragg reflector mirrors in vertical cavity light-emitting diodes [98] or even focus a laser beam by tuning the line width and period of the grating [99]. HR gratings have also been used in semiconductor disk lasers for stabilizing the emission and polarization [100]. They are also suitable for introducing an external feedback element/pump coupler for fiber lasers, as the grating structure can be designed to be transparent for pump wavelength but to reflect the laser emission [101].

However, GMR mirror development in the IR range has been challenging, since a high refractive index contrast is a necessity in obtaining high reflectivity, and finding suitable materials has been arduous. Lately, the feasibility of germanium (Ge) for fabricating broadband grating mirrors in the IR range has been studied by Kontio et al. [102]. Ge fulfils several requirements to achieve high reflectivity in the IR range. First of all, the material costs are low and the processing is straightforward. At room temperature, Ge has a very high index of refraction of >4.0 at wavelengths 2–12 µm [103]. Ge also has a very low absorption above the band gap energy 0.66 eV corresponding to a wavelength of 1.88 µm, and the transmission spectrum of Ge extends from 1.9 to over 17 µm. In this work, a Ge grating fabricated by Kontio et al. was tested as an output coupler in an SDL to determine the suitability of Ge gratings as laser output coupler.

3.4.1 Polarization selection

The aim in this work was to use a Ge grating for polarization stabilization of a 2.35 µm SDL. This subchapter focuses on the theoretical ground of polarization selective gratings. The following review is according to reference [104]. Let us consider a wave propagating in a waveguide grating presented in Figure 3.4. The

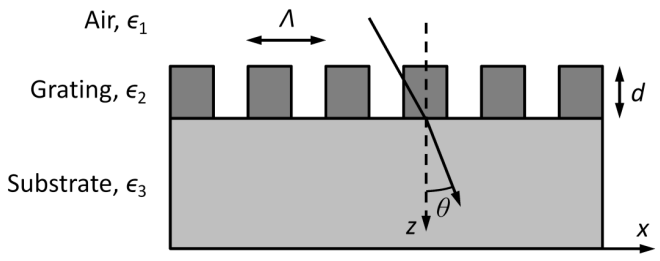

Figure 3.4: A schematic illustration of a planar waveguide grating.

spatially modulated relative permittivity of the grating is

$$\epsilon_2(x) = \epsilon_\mathrm{g} + \Delta\epsilon \cos(Kx), \tag{3.10}$$

where ϵ_g is the average relative permittivity of the grating, $\Delta\epsilon$ is the modulation amplitude and

$$K = \frac{2\pi}{\Lambda}, \tag{3.11}$$

where Λ is the grating period. According to rigorous coupled-wave theory, the coupled-wave equations for transverse electric (TE) polarization can be expressed as [105]

$$\begin{aligned}\frac{\mathrm{d}^2\hat{S}_i(z)}{\mathrm{d}z^2} + &\left[k^2\epsilon_\mathrm{g} - k^2\left(\sqrt{\epsilon_\mathrm{g}}\sin\theta - \frac{i\lambda}{\Lambda}\right)^2\right]\hat{S}_i(z) \\ &+ \frac{1}{2}k^2\Delta\epsilon\left[\hat{S_{i+1}}(z) + \hat{S_{i-1}}(z)\right] = 0,\end{aligned} \tag{3.12}$$

where $\hat{S}_i$ is the amplitude of the inhomogeneous plane wave of the ith space harmonic, k is the wave number $2\pi/\lambda$, λ is the wavelength in vacuum, and θ is the internal angle of incidence i.e. angle between diffracted wave and the grating normal. In the case $\Delta\epsilon \to 0$, equation 3.12 reduces to

$$\frac{\mathrm{d}^2E(z)}{\mathrm{d}z^2} + \left(k^2\epsilon_\mathrm{g} - \beta^2\right)E(z) = 0, \tag{3.13}$$

where the propagation constant is defined by

$$\beta = Nk, \tag{3.14}$$

where N is the effective waveguide index of refraction. Equation 3.13 corresponds to wave equation in the case of an unmodulated dielectric waveguide. If the inequality

$$\max\left\{\sqrt{\epsilon_1}, \sqrt{\epsilon_3}\right\} \leq |N| < \sqrt{\epsilon_\mathrm{g}} \tag{3.15}$$

holds, a guided wave can be excited. As $\Delta\epsilon \to 0$ and correspondingly $\beta \to \beta_i$, the effective propagation constant becomes

$$\beta_i = k\left(\sqrt{\epsilon_\mathrm{g}}\sin\theta - \frac{i\lambda}{\Lambda}\right), \tag{3.16}$$

where the effective refractive index equals $N_i = \beta_i/k$.

For a TE polarized wave in an unmodulated waveguide the eigenvalue function is [106]

$$\arctan(\gamma/\kappa) + \arctan(\delta/\kappa) = \kappa d - N\pi, \tag{3.17}$$

where the abbreviations are defined as

$$\kappa = \left(\epsilon_{\mathrm{g}} k^2 - \beta_i^2\right)^{1/2}, \tag{3.18}$$

$$\gamma = \left(\beta_i^2 - \epsilon_1 k^2\right)^{1/2} \tag{3.19}$$

and

$$\delta = \left(\beta_i^2 - \epsilon_3 k^2\right)^{1/2}. \tag{3.20}$$

Equation 3.17 can be reformed to give an eigenvalue equation for a TE polarized wave in a modulated waveguide [104]

$$\tan(\kappa_i d) = \frac{\kappa_i(\gamma_i + \delta_i)}{\kappa_i^2 - \gamma_i \delta_i}, \tag{3.21}$$

and for transverse magnetic (TM) polarized wave

$$\tan(\kappa_i d) = \frac{\epsilon_{\mathrm{g}} \kappa_i(\epsilon_3 \gamma_i + \epsilon_1 \delta_i)}{\epsilon_1 \epsilon_3 \kappa_i^2 - \epsilon_{\mathrm{g}}^2 \gamma_i \delta_i}. \tag{3.22}$$

Due to the difference of eigenvalue functions for TE and TM modes, the corresponding resonances for TE- and TM polarized incident waves have different parametric locations. Consequently, this kind of a waveguide grating acts as a polarization selective element [104]. When used as a cavity mirror, as in this thesis, a polarized output of the laser can be achieved if the laser line width is narrow compared to the separation between the center wavelengths of the TE- and TM mode resonances, that can be calculated with equations 3.21 and 3.22, respectively [105]. It is also assumed that the discrimination between TM an TE modes is large compared to the losses tolerated by the laser.

3.4.2 The principle to achieve high reflectivity in a grating

Here the high reflectivity of the Ge mirror is based on GMR. This phenomenon occurs when a incident light is diffracted and "trapped" inside a waveguide. In a periodic waveguide structure, e.g. a grating, where the periodic layer has a higher index of refraction than the adjacent layer [107] such as air as in this work, the modes experience modulation and thus cannot be sustained in the waveguide and become leaky [108]. As the incident wave couples into a leaky mode, a quite complete energy change between zeroth order forward- and backward-diffracted waves happen and the wave is reradiated backwards [104, 109]. GMR-based optical devices are applicable for example as filters, reflectors and laser mirrors as such [110]. Moreover, they

can be used to enhance Bragg reflectors and other thin film optical elements to leaky-mode resonance [111].

4. PULSED LASERS

4.1 Introduction

The output power of continuous wave lasers is limited mainly due to thermal issues. Pulsed lasers enable high peak output powers, since the energy is released in a short time. On the other hand, with a lower pulse repetition rate more energy can be stored in the system and then released in consecutive pulses. Since the laser emission can be collimated and focused to a small area, intensities can be extremely high, which is a well-requested feature in specialized material welding, micro-machining, marking and surgery. Pulsed operation in lasers can be achieved in numerous ways, which are suitable for different applications. This chapter introduces one to the most common methods for generating laser pulses, focusing on passive mode-locking, the technique used in this work.

4.2 Mode-locking

Mode-locking is the main method for creating ultra-short pulses in lasers. The principle is to force the longitudinal modes to maintain fixed phase relations, which results in varying output as a function of time. This is achieved by modulating the losses inside the laser cavity in such a way that only a few or a single pulse is amplified enough to remain circulating the cavity. An output pulse is produced on each incidence in the output coupler mirror, and thus a periodic train of pulses achieved in the output. It depends on the oscillating modes and the maintained phase relation, what form is the output like [112]. Only a weak modulation synchronous with the circulating wave round trip time is needed to initiate a pulse. This pulse can be made shorter at each round trip. Since widening of the spectrum and the pulse shortening evolve hand in hand, eventually the gain spectrum of the active medium defines minimum duration of the pulse [113]. Therefore, the operation of a mode-locked laser can usually be well estimated by observing the spectrum. This will be shown in the following.

4.2.1 Basics for mode-locking

In chapter 2.4.3 the case of uncorrelated phases between the cavity modes was viewed in terms of a simple model with $2n$ longitudinal modes oscillating in the cavity. If

the phase correlation is assumed to exist, and the phase of the mode l is written as

$$\varphi_l = l\varphi, \tag{4.1}$$

the total electric field in the cavity becomes [67]

$$E(t) = \sum_{l=-n}^{n} = E_0 \exp\left[j\left(\omega_0 + l\Delta\omega\right)t\right] \exp\left(jl\varphi\right) = A(t)\exp\left(jl\omega_0 t\right). \tag{4.2}$$

Adopting a new variable $\Delta\omega t' = \Delta\omega + \varphi$ yields

$$A(t') = E_0 \sum_{l=-n}^{n} \exp\left(jl\Delta\omega t'\right). \tag{4.3}$$

The amplitude of the electric field in equation 4.2 can be obtained from the Fourier transform of the electric field in frequency domain [114]

$$A(t) = \frac{1}{2\pi}\int_{\infty}^{-\infty} E(\omega)\exp\left(-j\omega t\right)\mathrm{d}\omega, \tag{4.4}$$

and from the Fourier inversion theorem follows

$$E(\omega) = \int_{\infty}^{-\infty} A(t)\exp\left(j\omega t\right)\mathrm{d}t. \tag{4.5}$$

As equations 4.4 and 4.5 indicate, there is an explicit connection between the laser spectrum and pulse duration. By considering equation 4.3 as an integral, the pulse duration as a function of the spectral width could be calculated according to the Wiener-Khinchin theorem [97, 115], but the same result can be attained by noticing that equation 4.3 has the form of geometrical series. It can be rewritten as

$$A(t') = E_0 \frac{\sin\left[\frac{(2n+1)\Delta\omega t'}{2}\right]}{\sin\left(\frac{\Delta\omega t'}{2}\right)}. \tag{4.6}$$

The total intensity of the electric field is therefore

$$I \sim < |E(t')|^2 > = < A^2(t') > = {E_0}^2 \frac{\sin^2\left[\frac{(2n+1)\Delta\omega t'}{2}\right]}{\sin^2\left(\frac{\Delta\omega t'}{2}\right)}, \tag{4.7}$$

which is found out to be periodic pulse train as seen in Figure 4.1, where the intensity profile of the electric field is plotted versus time with the value $n = 5$.

Any sine function $\sin(\theta)$ goes to zero at $\theta = m\pi, \forall m \in \mathbb{Z}$. Since the denominator in equation 4.7 goes to zero at values $\Delta\omega t' = m\pi$, the separation between two successive intensity maxima is

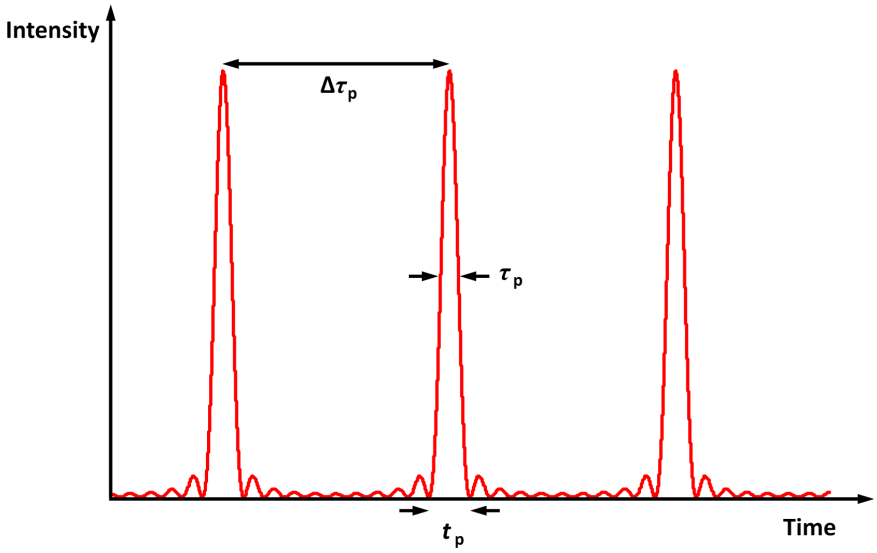

Figure 4.1: Total field intensity in time domain of a mode-locked laser with 11 modes.

$$\tau_{\mathrm{p}} = \frac{2\pi}{\Delta\omega} = \frac{1}{\Delta\nu}. \tag{4.8}$$

The pulse duration can also be derived on the grounds of the sine function minima. The numerator in equation 4.7 goes to zero at $(2n+1)\Delta\omega t'/2 = m\pi$. Therefore, the full width of the pulse is given by

$$t_{\mathrm{p}} = 2\frac{2\pi}{(2n+1)\Delta\omega} = 2\frac{2\pi}{\Delta\omega_L} = \frac{2}{\Delta\nu_L}, \tag{4.9}$$

where $\Delta\nu_L$ is the laser's FWHM. Equation 4.9 shows that the pulse duration is inversely proportional to the laser bandwidth. Although this derivation doesn't give a realistic result due to the assumption of a uniform amplitude distribution, it does imply the connection between the spectral bandwidth of the laser and the pulse width. Assuming an e.g. Gaussian distribution of the longitudinal modes gives more realistic values. In this case, the amplitude of a longitudinal mode is [4]

$$E_l = E_0 \exp\left[-\frac{1}{2}\left(\frac{2l\Delta\omega}{\Delta\omega_L}\right)^2 \ln 2\right]. \tag{4.10}$$

Similarly to the model of uniform distribution in equation 4.3, the amplitude of the total Gaussian field becomes

$$A(t') = \sum_{l=-\infty}^{l=\infty} E_l \exp\left(jl\Delta\omega t'\right). \tag{4.11}$$

The sum can be approximated by an integral, when the total intensity is written

as [4]

$$I \sim A(t)^2 \propto \exp\left[-\left(\frac{2t}{\Delta\tau_{\mathrm{p,G}}}\right)^2 \ln 2\right], \tag{4.12}$$

where the Gaussian pulse width (FWHM) is defined as

$$\Delta\tau_{\mathrm{p,G}} = 2\frac{2\pi \ln 2}{\pi\Delta\omega_{\mathrm{L}}} = \frac{2\ln 2}{\pi\Delta\nu_{\mathrm{L}}} = \frac{0.441}{\Delta\nu_{\mathrm{L}}}. \tag{4.13}$$

Equation 4.13 gives the shortest possible pulse duration from a laser with a Gaussian spectrum of FWHM $\Delta\nu_{\mathrm{L}}$. The quotient $2\ln 2/\pi$ is called the numerical factor and it depends on the shape of the spectral intensity distribution. Therefore, the minimum pulse length for any spectral profile is given by

$$\Delta\tau_p = \frac{\kappa}{\Delta\nu_{\mathrm{L}}}, \tag{4.14}$$

where κ is the numerical factor.

Pulses equal to duration given by equation 4.14 are said to be bandwidth limited or transform limited, following from the relation of the pulse's time and frequency Fourier transforms.

4.2.2 Passive mode-locking with a semiconductor saturable absorber mirror

In passive mode-locking the amplitude of the electromagnetic wave in the laser cavity modulates due to real or artificial saturating absorption. This nonlinear process is dependent on the incident beam intensity i.e. the resonance field in the cavity. The absorption of the optical element varies according to the light intensity, which modifies the losses inside the cavity in such a way, that high intensity results in reduced losses.

Passive mode-locking has four main types [4]:

1) Fast saturable absorber mode-locking is based on an absorbing material, which has a very short excited state lifetime and suitable saturation properties.

2) A Kerr lens is a self-focusing, nonlinear optical element.

3) In slow saturable absorber mode-locking, the dynamic saturation of the gain medium is exploited.

4) Additive pulse mode-locking. A self-phase-modulating nonlinear optical element is placed in an auxiliary cavity and coupled to the main cavity of the same length.

In addition, there are several ways to passively mode-lock fiber lasers that exploit e.g. nonlinear polarization rotation [116, 117] or a nonlinear loop mirror [118], also called Sagnac loop [119].

SESAM structure

In this work, passive mode-locking with a fast semiconductor saturable absorber mirror (SESAM) was used. The first SESAM was introduced by Keller et al. in 1992 [120]. The structure of a SESAM is similar to the gain mirror described in chapter 2.3; a single or multiple thin semiconductor quantum well layers are grown on top of a DBR with high reflectivity. Such architecture is very dexterous, since to achieve mode-locking, one of the cavity mirrors only needs to be replaced with a SESAM. Instead of QWs, also QDs [121] or bulk absorbers [122] can be used.

There are various types of SESAMs. In an antiresonant structure [120] the cavity resonance wavelength is different from the operation wavelength and the optical field maxima are mismatched from the QW locations. The benefits of the antiresonant design are decreased losses in the cavity and minimal group velocity dispersion (to be discussed in subchapter 4.5.2). In addition, the field intensity inside the FP cavity is significantly lower compared to that of incident light. Therefore, the effective saturation intensity (will be discussed in subchapter 4.2.2) is increased and the risk of SESAM damage diminishes [120]. Antiresonant SESAMs are widely used for solid state laser mode-locking. In the design by Keller et al. a highly reflective mirror, a semiconductor DBR, was placed on the bottom and a dielectric DBR on top to form a FP cavity. With this kind of a structure, the intensity entering the SESAM can be controlled, which in turn determines the effective saturation intensity. On the downside, this kind of a structure has a high finesse, which corresponds to a narrow passband of the etalon transmission peaks, as indicated in equation 2.35. To broaden the passband, the finesse of the cavity for the SESAM can be decreased by depositing an AR coating on top of the semiconductor surface of the SESAM [123]. Also the Fresnel reflection emerging in the semiconductor-air interface can be exploited, as in the SESAM used in this work.

The SESAM can also have a resonant structure [124], which is similar to the gain area of an SDL, in which the optical field maxima are located at the QW positions. Also a single quantum well (SQW) structure can be made resonant [125]. The resonant structures cannot usually be used to mode-lock solid-state lasers, since the induced losses are too high. Moreover, they influence the average dispersion of the laser cavity due to the high group delay dispersion [126]. However, the resonant absorber mirrors are useful in fiber lasers with high gain amplifiers. In addition, the amount of radiation entering the SESAM can be controlled with the top mirror, which in turn affects the nonlinear reflectivity, saturation intensity and the damage threshold of the absorber [127].

The operation of a SESAM

The operation principle of a SESAM is that low optical intensities normally excite electrons to conduction band and by electron-hole recombination these states decay. High optical intensities, however, cause electrons to accumulate in the conduction band. As a result, the original low-energy states initiated by the absorption of photons deplete, while the final high-energy states remain occupied. Therefore, the absorption of the quantum wells saturate. [114]

The saturable absorption allows for self-stabilized mode-locking. Noise spikes always exist in CW radiation. Due to the higher intensity, these spikes experience lower absorption when interacting with the SESAM and the feedback is stronger than for CW background radiation. Thus the spikes gain more energy at each round trip and eventually bring about the saturation of the gain. As the spikes reserve more and more of the energy available from the gain, CW background signal starts to fall. Finally, the most energetic spike overcomes every other, and only a single pulse is circulating the cavity. In addition, the saturable absorber has a feature that favors the peak over the wings of the pulse [114]. This enforces the pulse to shorten at each round trip until the duration stabilizes to a certain limit due to broadening mechanism and eventually the transform limit.

Key parameters of a SESAM

The saturation intensity of a SESAM defines the point at which the absorption begins to saturate, and it is given as [128]

$$I_{\text{sat}} = \frac{h\nu}{\sigma_{\text{A}}\tau_{\text{A}}}, \tag{4.15}$$

where $h\nu$, σ_{A} and τ_{A} are the photon energy, the absorption cross section characteristic for the absorbing material and the absorber recovery time, respectively. Saturation fluence is the corresponding energy where the absorption saturation initiates. Since intensity is defined as power per unit area, the saturation fluence is obtained by multiplying the saturation intensity with the recovery time of the absorber

$$F_{\text{sat}} = \frac{h\nu}{\sigma_{\text{A}}}. \tag{4.16}$$

A typical reflectivity profile of a SESAM as a function of pulse fluence is presented in Figure 4.2.

The absorption loss coefficient for a fast absorber is defined as [4]

$$\alpha(I) = \frac{\alpha_0}{1 + \frac{I}{I_{\text{sat}}}}, \tag{4.17}$$

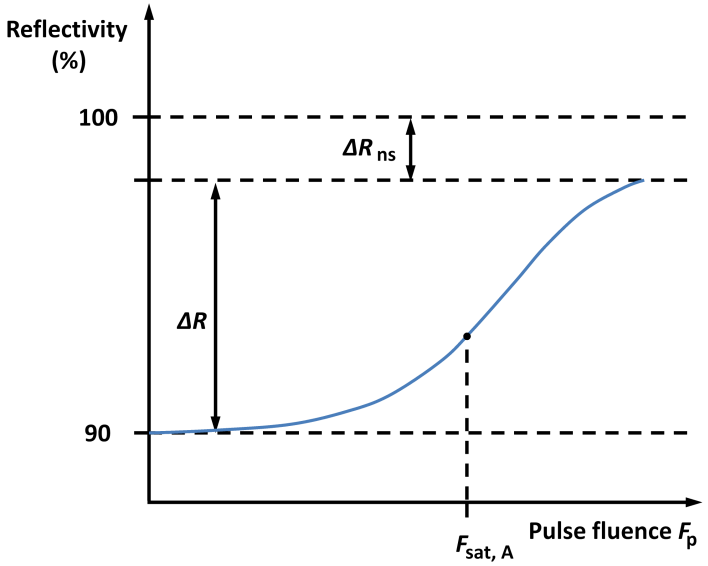

Figure 4.2: SESAM reflectivity as a function of pulse fluence. At low intensities absorption is strong and reflectivity remains low. As the the absorption begins to saturate after reaching saturation fluence F_{sat}, reflectivity starts to increase up to the maximum value determined by the non-saturable losses ΔR_{ns}. ΔR is called modulation depth.

from which it can be seen that the absorption decreases until the intensity of the incident radiation reaches the saturation intensity.

For slow SESAMs, the model is not as straightforward. The approach is done across a time-dependent power-loss coefficient $q(t)$, which depends on both the absorber parameters and the exciting pulse. The model uses a differential equation to describe the evolution of the power loss [129]

$$\frac{\mathrm{d}q}{\mathrm{d}t} = -\frac{q - q_0}{\tau_{\mathrm{A}}} - q\frac{I}{F_{\mathrm{sat}}}, \tag{4.18}$$

where q_0 is the unsaturated power loss. If the SESAM is very slow and the recovery time of the absorber is long enough, the first term on the right hand side in equation 4.18 can be neglected and the integration results in

$$q = q_0 \exp\left(-\frac{F_{\mathrm{p}}}{F_{\mathrm{sat}}}\right), \tag{4.19}$$

where F_{p} is the pulse fluence.

The lifetime of the photoexcited carriers in the conduction band (or the recovery time of the absorber) is one of the essential properties of a SESAM, since it defines the absorber speed and thus the pulse shaping mechanism of the absorber. For example, carrier lifetimes in the nanosecond scale are too slow for efficient pulse shaping, which is usual in pure high quality semiconductor crystals. By implanting or irradiating the sample with ions, one can create defects acting as fast non-radiative

points into the crystal. By reducing the charge carrier recombination time in the QWs with ion-irradiation, the recovery time can be made shorter. In addition to ion irradiation after growing process [130], low temperature growth [131], metamorphic growth [132] and proton bombardment [133] can be used the reduce the absorption recovery time and enable ultra-short pulses. The saturated absorption recovers back to initial level after the pulse, and the rate of this recovery defines the dominant mode-locking mechanism.

The saturable absorption is dependent on different kind of processes in the semiconductor material. The recovery time related to intraband carrier-carrier interactions and thermalization processes is in the femtosecond range. This fast component is an essential factor in stabilizing femtosecond pulses in a mode-locked laser. Absorption recovery time due to interband carrier recombination and trapping is in the order of picoseconds to nanoseconds. These slower processes complete the absorption recovery. The slow component of the absorption recovery time contributes to the starting of pulse formation and has an important role in lasers with pulse durations of picoseconds and longer [128]. A slow absorber has a recovery time longer than the pulse duration and the pulse shaping favors the attenuation of the pulse leading edge. As a result, the pulse center shifts backwards at each round trip. On the other hand, this simultaneously causes noise to suppress, which enables stable mode-locking in soliton mode-locked lasers even with slow absorbers [129]. A pump-probe system can be used to measure the SESAM's recovery time. The principle is to illuminate the absorber with a pump pulse and simultaneously measure the reflection or transmission of the sample as a function of time delay. Figure 4.3 shows an illustration of the absorbption recovery.

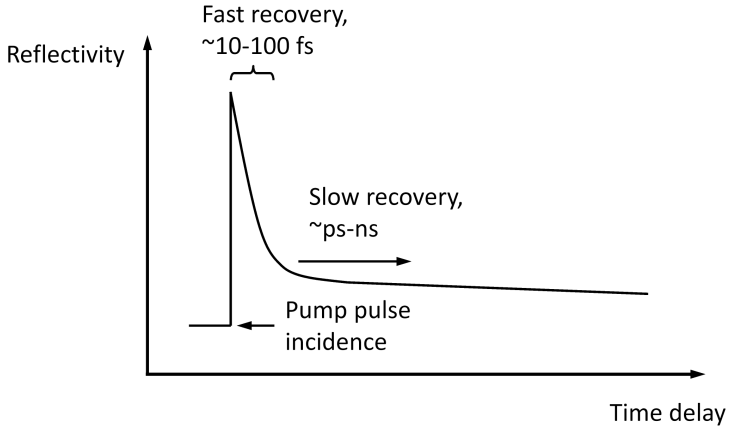

Figure 4.3: Reflectivity change of a SESAM hit by a pump-probe pulse. The absorption recovery time components with different durations are clearly distinguishable. [128, 134]

When the SESAM reflectivity is considered with respect to the intensity of the incident wave, two main attributes are used for description. Non-saturable losses

refer to the minimum losses that are residually present even when the absorption is saturated. Modulation depth is the increase in reflectivity from the unpumped state to the saturation level. The SESAM reflectivity depends on several parameters and it is defined as [135]

$$R = 1 - \Delta R_{\mathrm{ns}} - \Delta R \frac{\exp\left(\frac{-F_{\mathrm{p}}}{F_{\mathrm{sat}}}\right)}{\frac{-F_{\mathrm{p}}}{F_{\mathrm{sat}}}}, \tag{4.20}$$

where ΔR_{ns} is the non-saturable reflectivity loss and ΔR is the modulation depth.

When fabricating fast SESAMs, such as the one used in this work, certain issues need to be considered in the design. The amount of QWs has a major role, since several QWs increase the absorption. Therefore, the modulation depth is increased, which in practice results in larger non-saturated losses. In addition, due to the reduced material quality, also the saturation can slightly increase, which makes self-starting more complicated [136]. Especially for ultra-short pulses, a higher saturation level reduces the tendency for Q-switching instabilities due to thermal effects and two-photon absorption [137]. This means that if the average power of the laser experiences low-frequency oscillations and hence modulates the pulse train, the oscillations will take the form of high intensity, stable pulses with pulse widths in nanosecond range. In addition, the two-photon absorption reduces the SESAM reflectivity gradually at high intensities [138].

4.2.3 Active mode-locking

Active mode-locking needs to be forced by an external oscillating signal, which controls a modulator that alters either the gain/losses (amplitude modulation) or the round trip phase change (frequency modulation) in the cavity. The pulse circulates the cavity during the period of minimum losses, and higher losses in the pulse wings act as a pulse shortening mechanism [139]. The first actively mode-locked laser utilized amplitude modulation via an acousto-optic modulator, fused quartz block excited at longitudinal acoustic resonance, and it was reported in 1964 [140]. In this method, the refractive index of the modulator changes when it is stimulated with an acoustic standing wave. The periodic changes corresponding to cavity round trip time cause the laser light to refract differently and adequate feedback exists only for the remaining single nanosecond pulse.

Electro-optic modulators are optically active nonlinear crystals which can be used to induce phase shifts. When a voltage is applied over such a material, the refractive index of the material changes [141]. Electro-optic modulators are suitable for achieving mode-locked operation since the refractive index can be altered periodically. If sinusoidal voltage with a frequency matched to cavity round trip time is applied over the modulator, the laser radiation experiences frequency chirping due

to a phase shift of the same sinusoidal function of the voltage. As a consequence, the laser frequency is moved away from the center frequency and perhaps even outside the gain bandwidth. Therefore, only the light passing the modulator during the zero phase shift period is left circulating the cavity [142].

Femtosecond pulses are hard to achieve with active mode-locking due to the limitations in the pulse compression capability of the modulators. After all, pulses cannot become shorter than the low loss period, and periodically shorter signals would make it difficult to match the cavity dimensions to the modulating frequency [143]. However, with synchronous pumping femtosecond pulses from actively mode-locked lasers have been attained [144, 145]. In this method the laser cavity length is matched to that of the pulsed pump laser, so that the pump pulses and the pulses circulating in the laser cavity are synchronized.

4.3 Q-switching

Q-switching is a method for energetic, nanosecond, even picosecond scale pulse generation. Ultra-short pulses cannot be obtained with this approach, and it is mainly used to achieve high peak powers. The first Q-switched laser was reported as early as 1962 by McClung et al. [146]. The ruby laser they used, produced pulses with 600 kW peak power and 0.12 µs in duration.

In a Q-switched laser, the quality factor of the cavity is altered, which means that losses inside the cavity change. In active Q-switching, this is done by e.g. placing a loss-introducing modulator inside the resonator [66]. McClung et al. used a Kerr cell to rotate the polarization of the feedback light perpendicular to the fundamental polarization. During the period of low Q-factor, whilst there is no feedback into the gain medium, no lasing is achieved and the pump energy is stored into the gain medium. At some point maximum level of stored energy is achieved, and when the Q-factor turns high again, the stored energy is released as an energetic pulse of light.

Passive Q-switching uses saturable absorbers similarly to passive mode-locking. The use of a Kerr element can also be counted to be a passive method, but since it required external control of the voltage at least in the setup of McClung et al., it was considered here as an active method.

4.4 Gain switching

The concepts described in the previous subsections are more or less based on changes in cavity losses. The remaining option certainly is to modulate the gain, which is called gain switching. It is done directly by altering the pump power. The idea is that the pump pulse produces population inversion (significantly higher than threshold) much faster than the cavity photons reproduce to inversion-depleting

level. As the rapidly increased population inversion starts to decay by spontaneous emission, it takes several round trips before the actual lasing initiates. As the pump pulse ends, the energy stored in the gain medium is released as a pulse. Due to this energy build-up scheme, the obtained pulse can be much shorter than the pumping period. [4]

Gain switching is more feasible for laser diodes, since modulating the electric current is easier than to use a pulsed optical pump. Usually pulses in the nanosecond range can be obtained by gain switching, but also picosecond pulses from a diode laser have been reported [147].

Using a pulsed optical pump in an SDL reduces thermal effects in the gain mirror, which enables multiplied peak power level compared to CW operation. The pulse duration is ultimately limited by the pump pulse, but nanosecond pulses are achievable [148].

4.5 Autocorrelation

Pulsed lasers can reach pulse durations of only a few femtoseconds. However, typical photodetectors and oscilloscopes are not fast enough to measure pulses this short, since their response times are too long to record temporal pulse shapes. To overcome these bandwidth limitations indirect measurement techniques have been developed, and the motivation for picosecond pulse measurement arose after the first mode-locked lasers in the 1960's. J. A. Armstrong introduced a technique able to measure widths of 400 ps pulses in 1967 [149]. Autocorrelators are widely used in ultra-short pulse measurement and also in optical nonlinear microscopy [150]. In this work an autocorrelator was a necessary device in the mode-locked laser characterization, since the obtained pulses were too short to be measurable with other methods.

Autocorrelation is based on the nonlinear interaction of two photons from a laser beam divided into two different arms using a beam splitter. However, the process can be exploited in different ways. A traditional method is to use a nonlinear crystal to generate the second order signal. There are devices based on intensity and interferometric autocorrelation, in which the beam is focused into the crystal. Nevertheless, they have major fundamental differences. The use of a nonlinear crystal is not compulsory though, since the nonlinear phenomenon can also occur as two-photon absorption in the photodetector itself. The used methods are presented more detailed in the following subsection.

4.5.1 Setup types

Intensity autocorrelation

Second-harmonic generation (SHG) of two non-co-axial beams in a second order (denoted as $\chi^{(2)}$) nonlinear crystal is the basis of intensity autocorrelation (IAC). The nonlinear process occurs when high optical intensities affect the properties of the material, which in turn changes the nature of light [141]. In SHG, the interaction of two incident photons in a nonlinear material results in creation of a photon that has a frequency two times that of the original photons. The process is illustrated in Figure 4.4. Figure 4.4(a) represents the original and the generated wave after the nonlinear medium, and Figure 4.4(b) introduces the widely used manner of representation of nonlinear phenomena known as photon diagram.

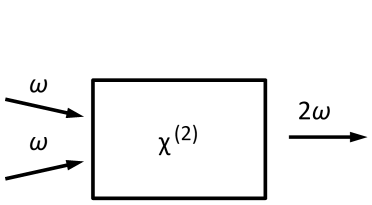

(a) A nonlinear medium affects two photons propagating non-co-axially.

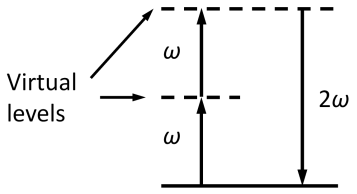

(b) Photon-diagram of the SHG.

Figure 4.4: Second frequency generation in a nonlinear medium.

An illustration of intensity autocorrelation is presented in Figure 4.5 Different lengths of the two arms cause a delay between the two beams. The output intensity from the SHG crystal thus depends on the temporal overlapping of the beams and is given as [151]

$$I_{\mathrm{SHG,IAC}}(\tau) = \int I(t)I(t+\tau)\,\mathrm{d}t, \tag{4.21}$$

where τ is the time delay between the waves.

The output from the crystal is recorded with a photodetector, usually a photomultiplier. When the other arm length is varied, the pulse envelope can be scanned as a function of the arm length difference, which can be translated into time delay. However, the autocorrelation signal does not give the real width of the pulse, since no phase information about the pulse is received. In addition, the generated trace is symmetric regardless of the pulse asymmetry. Therefore, assumptions about the pulse shape need to be made, after which a conversion or deconvolution factor can be used to calculate the estimated pulse width. The sech^2 and Gaussian shaped pulses are transferred to the autocorrelation trace; hence the use of deconvolution factors is justified.

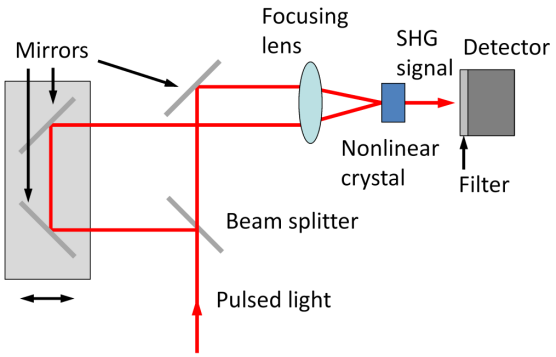

Figure 4.5: Intensity autocorrelation. The other arm length can be altered with the moveable stage. The filter transmits the 2ω radiation, but blocks the fundamental laser emission at ω.

Interferometric autocorrelation

An interferometric autocorrelator includes an interferometer where the beams combined from the two arms propagate co-axially to the nonlinear crystal or detector. The other arm length is variable as in intensity autocorrelation, but the beams from different arms are adjusted to propagate co-axially as presented in Figure 4.6. The beams are focused into a nonlinear crystal, where second harmonic generation takes place. As a result, the frequency of a photon is increased by a factor of two as presented in Figure 4.7.

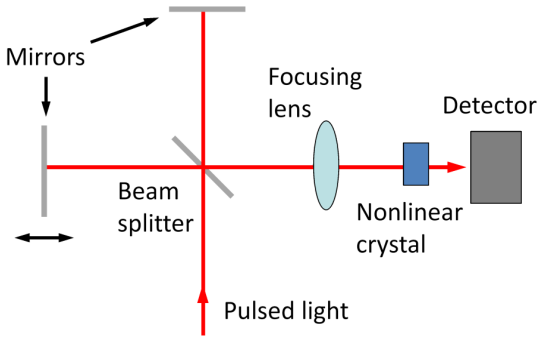

Figure 4.6: Interferometric autocorrelation. The different beams propagate into the nonlinear crystal co-axially.

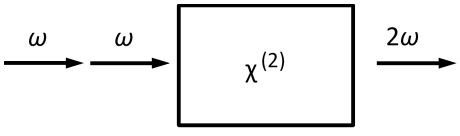

(a) A nonlinear medium affects the original, co-axially propagating photons.

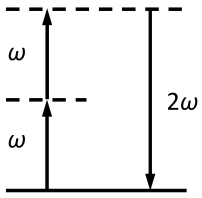

(b) Photon-diagram of the SHG.

Figure 4.7: Second harmonic generation in a nonlinear medium.

The intensity of the frequency doubled signal is dependent on the time delay [16]

$$I_{\mathrm{SHG,IFAC}}(\tau) = \int [E(t)E(t+\tau)]^4 \, \mathrm{d}t, \tag{4.22}$$

where IFAC denotes interferometric autocorrelation and τ is the time delay between the waves.

The two beams experience interference, which appears as fringes in the autocorrelation trace. The period of the fringes is naturally the inverse of the angular frequency 2ω:

$$t_{\mathrm{IFAC}} = \frac{1}{2\omega} = \frac{1}{4\pi\nu} = \frac{\lambda}{4\pi c}, \tag{4.23}$$

where ν and the λ are the frequency and the wavelength of the original pulse, respectively.

The maximum intensity is obtained when the phase mismatch equals zero. At this point the beams interfere constructively and the amplitude of the electric field is doubled, which corresponds to increase in intensity by a factor of four compared to a single pulse. According to equation 4.22, the intensity is thus 16 times that of a single pulse. However, due to the difference in arm lengths, no overlapping of the pulses occur in the crystal and the intensity is thus only two times the intensity that a single pulse generates. Therefore, the ratio between the peak autocorrelation signal and the background noise is eight.

Two-photon absorption autocorrelation

Two-photon absorption (TPA) is a nonlinear process, in which an atom absorbs two photons simultaneously and is excited to a higher energy state as shown in Figure 4.8(b).

As presented in Figure 4.8(a), in a TPA autocorrelator the two-photon absorption occurs in the photodetector itself and the autocorrelation trace is constructed from the induced photocurrent of the semiconductor detector similarly as in SHG autocorrelation as a function of the time delay [152]. For certain wavelength ranges, this method is a sensible alternative for SHG based autocorrelators, since nonlinear crystals are not required. However, the suitability of two-photon absorption autocorrelation (TPAAC) depends strongly on the spectral sensitivity of the detector, since the detector responsivity should be high for the 2ω light but minimal to the fundamental radiation at ω.

The theoretical peak-to-background signal ratio for TPAAC in a photodetector is 8:1, and since the beams propagate collinearly to the detector, interference fringes come out in the trace, if the beam paths are properly aligned. [153–155].

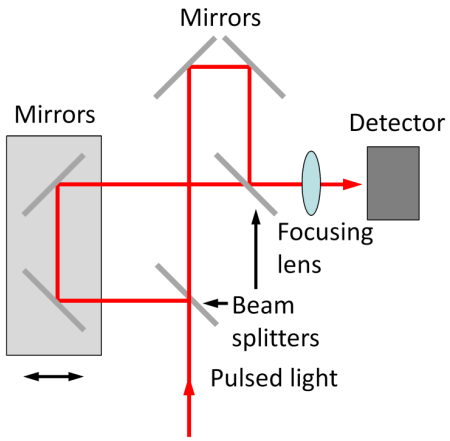

(a) Two-photon absorption autocorrelation. The two beams propagate co-axially into the detector, were two-photon absorption occurs.

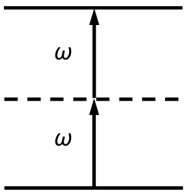

(b) Two-photon absorption. The energy of the photons is simultaneously absorbed into the medium, but no photons are emitted. The energy is released as a photocurrent in the detector.

Figure 4.8: Two-photon absorption autocorrelation. (a) illustrates the setup schematics of the device, and (b) gives the photon diagram.

4.5.2 Effects of optical fibers

Laser beams are often guided to the characterization devices through optical fibers. For short pulses this method can cause distortions, since dispersion and nonlinearity in optical fibers change the pulse properties. This section focuses on dispersion in optical fibers.

Frequency chirp

The refractive index of a material is frequency-dependent, which is the origin of chromatic dispersion. This means that frequency variations cause different spectral components to propagate at different speeds in a material. This group velocity dispersion (GVD) causes any pulse propagating in a dispersive medium, such as an optical fiber, to broaden in time [156].

Let us consider the propagation of an optical pulse represented as [141]

$$\tilde{E}(z,t) = \tilde{A}(z,t)\exp(j(k_0 z - \omega_0 t)) + \text{c.c.}, \tag{4.24}$$

where $\tilde{A}(z,t)$ is the slowly varying amplitude of the electric field, ω_0 is the central frequency and c.c. is the complex conjugate of the other term. In addition, the wave number $k_0 = n(\omega_0)\frac{\omega_0}{c}$ is proportional to the frequency-dependent index of refraction of the medium.

The time-dependent phase-shift of optical pulses is called chirp, and it causes the frequency of the radiation to change in time [157]. For example, the dispersion of

an optical fiber induces a pulse propagating in the fiber to become chirped. If the pulse is assumed to be Gaussian, the analysis of the propagation of a chirped pulse in an optical fiber can be done for the field [156, 157]

$$E(0,t) = A_0 \exp\left[-\frac{1+jC}{2}\left(\frac{t}{T_0}\right)^2\right], \tag{4.25}$$

where A_0 is the peak amplitude, C is the chirp factor and $T_0 = 2\sqrt{\ln 2}\Delta\tau_{\mathrm{p,G}}$ is the pulse width.

The instantaneous angular frequency of the pulse is the time derivative of the phase, and therefore, it becomes a function of time

$$\omega(t) = \frac{\mathrm{d}}{\mathrm{d}t}\left(\omega_0 t + \frac{C}{2}\frac{t^2}{{T_0}^2}\right) = \omega_0 + \frac{C}{{T_0}^2}t = \omega_0 + \Delta\omega(t), \tag{4.26}$$

where $\Delta\omega(t)$ is the time-dependent frequency shift i.e. chirp. The result of frequency chirp is presented in Figures 4.9(a) and 4.9(b), where an unchirped and chirped pulses are compared. In this case the pulse is experiencing a negative frequency chance and is said to be down-chirped. Correspondingly, a pulse with a growing frequency is called up-chirped.

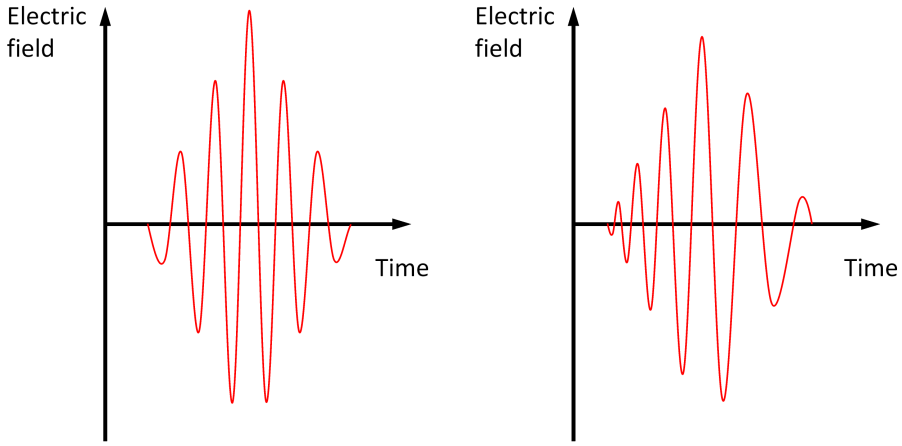

(a) Unchirped pulse. (b) Down-chirped pulse.

Figure 4.9: Electric fields of a non-chirped and down chirped pulses as a function of time.

A chirped Gaussian pulse retains its Gaussian form, but the width changes with the ratio [156]

$$\frac{T_z}{T_0} = \sqrt{\left(1 + \frac{C\beta_2 z}{{T_0}^2}\right)^2 + \left(\frac{\beta_2 z}{{T_0}^2}\right)^2}, \tag{4.27}$$

where β_2 is the GVD parameter. Therefore, even an originally transform limited pulse is strongly broaden in time. Figure 4.10 shows an example of dispersion in a

commercial single-mode fiber.

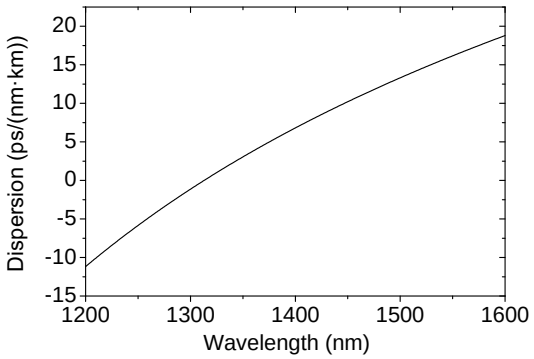

Figure 4.10: Dispersion versus wavelength in a common SMF-28 optical fiber. The zero dispersion wavelength is 1313 nm. [158]

An example of the effect of frequency chirp on interferometric autocorrelation is illustrated in Figure 4.11. In Figure 4.11(a) an autocorrelation trace of a non-chirped pulse is presented, and Figure 4.11(b) shows the same pulse with a frequency chirp. The wings of the pulse are bent upwards and the pulse width is shorter, which is typical for chirped pulses measured with an interferometric autocorrelator. On the other hand, as noticed during this work, even a few meter long standard single-mode fiber patch cord has enough dispersion to more than double a sub-picosecond pulse width at 2 µm.

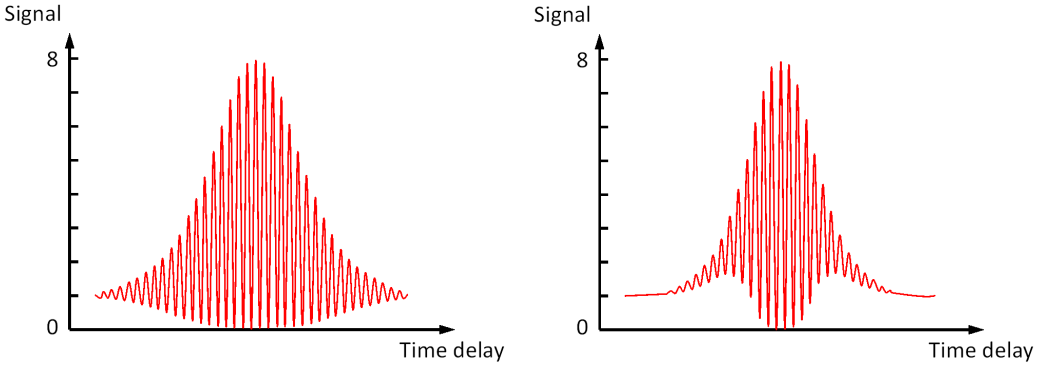

(a) Non-chirped pulse.

(b) Down-chirped pulse.

Figure 4.11: Interferometric autocorrelation traces of a non-chirped and chirped pulses.

Absorption

Figure 4.12 illustrates absorption profiles of some optical fiber types.

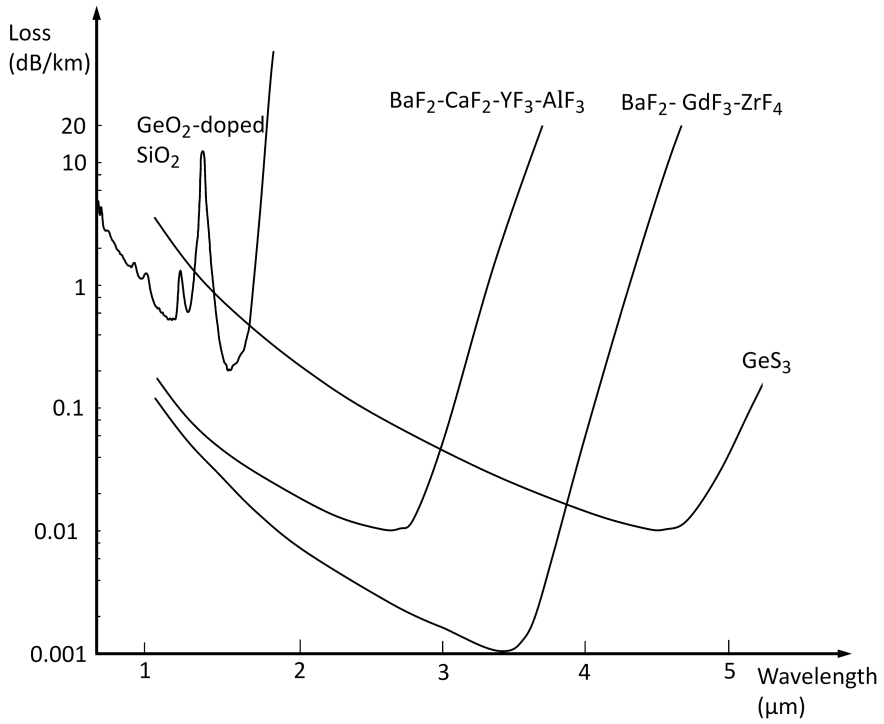

Figure 4.12: Absorption in different optical fiber types as a function of wavelength [159, 160].

Standars fibers made of fused silica[1] have an absorption minimum at 1.55 µm, but at longer wavelengths the absorption starts to increase rapidly [159]. As presented in Figure 4.12, fibers made from certain fluorides, chalcogenides or halides would theoretically have an extremely low damping factors of 0.001–0.01 dB/km in the 2–5 µm wavelength region compared to current minimum 0.2 dB/km at 1.55 µm. However, these materials are chemically so reactive and mechanically fragile that so far the efforts to fabricate a truly competitive fibre compared to SiO_2 have not succeeded [160]. The absorption in fused silica optical fibers can be a problem in measuring wavelengths at 2.5 µm and beyond when low powers are involved and high accuracy is required. In this work, absorption in standard fibers attenuated the signal enough to cause difficulties in measurements, and therefore free-space propagation had to be arranged.

[1]Amorphous, high purity SiO_2 is called fused silica. The designation originates from the synthetic reaction $SiCl_4 + O_2 \rightarrow SiO_2 + 2Cl_2$ [160].

4.5.3 Autocorrelator for 2 µm wavelength range

Autocorrelators for 2–3 µm wavelength range are commercially available, but they are expensive and not excessively sensitive. Therefore, based on the autocorrelation theory, a home-made device was fabricated.

The interferometric autocorrelator used in this thesis was based on two-photon absorption. A silicon detector was used, since the typical responsivity maximum of Si photodiodes is located near 1 µm, which suits well for the 2ω detection of 2.0 µm laser. On the other hand, the Si detector responsivity drops rapidly after the peak and thus the fundamental 2.0 µm emission was not detected and thus did not interfere the signal. The finished device is illustrated in Figure 4.13(b).

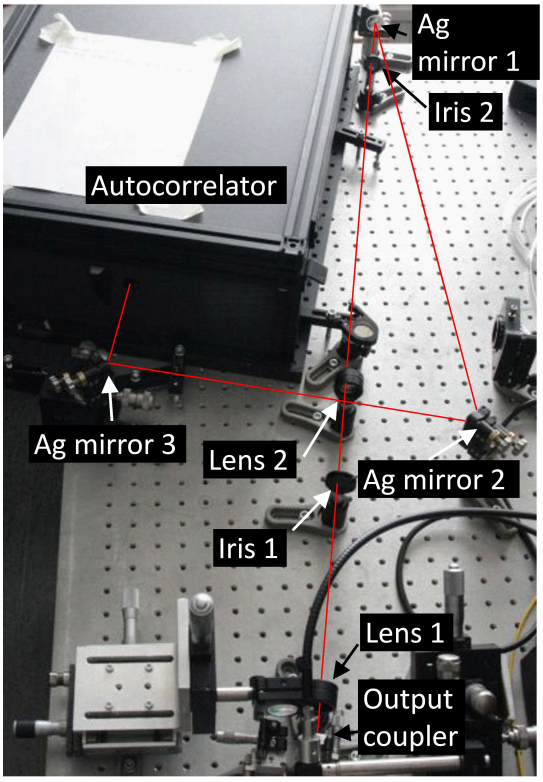

(a) Free-space guiding of the beam to the autocorrelator.

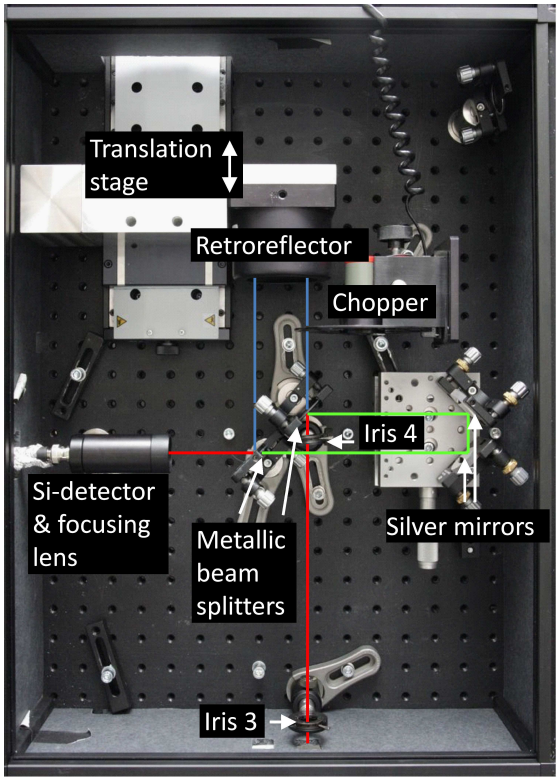

(b) Autocorrelator inside. Red line is the incoming beam. Green and blue lines represent the divided beam propagating in different arms, and the red line propagating into the detector is the combined beam.

Figure 4.13: Pictures of the autocorrelator

Device structure

The autocorrelator was originally built so that the laser beam was guided to the device using a single-mode optical fiber. It was later observed that the fiber induces a frequency chirp on the pulse and skews the pulse duration retrieved from the

AC data up to factor of 1.8 above the transfer limit [161]. To avoid fiber-coupling losses as well as dispersion and absorption induced in the fibre, the signal was later on directed to the autocorrelator by free-space optics as shown in Figure 4.13(a). Metallic mirrors were used to avoid dispersion.

As presented in Figure 4.13(b), the collimated beam passes partly through a metallic beam splitter in the autocorrelator. Therefore, the beam could be divided into two beams roughly equal in optical power and traveling in different arms. The reflected beam was re-directed to the detector by two silver mirrors.

The transmitted beam from the first beam splitter was guided back by a retroreflector, which was mounted onto a precision translation stage [162]. The retroreflector has three flat mirrors assembled into a cubic corner, and this structure causes the input beam to reflect backwards in a path parallel to the incoming beam path. Should the beam not arrive at the center of the reflector, a beam path shift in is generated. The new beam path is located at the opposite side of the retroreflector center in the direction between the center position and the original point of incidence. The gold coated mirror reflectivity for the used wavelength range is >94 % [163], so losses were moderate. The signals from both interferometer arms are combined at a second beam splitter and thus the two beams are co-axial as the arrive at the detector. The other arm length is adjusted with the translation stage, and thus the phase difference generated in the arms can be matched to zero.

Alignment of the device

The alignment of the autocorrelator optics is vital for the interference of the two beams to occur. It was realized that a small misalignment resulted in drop of the theoretical peak-to-background signal ratio of 8:1. An explicit misalignment resulted in intensity autocorrelation trace and the interference fringes disappeared leaving only the envelope of the profile. Any further misalignment led to loss of signal.

The alignment was done by first moving the retroreflector from minimum to maximum position; this way it could be ensured that the incoming beam is parallel to the translation stage axis. Then, by adjustment of the mirrors, the corresponding beam path from the loop arm was matched to the other so that in a few meters distance the beams coincided. Finally, this was double-checked by moving the retroreflector end-to-end.

Figure 4.14 shows how divergent the output beam from the mode-locked laser is. As presented in Figure 4.14(b), the mode diameter on the plane of incidence at the output coupler is approximately 0.6 mm, but already after 50 cm the beam had widened to 10 mm. Therefore, the beam was collimated with a two-lens-system (lenses 1 & 2 in Figure 4.13(a)) to an approximately constant diameter of 4 mm as simulated in Figure 4.15. The beam was focused onto the detector chip with a lens

inside the detector tube. The lens had a focusing length of 8 mm and a diameter of 8 mm. Hence, the whole beam was incident on the lens producing a sufficiently small focal spot under which the intensity was high enough for the TPA to arise.

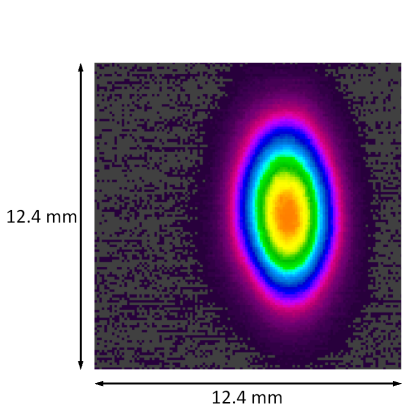

(a) Beam profile of a 2.0 µm mode-locked laser approximately 0.5 m after the laser output.

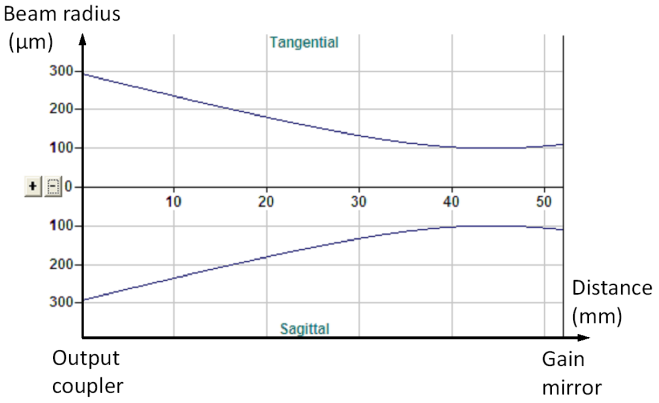

(b) WinLase-simulation of the mode/beam size (µm). Zero point on the x-axis is the output coupler end of the cavity, and the distance of 52 mm is from the gain mirror to the output coupler.

Figure 4.14: Output beam profile and simulated beam radius in the laser.

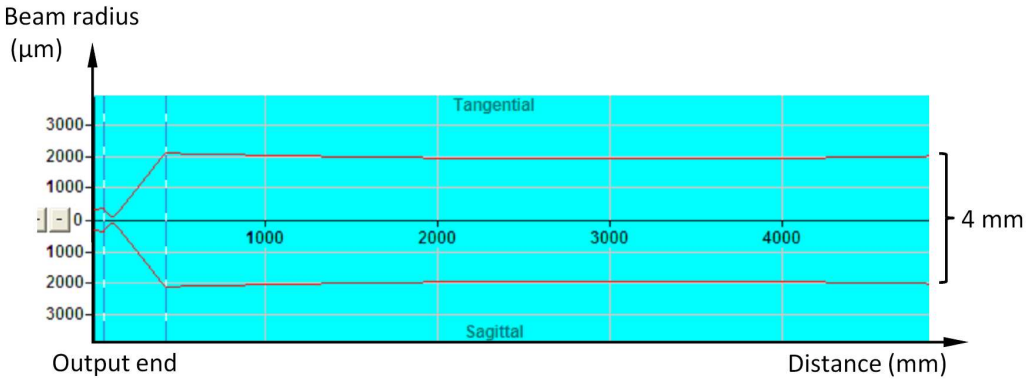

Figure 4.15: Collimation of the divergent, mode-locked laser beam with a two-lens system. Zero point on the x-axis (units in mm) is the output from the laser.

Silver (Ag) mirrors 1 and 3 were used to lift the beam from optical height of 75 mm to 95 mm, at the AC, being built on a 20 mm thick breadbord. Finally, Ag mirror 3 guided the beam into the AC. This reflection path also turned out to be flexible regarding testing of different SESAMs, since changing a new optical element always alters the alignment of the cavity and thus the output beam turns in different direction. Even if the optimizing adjustment of the new SESAM would not bring about an identical beam path to previous, the mirror system enabled controlling the beam into the AC in the correct direction by directing the beam through apertures

placed on the correct beam path. This could be done by simply monitoring the amplified detector signal with a multimeter.

The free-space propagation of the beam ensured efficient power for detection. After an electrical amplifier, the signal was even so strong, that an oscilloscope could be used to carefully complete the alignment. The translation stage was programmed to move the retroreflector back and forth so that by suitable selection of the oscilloscope trigger level, the autocorrelation trace could be observed from the oscilloscope screen. This way the peak-to-background ratio could be optimized with a few second response time.

Figure 4.16 shows an example of an autocorrelation trace measured with the device from a 1.55 µm fiber laser. The signal-to-noise ratio (SNR) for the device was considered as the quotient of the peak signal and the peak-to-peak amplitude of noise and it was estimated to be $SNR = 80$.

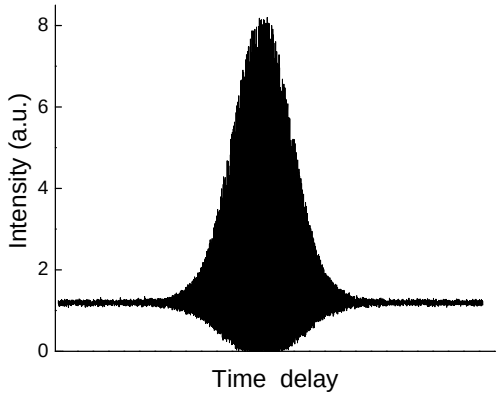

Figure 4.16: Example measurement with the autocorrelator.

Using the device

The autocorrelation signal from the detector was first voltage-amplified and then read with a lock-in-amplifier, which was triggered by the chopping frequency signal. The translation stage was driven by a LabView-software that also recorded the data from the lock-in-amplifier.

The signal from the detector after amplification was fed to a delay generator to reduce the amount of data points and to speed up the measurement. The translation stage's step size was 3.5 nm, which lead to 10 times the necessary amount of measuring points from a single oscillation (the fringes in the trace) at the 2.0 µm wavelength. The use of this pre-dividing factor reduced the measuring time by 90 % and still gave accurate results. Ultimately the measurement speed was limited by the bandwidth of the signal amplifier.

5. EXPERIMENTAL

5.1 Polarization-stabilized 2.35 µm semiconductor disk laser

In this setup, the polarization-stabilization of a 2.35 µm SDL based on GaSb material system was studied. The objective was to test whether a highly reflective Ge grating can be used as an output coupler in the laser and to control the laser's polarization. The laser was first built by using a dielectric mirror as the output coupler, and single transversal mode operation was adjusted. Then the output coupler was replaced with the Ge grating, and a comprehensive research on the grating effects was carried out.

5.1.1 Gain material

The gain material was grown on an n-GaSb substrate. The DBR consisted of 21.5 pairs of GaSb- and AlAsSb-layers, and the 320 nm wide stop band was centered at 2300 nm. The active region had three quantum well groups embedded in $Al_{0.3}Ga_{0.7}Sb$, each having three strained $In_{0.35}Ga_{0.65}AsSb$ quantum wells separated by narrow $Al_{0.3}Ga_{0.7}AsSb$ barriers. The window layer consisted of $Al_{0.85}Ga_{0.15}AsSb$ and it was capped with a thin GaSb layer. Room temperature photoluminescence peak for the quantum wells was observed at 2280 nm. A detailed structure of the gain mirror can be found in Appendix A.

5.1.2 Grating stabilized 2.35 µm laser cavity

The used v-shaped cavity is illustrated in Figure 5.1. The cavity was designed to have a nearly collimated beam between mirror M_1 and the Ge grating. The laser could be adjusted to single transverse mode operation by choosing $D_2 = 282$ mm. With this dimension the transversal laser mode size matched to the pump spot size on the sample. The distance from the gain mirror to the HR mirror M1 with a radius of curvature (RoC) of 150 mm was 85 mm. The sample included a heat spreader diamond that was AR coated.

The gain mirror was optically pumped with a commercial, fiber-coupled 980 nm diode laser. A maximum of 27 W of pump radiation was first collimated with a lens having 11 mm focal length and was then focused on the sample using a lens with $f = 10$ mm. The pump spot had a 230 µm diameter. The Ge-grating described in

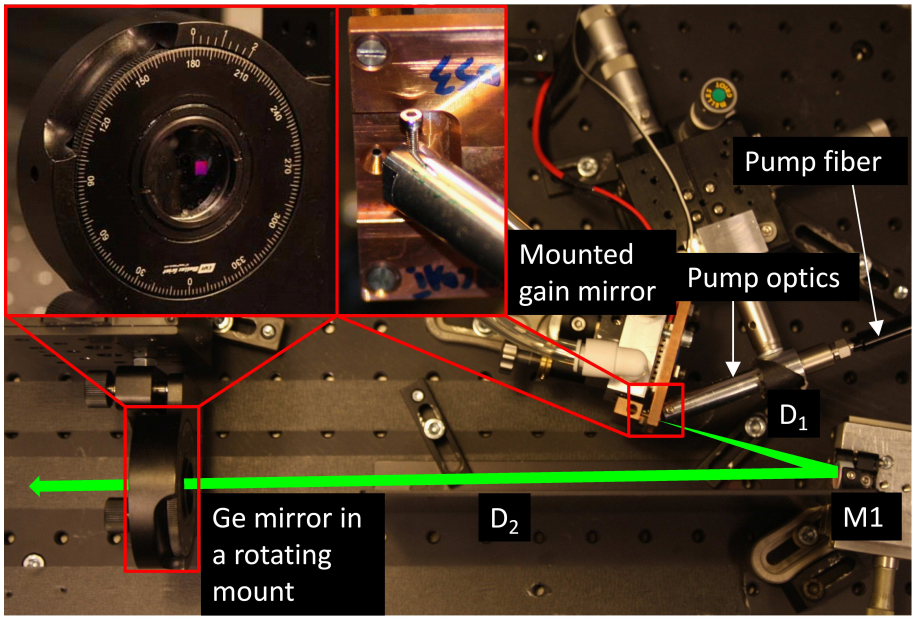

Figure 5.1: Grating stabilized laser setup. $D_1 = 85$mm, $D_2 = 282$mm.

the next subsection was attached to a rotating mount and was used as an output coupler. The simulated mode diameter on the grating and thus at the output was ~900 µm.

5.1.3 Grating characteristics

The Ge grating presented in Figure 5.2 was designed to provide a reflectivity of >95 % for TM-polarized (E-field and grating lines are perpendicular) light at wavelength range between 1850 nm and 3020 nm.

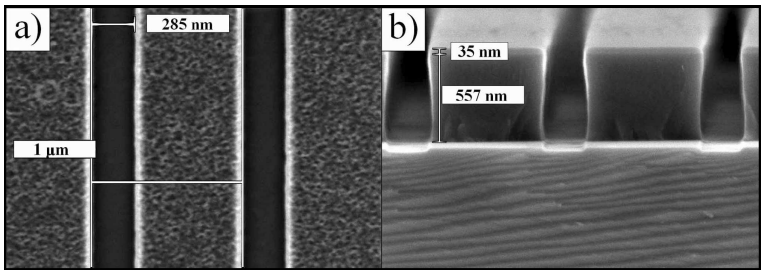

Figure 5.2: (a) Ge grating on a fused silica wafer imaged from above. The grating has a 1 µm period and a 285 nm groove width. (b) Cross section of the Ge grating on a Si wafer that was used in a reference sample to enable good cross-section quality for inspection of the etching profile. The Ge layer is 557 nm thick, and the 35 nm thick layer on top is a residual SiNx etch mask. Courtesy of Juha Kontio.

The grating was fabricated out of amorphous Ge by depositing a ~500 µm thick layer on a fused silica substrate. The grating pattern was fabricated using nanoimprint lithography (NIL). The grating period was 1 µm, and width of the grating

groove was 280 nm, corresponding to a fill factor of 0.72. The reflectivity profile of the grating for wavelengths 2300–2400 nm is presented in Figure 5.3. A broadband reflectivity graph and details of the design and manufacturing process can be found in reference [102].

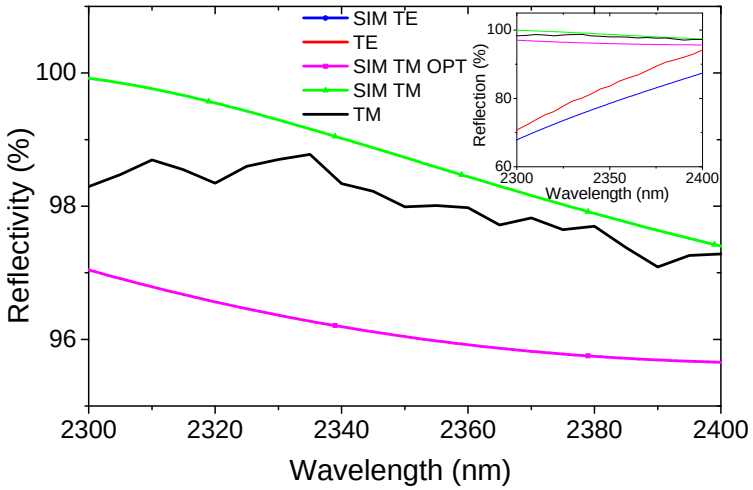

Figure 5.3: Ge grating reflectivity for TM polarized light in the band of interest. Inset: Both measured (solid curves) and simulated (dotted curves) grating reflectivity for TM and TE polarization. "SIM TM OPT" refers to TM polarization design). "TM" and "TE" were derived from IR-spectrophotometer transmission measurements. "SIM TM" and "SIM TE" spectra represent simulated reflectivities for the measured sample with the realized dimensions. Courtesy of Juha Kontio.

The measured reflectivity of the grating for TM polarized light varies from 97.65 % to 98.78 % at 2300–2400 nm. However, the power from the spectrophotometer light source could have been quite small at these wavelengths. Therefore, the grating reflectivity was measured more accurately with higher powers using the setup presented in Figure 5.4.

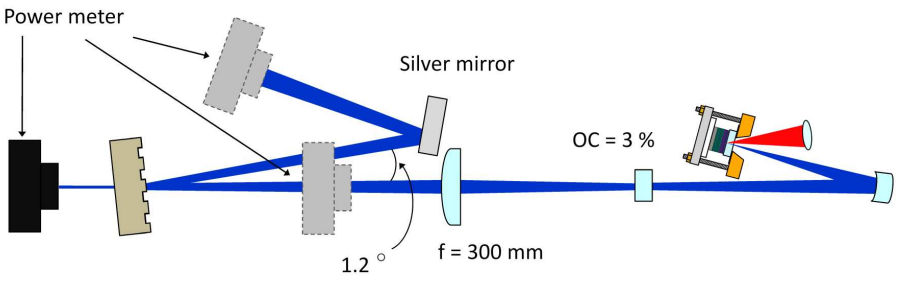

Figure 5.4: Setup schematics for grating reflectivity measurement at 2.3 µm.

The laser presented in Figure 5.1 was used as light source with the addition that an output coupler of 3 % was utilized instead of the Ge mirror. The emission was tuned to approximate output power of 300 mW, and the slightly divergent laser

beam was collimated using a lens with a focal length of 300 mm set to distance of 350 mm from the output coupler, which collimated the beam to a diameter of 1 mm. The grating was mounted into a three-axis translation stage and was placed on the collimated beam path. The reflected beam was again reflected from a D-cut silver mirror to enable small 0.6° incidence angle of the beam on grating. Prior to conducting the actual grating reflectivity measurements we wanted to determine the exact losses of the mirrors used in the system. This was essential to ensure the accuracy of the measurement. A measurement indicated a reflectivity of ∼97 % for the used silver mirror, which corresponds to an absorption of 8.7 mW with the used 300 mW power. Other losses were estimated to be ∼3 mW. According to WinLase simulation, beam diameter on grating was ∼1 mm.

Transmitted power from the grating was measured and compared to laser output power and reflected power from the grating. These actions were done for both TM and TE polarized light by first defining the linear polarization direction of the laser to be 150°. Therefore, the grating reflectivity for TM and TE polarized light could be measured by rotating the grating into angles 30° and 120°, respectively. Table 5.1 shows that the grating reflects 97.1 % of TM polarized and 85.4 % of TE polarized incident light at wavelengths 2330–2350 nm.

Table 5.1: Ge mirror reflectivity measurement data

Laser power (mW)	Transmitted power (mW)	Reflected power (mW)	Ag mirror absorption (mW)	Grating reflectivity (%)
TM polarization				
310	10	290	9	96.8
306	9	288	9.1	97.1
300	9	281	8.7	97.0
299	9	278	8.7	97.0
300	9	279	8.7	97.0
303	9	279	8.8	97.0
297	8	271	8.6	97.3
290	8	273	8.4	97.2
291	8	271	8.5	97.3
TE polarization				
306	44	265	7.9	85.6
299	44	268	7.7	85.3
300	44	267	7.7	85.3
294	44	264	7.5	85.0
295	44	261	7.5	85.1
296	45	264	7.5	84.8
289	41	260	7.4	85.8
292	42	263	7.5	85.6
290	41	262	7.5	85.9

5.1.4 Results and discussion

Characteristic comparison in terms of laser output power, optical spectrum and polarization between the grating and standard dielectric mirrors having reflectivities of 97 %, 99 % and 99.9 % was made. Using the grating as an output coupler wasn't straightforward, and a few actions to stabilize the laser behaviour needed to be done as new disconcerting properties arose.

Laser characteristics

Laser output power measured with a thermal power meter are shown in Figure 5.5. Measurements were made for different output couplers. A typical behaviour [164] of an increasing threshold pump power for lasing as a function of increasing output coupling ratio was observed.

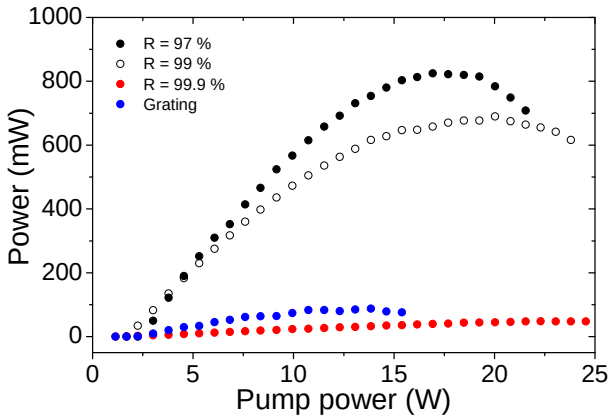

Figure 5.5: Output powers with different output couplers. The threshold pump powers for different output couplers were following: $R = 99.9$ %: 1.7 W, $R = 99$ %: 1.8 W,$R = 97$ %: 2.5 W, Grating: 2.2 W.

Emission spectra of the laser are presented in Figure 5.6. Etalon fringes with a free spectral range of 3.5 nm were observed. According to formula 2.34, the FP etalon is formed by the 300 µm thick heat spreader diamond.

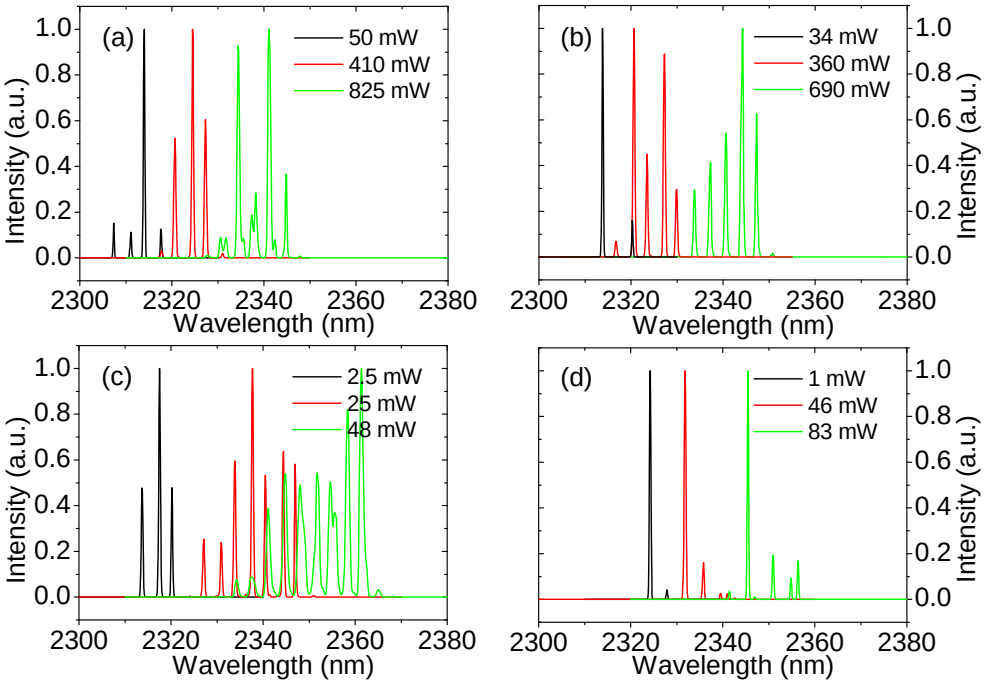

Figure 5.6: Optical spectrum with (a) $R = 97$ %, (b) $R = 99$ %, (c) $R = 99.9$ %, (d) Ge-grating. Different colors refer to different output powers.

Polarization stabilization

The polarization of the laser emission was measured by observing the laser power after a linear polarizer that could be freely rotated around the optical axis. Polarization of the laser emission was found to be linear with dielectric output couplers, although the polarization measurements for OC = 1 % were not performed since the power fluctuated significantly (tens of percents).

For the grating the measurement was done in different grating rotation angles (note that the beam location on grating was not the same with different angles). Figure 5.7 illustrates the polarization versus polarizer rotation angle.

The value with grating angle 75° was first considered to be a bad spot, but a retaken measurement of the polarization verified the direction.

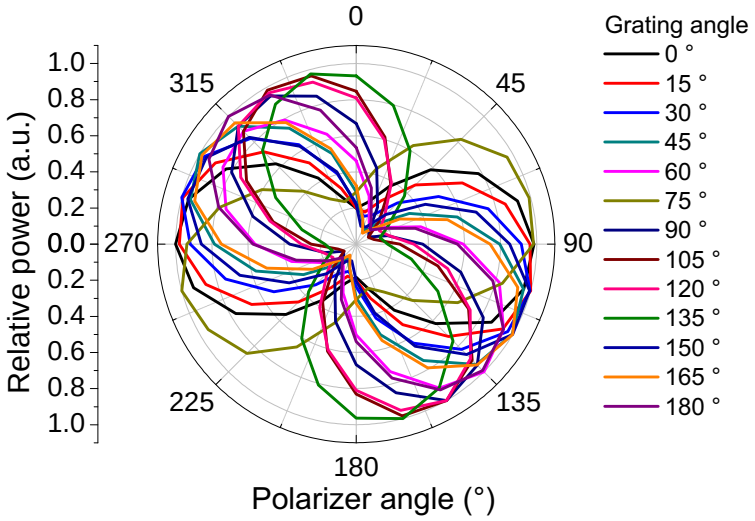

Figure 5.7: Measured polarization i.e. power with different grating angles after linear polarizer as a function of polarizer angle.

Output dependence on beam position on grating

The properties of the Ge-grating in terms of beam-location-dependent effect on polarization were also studied. In CW operation with grating rotation angle of 75°, the grating was slightly shifted in horizontal direction. As a result of the shift, a significant change in the beam profile was observed as can be seen in Figures 5.8(a) and 5.8(b). Most likely the phenomenon at issue is interference or scattering from the grating defects. However, this didn't affect the polarization of the laser, which indicates that polarization can be stabilized to a certain direction independent of the beam position on the grating.

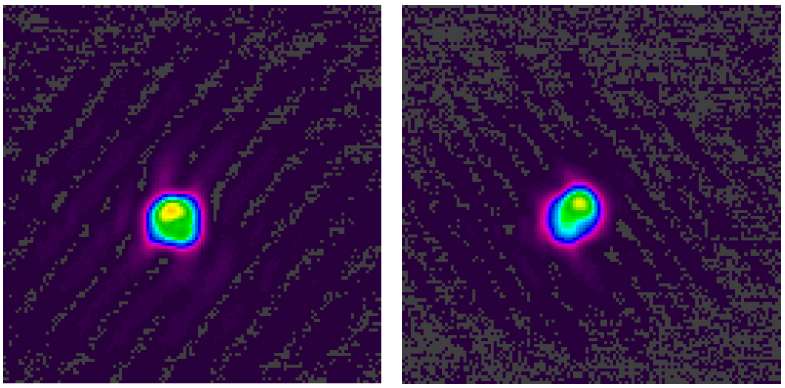

(a) (b)

Figure 5.8: Beam profiles before (a) and after (b) a vertical shift of the grating in angle of 75°.

The implantation of aluminium aperture

To avoid beam position fluctuation on the grating and to ensure rotation around the optical axis of the laser cavity, an aluminum piece with a 1.5 mm aperture was attached onto the substrate of the grating as presented in Figure 5.9.

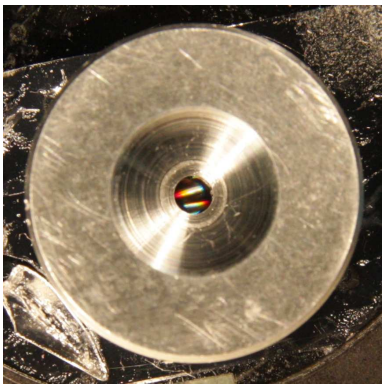

(a) Aluminium aperture on the Ge grating. The rainbow of colors show how the illuminating white light from opposite directions is diffracted by the grating.

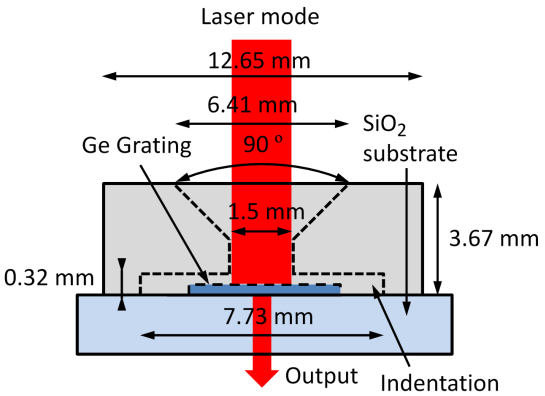

(b) Dimensions of the aluminium aperture.

Figure 5.9: Schematics of the aluminium aperture.

The aperture was relatively small, but due to the 3×3 mm^2 size of the grating a specific method for finding the exact beam position was necessary. The aperture element was fabricated out of a round aluminum disk, and it had an indentation which prevented direct contact to the grating. On the top side, surrounding the small aperture, the disc had an opening with edges machined at an angle of 45° to allow for easier cavity alignment. This way it could be made sure that the beam position on the grating remained about the same between grating rotations.

The measurement results for the polarization are shown on Figure 5.10. It can be seen that the polarization directions extend to a whole circle.

The aperture turned out to result in decreased output power of the laser, which could be caused by the mode-filtering effect of the aperture. A Gaussian beam with a 900 µm width has a $\frac{1}{e^2}$ width of 1.5 mm at 1.2 % of the peak, so the amount of incoming emission on grating is a bit smaller since the beam wings are filtered out. On the other hand, the aperture reduced non-directional reflections and scattering.

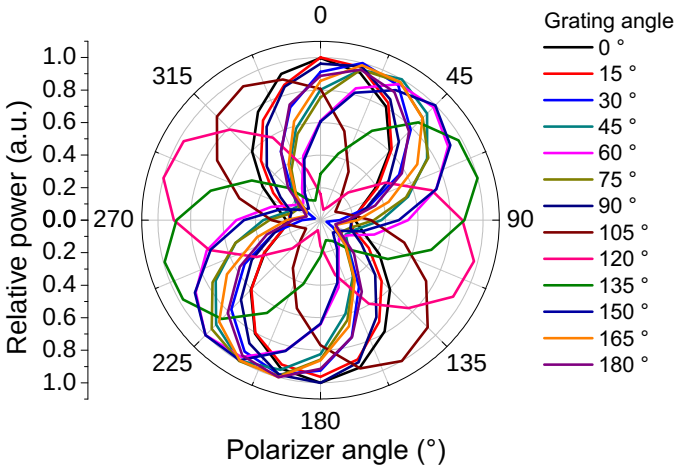

Figure 5.10: Measured polarization i.e. power at different grating angles after linear polarizer given as a function of polarizer angle.

The effects of the aperture were tested by first measuring the laser characteristics with the aperture and then without it. In Figure 5.11 one can see the spectrum with the aperture (black and red peaks) and without it. As a consequence of aperture removal the laser emission experiences a redshift of 6.5 nm.

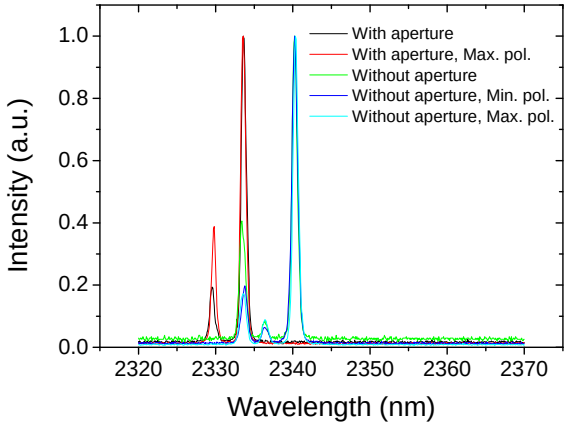

Figure 5.11: Emission spectra of the laser with and without the aperture on grating

Figure 5.12 illustrates the corresponding change in output power and polarization. Removing the aperture did not affect the polarization direction of the laser, although the polarization turned unstable and polarization ratio dropped by more than 50 %. Instead, output power multiplied and beam quality collapsed. Also the laser threshold decreased by 1.1 W.

As can be seen in Figure 5.13, the beam quality was extremely good when using the aperture, whereas without the aperture laser operates strongly multimodal. This is indicated by light output curve in Figure 5.12 and the beam profile in Figure 5.13(b). The aperture seems to operate as an effective mode filter, which facilitates

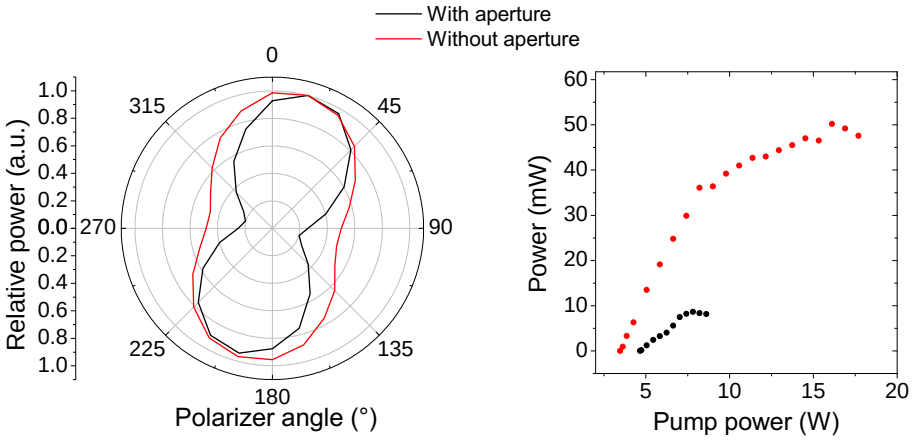

Figure 5.12: Emission spectra of the laser with and without the aperture on grating

achieving near single transversal mode operation.

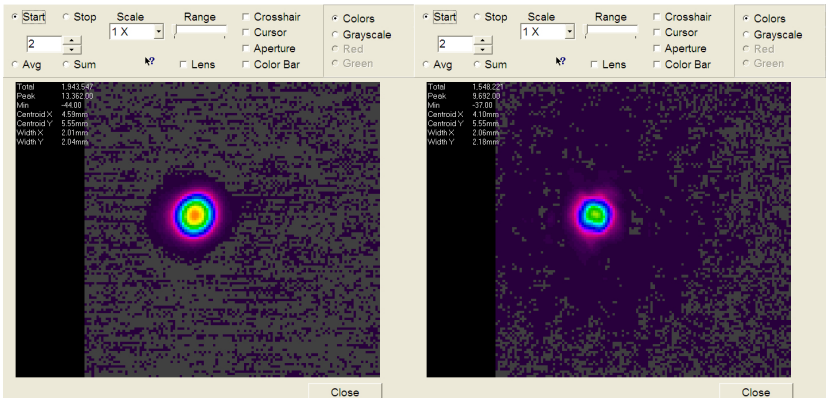

(a) (b)

Figure 5.13: Profiles of the laser beam with (a) and without (b) the aperture.

The polarizing effect of the Ge-grating was also tested by tilting the grating according to Figure 5.14. First, the direction of the fundamental polarization of the VECSEL was determined using dielectric mirrors as output couplers. The commercial linear polarizer was realized to have an offset of 5° with respect to rotating mount scale. The grating was placed as an output coupler and adjusted to angle of −20° so that the grating lines were perpendicular to the polarization direction (TM polarization). The grating was then tilted parallel to the grating lines, which caused a nearly negligible change of a few degrees in the direction of polarization. Also the polarization ratio remained the same.

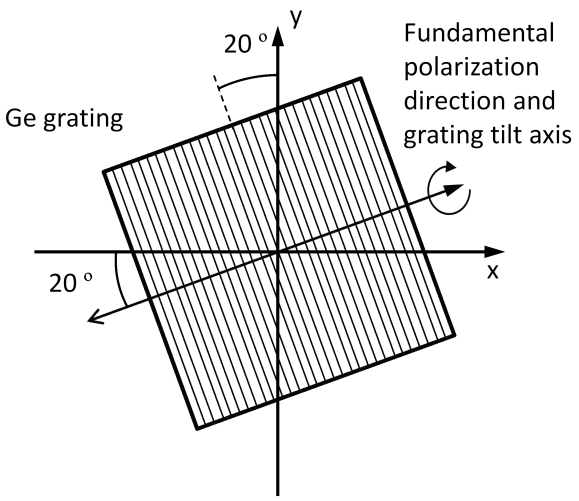

Figure 5.14: Tilting the Ge grating. The grating was aligned so that the grating lines were perpendicular to the direction of fundamental polarization of the laser (TM polarization). The tilt was done around this very axis.

Antireflective coating

The ratio between different polarization was 1/8 in average, so the polarization selection isn't perfect, even though the reflectivities for TE and TM polarizations have a difference of 12 percentage units. This indicates that TE polarization is amplified by feedback additional to that reflected from the grating. This could be a consequence of the glass substrate's reflecting back surface, which could cause an adequate feedback for the TE polarization to strengthen. With TM polarization this phenomenon would not appear so intensely due to difference of 12 percentage unit in reflectivity. As a smaller amount of TM polarized light compared to TE polarized penetrates the grating, also a smaller amount is fed back to gain medium. Therefore, the back surface of the substrate was AR coated, but this didn't clearly improve polarization extinction ratio despite the nearly perfectly succeeded coating. Instead, the coating resulted in a great improvement of the polarization direction behaviour.

Figure 5.15 shows the consistency of polarization direction with respect to grating rotation. The polarization of the laser was first measured with 180° rotation in 15° steps. Later on, the same measurement was repeated with a full circle turn. The behaviour is surprising at grating angles 15–60°, since the polarization direction rotates in the opposite direction as the grating. Then, in angles 105–150° the polarization direction certainly follows the grating rotation in the right direction, but the change in polarization direction is as large as 30–45°. Figure 5.16 shows examples of the spectral variation of laser emission with respect to grating angles. It can be seen, that at these four angles there practically are no wavelength shifts, so the phenomenon doesn't occur due to spectral changes in laser emission, since

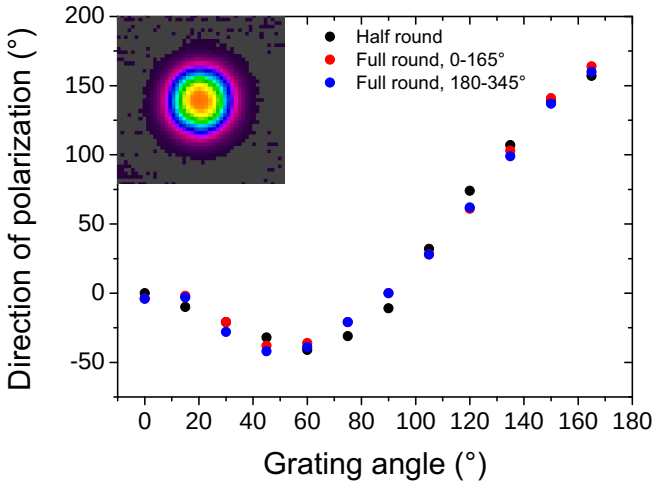

Figure 5.15: Direction of polarization as a function of grating rotation angle. The measurement was done after AR coating, with the aperture on the grating. An example of a beam profile is given.

the grating reflection doesn't seem to have strong variations in these wavelengths.

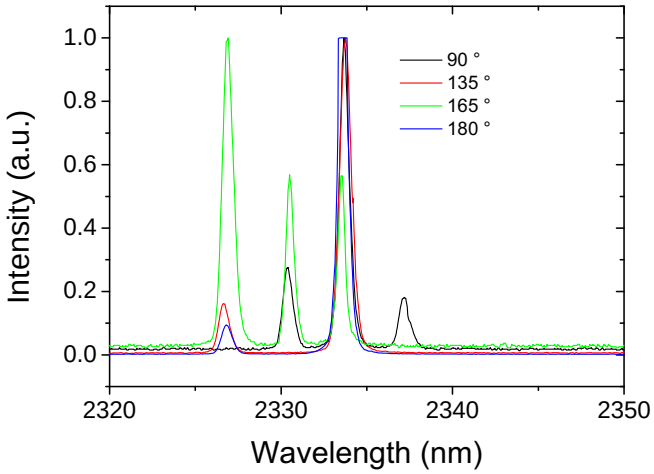

Figure 5.16: Laser emission spectra with Ge grating at various angles.

Implications

The polarization ratio wasn't as good as theoretically expected, and lasing in all grating angles and polarization directions such extensively between 0–180° was surprising. Reflectivity of 85 % should be too low to provide enough feedback for the gain medium to lase, although the lasing threshold is lower for the TE mode [165]. Figure 5.17 presents measured power corresponding to TM polarization as a function of Ge grating rotation. The data points form an oscillating function with a

period of 90°, which indicates that output coupling varies with respect to grating angle.

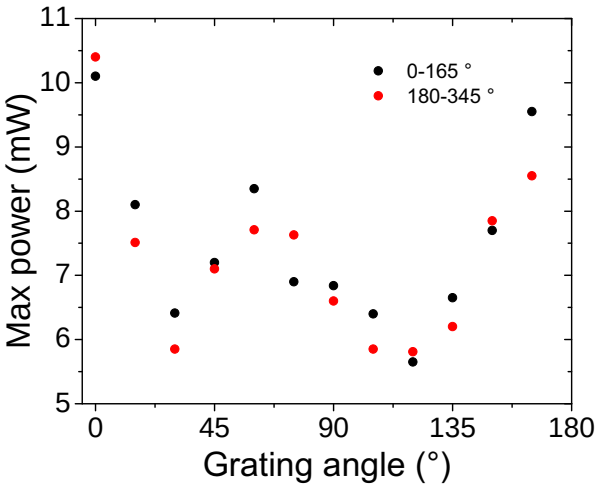

Figure 5.17: Maximum powers from the laser with different grating angles after a linear polarizer.

The considerably strong power fluctuations noticed in the polarization measurement with the 99 % mirror could be explained by the diamond birefringence. An imperfect alignment on the optical plane of the laser could bring about a near-ring-shaped cavity, if the returning beam doesn't completely arrive at the original mode area on the gain medium. In this case, the circulating wave could experience a phase retardation in polarization at each round trip [94]. In a linear cavity this effect on polarization doesn't exist, since the emitted and returning beams overlap and due to the opposite directions, the nonlinear phase retardations cancel each other out. However, here the laser cavity includes discriminative elements, the gain medium and the Ge grating, that actively effect the polarization. Therefore, the polarization state of a cavity mode is different when emitted through the heat spreader diamond and reflected backwards after a cavity round trip. This fact together with a slight misalignment in the cavity plane is surely to cause extraordinary phenomena.

The polarizer was tilted so that a possible feedback from the polarizing film was excluded. With HR mirror the polarization extinction ratio was only 1:4, but with the 97 % mirror the ratio was 1:211. The dielectric mirror coatings were measured with a spectrofotometer to see the coating properties with different polarizations, but this didn't provide any informative results. The laser was alos tested with higher cavity losses, and lasing was observed with 5 % output coupling. The laser gain was not tolerant for even higher losses that could have explained the behaviour.

Despite the complex behaviour of the Ge grating, stable laser operation was achieved. In the end, the polarization selectivity of the grating was consistent, although the development required intuitive ideas to enhance the laser properties

and cancel the interfering effects of the Ge grating. As the grating design is still at an early phase, these results are truly promising. Learning and understanding the cumulative interactions between the different laser cavity elements will make it easier to design a grating with excellent polarization extinction ratio. The crucial points realized in this work can be taken into account in the future when aiming for even better operation, and a further step is to improve the wavelength selective properties of the Ge grating to induce wavelength-locked, narrow-band emission.

5.2 Passively mode-locked 2.0 µm semiconductor disk laser

This chapter presents a laser setup, in which a 2.0 µm GaSb disk laser was passively mode-locked with a fast SESAM. As far as I can tell, sub-picosecond pulse operation in a passively mode-locked GaSb SDL had not been demonstrated before the beginning of this work, and the objective was to study the possibilities of the GaSb material system to produce ultrashort pulses in mode-locked SDLs. The obtained pulses were measured with an autocorrelator built during this work.

5.2.1 Structure of the gain mirror

The gain mirror was grown on an n-doped (100)-oriented GaSb substrate. First a GaSb buffer layer was grown on top of the substrate. The buffer layer was followed by a distributed Bragg reflector that included 18.5 pairs of lattice matched AlAsSb/GaSb $\lambda/4$-layers and had a theoretical reflectivity of 99.9 %. The gain region had five equally spaced groups of $In_{0.2}Ga_{0.8}Sb$ quantum wells. Each group included three 8 nm thick QWs embedded in GaSb, resulting in total of 15 QWs in the resonant periodic active region. A lattice matched $AlAs_{0.08}Sb_{0.92}$ window layer and a thin GaSb cap layer completed the gain mirror structure. A micro-cavity with an optical thickness of 3-λ was thus formed between the DBR and the window layer. The total thickness of the window and cap layer was $\lambda/4$. A detailed structure of the gain mirror can be found in Appendix A.

A chip of gain material with a size 2.5 mm × 2.5 mm was capillary bonded to a wedged diamond heat spreader sized 3 mm × 3 mm × 0.25–0.35 mm. Finally, a two-layer TiO_2/SiO_2 AR coating was evaporated on the heat spreader to avoid surface reflections.

5.2.2 Semiconductor saturable absorber mirror structure

The SESAM with a reflectivity presented in Figure 5.18 had an antiresonant design comprising three $In_{0.29}Ga_{0.71}Sb$ QWs embedded within GaSb layers. An estimated modulation depth of the SESAM was in the range of 1.5–2 %. A detailed structure of the SESAM can be found in Appendix B. A pump-probe system at Max Born

Institute for Nonlinear Optics and Short Pulse Spectroscopy, Berlin, was used to determine the absorption recovery time. Since the system had a low measurement sensitivity, reliable characterization data for the SESAM incorporating only three QWs could not be obtained. Therefore, mirrors incorporating six and ten QWs were used in recovery time measurements to give an estimate. These mirrors had a higher modulation depth, with otherwise similar composition as the slightly ion-irradiated SESAM used in the mode-locking experiments. The measured pump-probe recovery trace is illustrated in Figure 5.19.

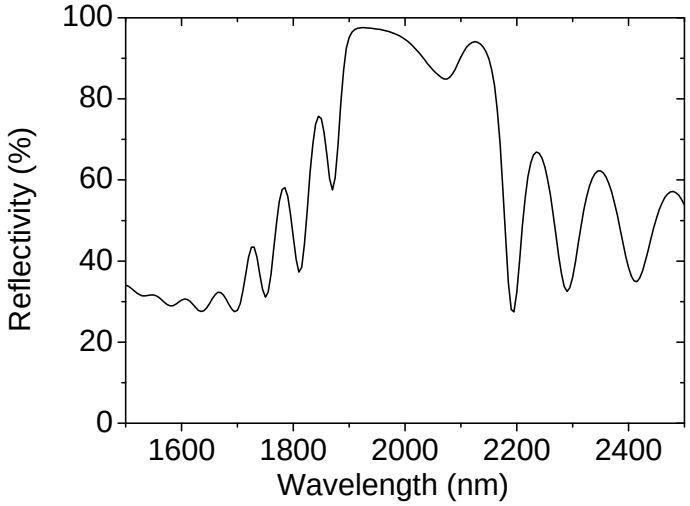

Figure 5.18: Reflectivity of the SESAM measured with a spectrophotometer. Courtesy of Riku Koskinen.

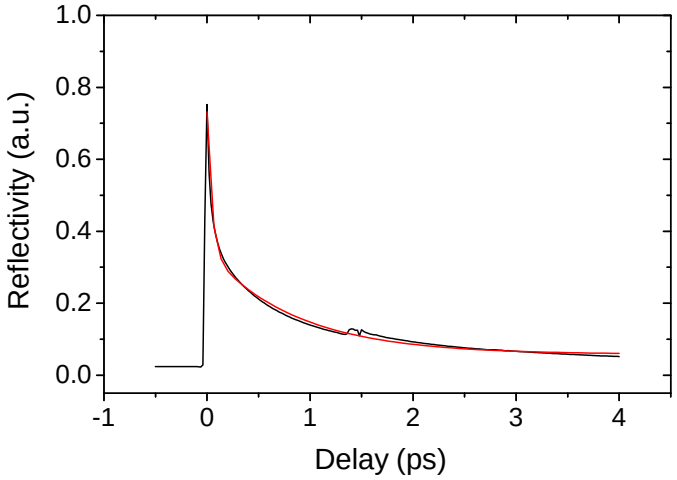

Figure 5.19: A measured pump-probe recovery trace from a six quantum well test sample. Double exponential fitting (red curve) has a fast time component of 0.53 ps and a slow time component of 9 ps. Insufficiently suppressed spurious reflections in the pump-probe setup caused the two small peaks at about 1.5 ps delay.

The source was an idler wave of a Spectra Physics Opal optical parametric oscillator (OPO) tuned to 2.0 µm. The average power from the source was about 150 mW with a 80 MHz repetition rate, and the 150 fs pulse duration corresponded to about 2 nJ in pulse energy. Estimated pulse fluence was less than 60 µJ/cm^2. On this basis, the absorption recovery time was estimated to have a fast time component of 0.53 fs and a slow component of 9 ps, which indicates a high speed of the SESAM.

5.2.3 Setup for mode-locked 2 µm laser

The gain mirror bonded to a diamond heat spreader was clamped to a copper heat sink and the temperature was kept at constant 15°C with a Peltier element. The gain mirror was optically pumped with a spot of a diameter ∼230 µm using a commercial 980 nm diode laser. According to simulations, the laser mode diameter on the SESAM was ∼25 µm in diameter. The setup is illustrated in Figure 5.20. The distance from the gain mirror to the concave, HR focusing mirror (M1, RoC = 25 mm) was D_2 = 103 mm. The optimal focus distance from mirror to the SESAM was about $D_3 = 14$ mm. The concave output coupler with RoC = 50 mm, reflectivity of 99 % and a $D_1 = 51$ mm distance from the gain mirror completed the z-shaped cavity with a total length of ∼16.8 cm.

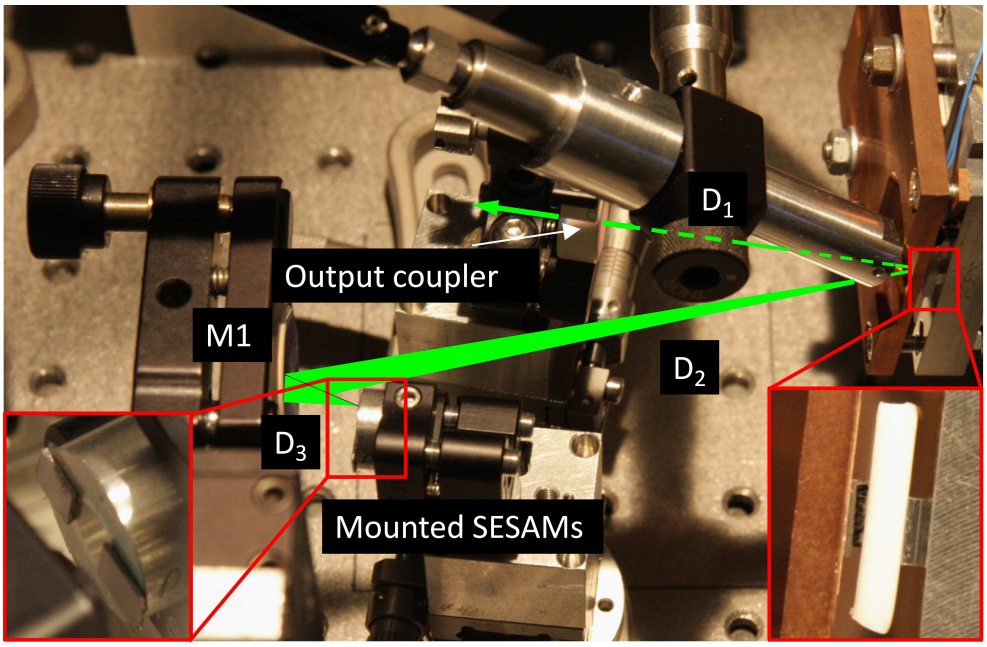

Figure 5.20: Picture of the mode-locked laser. The two different SESAMs were attached to the same mount to enable flexible change of sample, and only the other one is acting as a cavity mirror.

Due to the invisible IR wavelengths used in this work, a 532 nm green laser pointer was used in the alignment procedure of the beam into the autocorrelator. The path of the long-wavelength laser beam was first determined with the use of

Pyrocam III and apertures (irises 1 and 2 in Figure 4.13(a)). Then, the laser pointer was aligned through the apertures, and finally, with the Pyrocam, the beams were double-checked to travel on the same path.

5.2.4 Results and discussion

Mode-locking was initiated at ∼6.6 W of pump power as seen in Figure 5.21(b). The power-output curve shows a hysteresis typical to many mode-locked SDLs. The steep rise in power and the initialization of mode-locking arises from sudden bleaching of the saturable absorption as the net gain exceeds cavity losses. Even when the pump power is decreased below the initial threshold, stable mode-locking is sustained until the pump power is insufficient to hold the minimum radiation density to keep the absorption of the SESAM bleached [166].

The optical spectrum of the mode-locked laser with a Gaussian fit is shown in Figure 5.21(a). The FWHM of the emission band was estimated to be 11.5 nm. Spectral measurements in radio frequencies (RF), presented in Figure 5.22, revealed a fundamental repetition rate of 890.4 MHz, which corresponds to a round trip in the 16.8 cm long cavity.

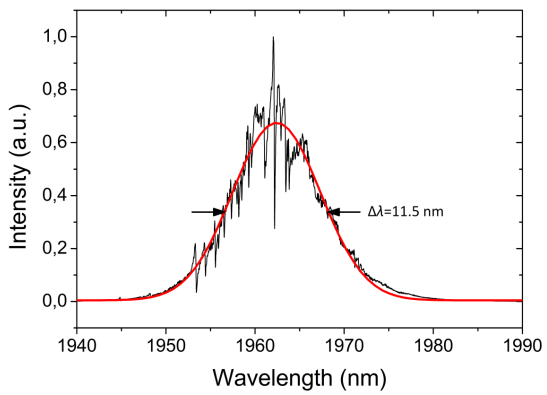

(a) Optical spectrum of the mode-locked laser with a Gaussian fit (red curve).

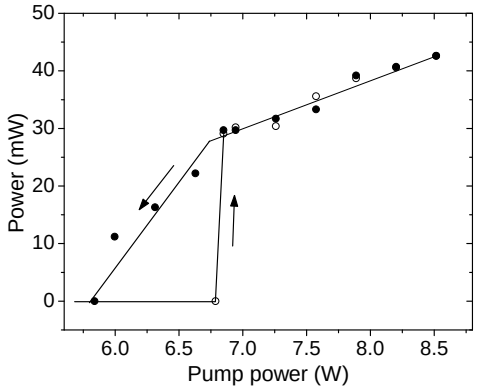

(b) Output power from the mode-locked laser as a function of pump power. Arrows demonstrate the direction of pump adjustment.

Figure 5.21: Optical spectrum and light output characteristics of the mode-locked 2.0 µm laser.

The obtained autocorrelation trace measured at 35 mW of output power is shown in Figure 5.23. It can be seen that the trace correlates well with the theoretical ratio of 1:8.

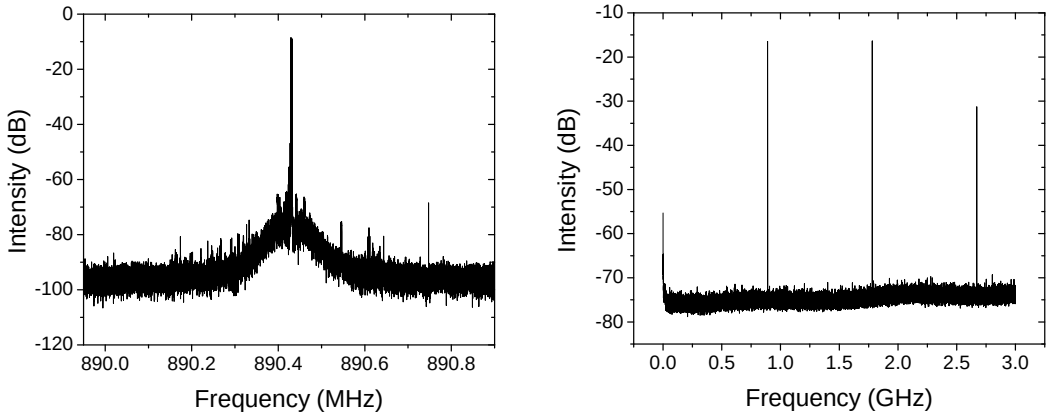

(a) RF spectrum of the mode-locked laser emission.

(b) Widescan RF-spectrum.

Figure 5.22: Radio frequency spectrum of the mode-locked laser.

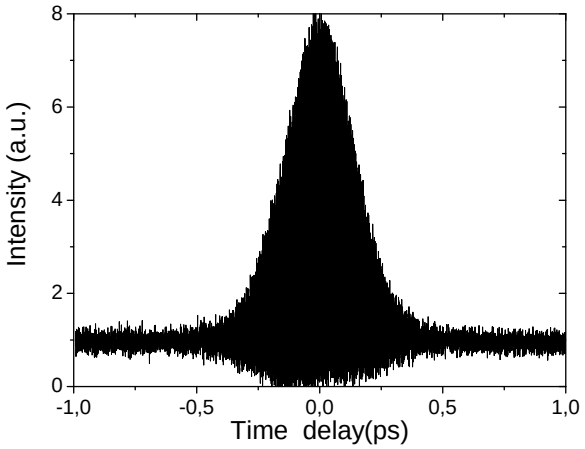

Figure 5.23: Measured interferometric two-photon absorption autocorrelation trace of a pulse from the 2.0 µm mode-locked laser.

The reconstructed pulse and the corresponding bandwidth and Fourier limits are presented in Figures 5.24(a) and 5.24(b), respectively. The estimated pulse duration is 415 fs, which is a factor of 1.10 times the Fourier limit. During the writing process of this thesis, even shorter, 381 fs pulses being within only 2 % above the Fourier limit were obtained from this laser [17]. The pulse duration was surprisingly close to the Fourier limit determined by the spectrum, since the only efforts to avoid pulse broadening due to fiber dispersion were done by using free-space propagating beam and metallic mirrors.

Testing the cavity in CW operation

The output power from the mode-locked laser was surprisingly low. In an optimal cavity, the mode diameter pump on the gain and the pump spot match, and

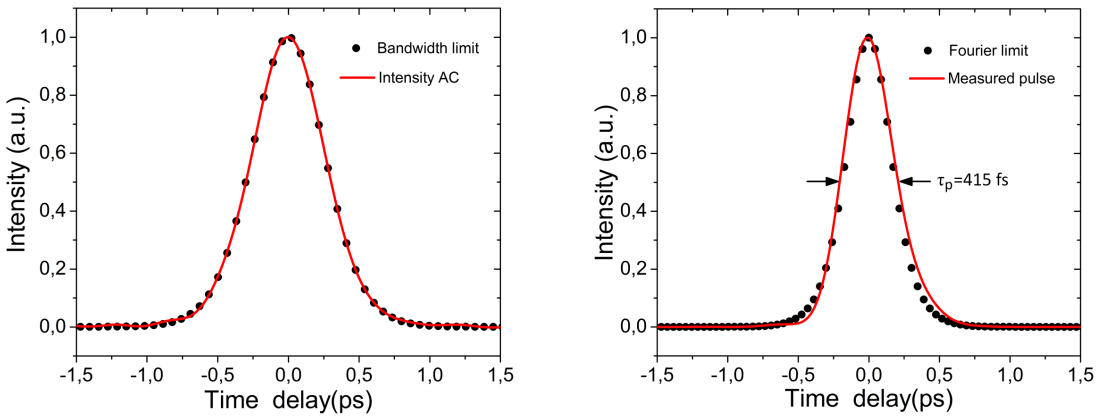

(a) Dots present the intensity autocorrelation retrieved from the interferometric autocorrelation data. Red curve is the bandwidth limit of the pulse calculated from the optical spectrum.

(b) Red curve plots the shape of the optical pulse, and the corresponding Fourier transform limit is defined by the dots.

Figure 5.24: Calculated intensity autocorrelation and reconstructed pulse shape.

correspondingly the mode diameter on the SESAM is equivalent to the optimal. Therefore, the reason for the modest power performance might be a slight mismatch in the cavity design, and in order to analyze the cavity dimensions, the SESAM was replaced with a HR mirror. The maximum output powers were measured with different cavity lengths i.e. by changing the location of the HR mirror. The cavity length was monitored with the RF spectrometer, which enabled adjusting the HR mirror position very accurately with respect to the original SESAM position.

The output powers shown in Figure 5.25 were measured at different HR mirror positions, roughly in 0.17 mm steps on the optical axis. It can be seen, that the maximum CW output power is achieved with >50 µm displacement of the HR mirror with respect to the SESAM position in mode-locked operation. Presumably, the optimal position of the SESAM for pulsed operation differs from that for optimized output power.

The optimization of the cavity design was not performed in this thesis, although it could be possible by just adjusting the cavity dimensions and pump optics without the need to change the cavity elements. On the other hand, the small RoC of the focusing mirror causes the mode diameter on the SESAM to change quickly with respect to axial movement. In addition, a change in SESAM position affects strongly to the mode diameter on the gain. To overcome this fine-tuning, a cavity design with different mirrors might be compulsory, and thus achieving the aforementioned optimal cavity design might not be such a straightforward procedure in the end. In any case, the prospective optimization is likely to result in output powers higher than 100 mW.

It is also possible, that due to the short recovery time of the SESAM's absorption,

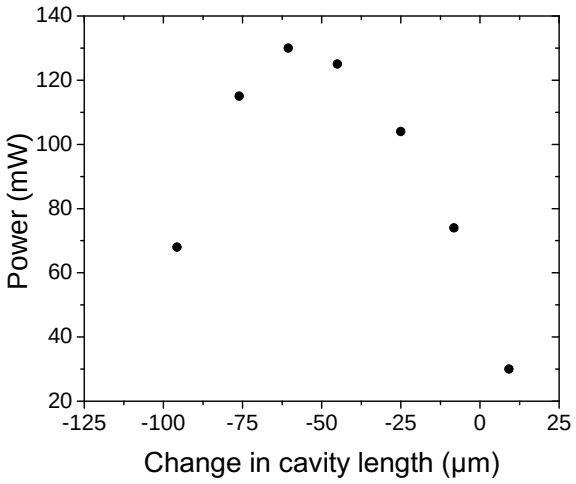

Figure 5.25: CW power given as a function of the HR mirror position, relative to the original SESAM position. Zero change in cavity length denotes that the HR mirror position was matched to that of the SESAM in the mode-locked laser.

the stored energy in time is low. Therefore, between the pulses the upper excited state is already relaxed before the next pulse has reached the gain region. In this scenario, a lot of pump energy is lost in time, and by increasing the pulse repetition rate i.e. by shortening the cavity, the average power could be increased, since the 'off-state' would be short.

6. CONCLUSION

6.1 Use of Ge gratings based on guided-mode resonance

In this work, the use of a novel Ge grating as an output coupler in a 2.35 µm GaSb semiconductor disk laser was studied. A polarization-stabilized emission was obtained, which resulted in polarization selectivity by a simple rotation of the grating.

The rotation of the polarization didn't follow the grating angle linearly as intuitively expected. This is likely due to interplay of effects including gain coupling to different polarizations, birefringence of the diamond and polarization selectiveness of the grating. The flat silica substrate of the Ge-grating was noticed to cause polarization instability due to reflections from the back surface. This problem could be diminished by coating the surface with an AR film, but a more confident method would be to use a wedge substrate with AR coating in order to reduce direct feedback. In the end, it was shown that the polarization of an SDL can be stabilized with a Ge grating despite the complex interactions.

Ge has all the properties of a well-suitable material for low-cost, easily processable optical components in the IR range. The fabrication allows for integration with any photonic element with a flat surface, and therefore Ge gratings could be used spectrally selective components fabricated on top of the SDL gain mirror. Nanoimprint lithography technique is a versatile method for extremely accurate, repeatable processing with low costs and scalability up to industry volumes. The possibility of high refractive index contrasts among with the scalability of the wavelength design and NIL grating fabrication make Ge-gratings an attractive solution for several IR applications.

All the attributes of the Ge grating could not be fully explained yet, but the characteristics of the laser were improved throughout the work by eliminating disruptive phenomena one by one. In the end, the laser showed consistent performance and the expected conveniences brought about by the grating mirror. Considering that the Ge mirror was originally not designed to be used as a laser mirror, the results obtained in this work show that grating mirrors are to be reckoned with as complementary alternatives for dielectric mirrors in specialized applications. A careful and more specific bandwidth design of the grating would no doubt lead to better performance in terms of power and achieving single-mode, linearly polarized operation with excellent polarization ratio.

6.2 Mode-locked GaSb-lasers

The study carried out in this work was a part of a research project, that lead to the first passively mode-locked GaSb SDL producing femtosecond pulses. The pulses were even surprisingly short, considering that the technology of the mode-locked lasers based on GaSb material system is relatively immature. Developing a high-quality, fast SESAM has been challenging and thus the results achieved in this work are truly encouraging. Furthermore, the quality of the pulses is astonishing as the pulse width is very close to the bandwidth limit of the laser in spite of the pulse broadening effects like dispersion and nonlinear processes that could take place in the system.

The cavity design turned out to be a contributing factor to the rather modest power level of the laser. Simultaneous matching of the laser mode diameters on the SESAM and the gain mirror to the optimal values might bring about output powers higher than 100 mW with the very cavity elements. In addition, more intense pumping could broaden the gain spectrum and thus broaden it, which would lead to even shorter pulses. The very fast recovery of the SESAM's absorption might also be a factor in low average power due to lost pump power between consecutive pulses. An increase in pulse repetition rate could result in higher average power level.

To summarize, the GaSb material system has proven to be a very notable tool in developing lasers in the wavelengths around 2 µm, and the study made in this work is to be extended to longer wavelengths. Mode-locking at the 2.35 µm wavelength was tested during this work, but so far stable pulses were not obtained. The ambition is to develop a system able to produce similar performance as the 2.0 µm laser.

6.3 The culmination

This work was a part of research that has been on wide view in the scientific community. Results obtained from the mode-locked 2.0 µm laser studied in this work have been published in several occasions [17, 39, 167], and they were given recognition by selecting one of the reports as the topic of a featured article [168]. The study on the polarization-stabilized 2.35 µm laser is to be submitted for publishing as well in the near future. This visibility has been a result of hard and intuitive efforts taken from the backbones of the research group, which is an encouraging motivator to continue the research and take even bigger steps in the future.

BIBLIOGRAPHY

[1] J. P. Gordon, H. J. Zeiger, and C. H. Townes, "Molecular microwave oscillator and new hyperfine structure in the microwave spectrum of NH_3," *Physical Review*, vol. 95, no. 1, pp. 282–284, 1954.

[2] J. P. Gordon, H. Zeiger, and C. H. Townes, "The maser-new type of microwave amplifier, frequency standard, and spectrometer," *Physical Review*, vol. 99, no. 4, pp. 1264–1274, 1955.

[3] A. Einstein, "Zur Quantentheorie der Strahlung," *Physikalische Zeitschrift*, vol. 18, pp. 121–128, 1917.

[4] O. Svelto, *Principles of Lasers*, 4th ed., D. Hanna, Ed. Springer Science+Business Media, Inc., 1998.

[5] G. R. Gould, "The LASER, Light Amplification by Stimulated Emission of Radiation," in *Proceedings of The Ann Arbor Conference on Optical Pumping, Washington, DC*, 1959.

[6] T. H. Maiman, "Stimulated optical radiation in ruby," *Nature*, vol. 187, pp. 493–494, 1960.

[7] A. Godard, "Infrared (2–12 µm) solid-state laser sources: a review," *Comptes Rendus Physique*, vol. 8, no. 10, pp. 1100–1128, 2007.

[8] N. Schulz, J.-M. Hopkins, M. Rattunde, D. Burns, and J. Wagner, "High-brightness long-wavelength semiconductor disk lasers," *Laser & Photonics Reviews*, vol. 2, no. 3, pp. 160–181, 2008.

[9] F. Tittel, D. Richter, and A. Fried, "Mid-infrared laser applications in spectroscopy," in *Solid-State Mid-Infrared Laser Sources*, ser. Topics in Applied Physics, I. Sorokina and K. Vodopyanov, Eds. Springer Berlin / Heidelberg, 2003, vol. 89, pp. 458–529.

[10] C. J. Fecko, J. D. Eaves, J. J. Loparo, A. Tokmakoff, and P. L. Geissler, "Ultrafast hydrogen-bond dynamics in the infrared spectroscopy of water," *Science*, vol. 301, no. 5640, pp. 1698–1702, 2003.

[11] H. Sumizawa, H. Yamada, and K. Tonokura, "Real-time monitoring of nitric oxide in diesel exhaust gas by mid-infrared cavity ring-down spectroscopy," *Applied Physics B: Lasers and Optics*, vol. 100, no. 4, pp. 925–931, 2010.

[12] R. Targ, B. C. Steakley, J. G. Hawley, L. L. Ames, P. Forney, D. Swanson, R. Stone, R. G. Otto, V. Zarifis, P. Brockman, R. S. Calloway, S. H. Klein, and P. A. Robinson, "Coherent lidar airborne wind sensor II: flight-test results at 2 and 10 textmu m," *Applied Optics*, vol. 35, no. 36, pp. 7117–7127, 1996.

[13] S. Zlatanovic, J. S. Park, S. Moro, J. M. C. Boggio, I. B. Divliansky, N. Alic, S. Mookherjea, and S. Radic, "Mid-infrared wavelength conversion in silicon waveguides using ultracompact telecom-band-derived pump source," *Nature Photonics*, vol. 4, no. 8, pp. 561–564, 2010.

[14] K. Mansour, A. Ksendzov, P. D. Maker, R. E. Muller, M. J. Manfra, and G. W. Turner, "Single-mode semiconductor reference oscillator development for coherent detection optical remote sensing applications," in *3rd Annual NASA Earth Science Technology Conference*, 2003.

[15] R. A. Sims, C. C. Willis, P. Kadwani, T. S. McComb, L. Shah, V. Sudesh, Z. Roth, M. K. Poutous, E. G. Johnson, and M. Richardson, "Spectral beam combining of 2 µm Tm fiber laser systems," *Optics Communications*, vol. 284, no. 7, pp. 1988 – 1991, 2011.

[16] R. Paschotta, *Encyclopedia of Laser Physics and Technology.* Wiley-VCH Verlag GmbH & Co. KGaA, Germany, 2008.

[17] A. Härkönen, C. Grebing, J. Paajaste, R. Koskinen, J.-P. Alanko, S. Suomalainen, G. Steinmeyer, and M. Guina, "Mode-locked GaSb disk laser producing 384 fs pulses at 2 µm wavelength," *IET Electronics Letters*, vol. 47, no. 7, pp. 454–456, 2011.

[18] H. Q. Le, S. D. Cecca, and A. Mooradian, "Scalable high-power optically pumped GaAs laser," *Applied Physics Letters*, vol. 58, no. 18, pp. 1967–1969, 1991.

[19] W. B. Jiang, S. R. Friberg, H. Iwamura, and Y. Yamamoto, "High powers and subpicosecond pulses from an external-cavity surface-emitting InGaAs/InP multiple quantum-well laser," *Applied Physics Letters*, vol. 58, no. 8, pp. 807 –809, 1991.

[20] M. Kuznetsov, F. Hakimi, R. Sprague, and A. Mooradian, "High-power (>0.5-W CW) diode-pumped vertical-external-cavity surface-emitting semiconductor lasers with circular TEM_{00} beams," *IEEE Photonics Technology Letters*, vol. 9, no. 8, pp. 1063 –1065, 1997.

[21] U. Keller and A. C. Tropper, "Passively modelocked surface-emitting semiconductor lasers," *Physics Reports*, vol. 429, no. 2, pp. 67–120, 2006.

[22] J. E. Hastie, L. G. Morton, A. J. Kemp, M. D. Dawson, A. B. Krysa, and J. S. Roberts, "Tunable ultraviolet output from an intracavity frequency-doubled red vertical-external-cavity surface-emitting laser," *Applied Physics Letters*, vol. 89, no. 6, p. 061114, 2006.

[23] A. Härkönen, "Optically-pumped semiconductor disk lasers for generating visible and infrared radiation," Ph.D. dissertation, Tampere University of Technology, 2008.

[24] S. Giet, H. Sun, S. Calvez, M. Dawson, S. Suomalainen, A. Harkonen, M. Guina, O. Okhotnikov, and M. Pessa, "Spectral narrowing and locking of a vertical-external-cavity surface-emitting laser using an intracavity volume bragg grating," *IEEE Photonics Technology Letters*, vol. 18, no. 16, pp. 1786 –1788, 2006.

[25] T. Leinonen, "The design and fabrication of lasing semiconductor nanostructures employing vertical-cavity geometry," Ph.D. dissertation, Tampere University of Technology, 2007.

[26] M. Rahim, F. Felder, M. Fill, and H. Zogg, "Optically pumped 5 µm IV-VI VECSEL with Al-heat spreader," *Optics Letters*, vol. 33, no. 24, pp. 3010–3012, 2008.

[27] M. Rahim, A. Khiar, F. Felder, M. Fill, and H. Zogg, "4.5 µm wavelength vertical external cavity surface emitting laser operating above room temperature," *Applied Physics Letters*, vol. 94, no. 20, p. 201112, 2009.

[28] M. Rahim, A. Khiar, F. Felder, M. Fill, D. Chappuis, and H. Zogg, "Above Room Temperature Lead Salt VECSELs," *Physics Procedia*, vol. 3, no. 2, pp. 1145–1148, 2010, proceedings of the 14th International conference on Narrow Gap Semiconductors and Systems.

[29] J.-M. Hopkins, N. Hempler, B. Rösener, N. Schulz, M. Rattunde, C. Manz, K. Koehler, J. Wagner, and D. Burns, "5W mid-IR optically pumped semiconductor disk laser," in *Conference on Lasers and Electro-Optics/Quantum Electronics and Laser Science Conference and Photonic Applications Systems Technologies*. Optical Society of America, 2008, p. CWD4.

[30] J. Paajaste, S. Suomalainen, R. Koskinen, A. Härkönen, M. Guina, and M. Pessa, "High-power and broadly tunable GaSb-based optically pumped VECSELs emitting near 2 µm," *Journal of Crystal Growth*, vol. 311, no. 7, pp. 1917 – 1919, 2009.

[31] J.-M. Hopkins, N. Hempler, B. Rösener, N. Schulz, M. Rattunde, C. Manz, K. Köhler, J. Wagner, and D. Burns, "High-power, (AlGaIn)(AsSb) semiconductor disk laser at 2.0 µm," *Optics Letters*, vol. 33, no. 2, pp. 201–203, 2008.

[32] M. Rattunde, J.-M. Hopkins, N. Schulz, B. Rösener, C. Manz, K. Köhler, D.Burns, and J. Wagner, "High-power GaSb-based optically pumped semiconductor disk laser for the 2.X µm wavelength regime," in *Mid-Infrared Optoelectronics: Materials and Devices IX*, 2008.

[33] L. Cerutti, A. Garnache, F. Genty, A. Ouvrard, and C. Alibert, "Low threshold, room temperature laser diode pumped Sb-based VECSEL emitting around 2.1 µm," *Electronics Letters*, vol. 39, no. 3, pp. 290–292, 2003.

[34] B. Rösener, M. Rattunde, R. Moser, C. Manz, K. Köhler, and J. Wagner, "GaSb-based optically pumped semiconductor disk laser using multiple gain elements," *IEEE Photonics Technology Letters*, vol. 21, no. 13, pp. 848 –850, 2009.

[35] B. Rösener, N. Schulz, M. Rattunde, C. Manz, K. Köhler, and J. Wagner, "GaSb-based VECSEL exhibiting multiple-watt output power and high beam quality at a lasing wavelength of 2.25 µm," in *Proceedings of SPIE*, vol. 6997, 2008.

[36] J. Wagner, N. Schulz, M. Rattunde, C. Ritzenthaler, C. Manz, C. Wild, and K. Köhler, "Barrier- and in-well pumped GaSb-based 2.3 µm VECSELs," *Physica status solidi (c)*, vol. 4, no. 5, pp. 1597–1600, 2007.

[37] J.-M. Hopkins, A. J. Maclean, D. Burns, E. Riis, N. Schulz, M. Rattunde, C. Manz, K. Köhler, and J. Wagner, "Tunable, single-frequency, diode-pumped 2.3µm VECSEL," *Optics Express*, vol. 15, no. 13, pp. 8212–8217, 2007.

[38] N. Hempler, J.-M. Hopkins, A. J. Kemp, N. Schulz, M. Rattunde, J. Wagner, M. D. Dawson, and D. Burns, "Pulsed pumping of semiconductor disk lasers," *Optics Express*, vol. 15, no. 6, pp. 3247–3256, 2007.

[39] A. Härkönen, A. Bachmann, S. Arafin, K. Haring, J. Viheriälä, M. Guina, and M.-C. Amann, "2.34-µm electrically pumped VECSEL with buried tunnel junction," in *Semiconductor Lasers and Laser Dynamics IV*, K. Panajotov, M. Sciamanna, A. A. Valle, and R. Michalzik, Eds., vol. 7720, no. 1. SPIE, 2010, p. 772015.

[40] N. Schulz, M. Rattunde, C. Ritzenthaler, B. Rosener, C. Manz, K. Kohler, J. Wagner, and U. Brauch, "Resonant optical in-well pumping of an

(AlGaIn)(AsSb)-based vertical-external-cavity surface-emitting laser emitting at 2.35 µm," *Applied Physics Letters*, vol. 91, no. 9, p. 091113, 2007.

[41] N. Schulz, M. Rattunde, C. Manz, K. Kohler, J. Wagner, J.-M. Hopkins, and D. Burns, "Resonant in-well pumping of GaSb-based VECSELs emitting in the 2.x µm wavelength regime," in *Conference on Lasers and Electro-Optics*, 2007, pp. 1–2.

[42] J. P. van der Ziel, R. J. Malik, J. F. Walker, and R. M. Mikulyak, *Applied Physics Letters*.

[43] T. Hosoda, G. Belenky, L. Shterengas, G. Kipshidze, and M. V. Kisin, "Continuous-wave room temperature operated 3.0 µm type I GaSb-based lasers with quinternary AlInGaAsSb barriers," *Applied Physics Letters*, vol. 92, no. 9, p. 091106, 2008.

[44] L. Shterengas, G. Belenky, T. Hosoda, G. Kipshidze, and S. Suchalkin, "Continuous wave operation of diode lasers at 3.36 µm at 12 °C," *Applied Physics Letters*, vol. 93, no. 1, p. 011103, 2008.

[45] W. Bewley, C. Canedy, M. Kim, C. Kim, J. Nolde, J. Lindle, I. Vurgaftman, and J. Meyer, "Interband cascade laser operating to 269 K at $\lambda = 4.05$ µm," *Electronics Letters*, vol. 43, no. 5, pp. 39–40, 1 2007.

[46] C. L. Canedy, W. W. Bewley, M. Kim, C. S. Kim, J. A. Nolde, D. C. Larrabee, J. R. Lindle, I. Vurgaftman, and J. R. Meyer, "High-temperature interband cascade lasers emitting at $\lambda = 3.6$–4.3 µm," *Applied Physics Letters*, vol. 90, no. 18, p. 181120, 2007.

[47] W. W. Bewley, C. L. Felix, I. Vurgaftman, D. W. Stokes, E. H. Aifer, L. J. Olafsen, J. R. Meyer, M. J. Yang, B. V. Shanabrook, H. Lee, R. U. Martinelli, and A. R. Sugg, "High-temperature continuous-wave 3–6.1 µm W lasers with diamond-pressure-bond heat sinking," *Applied Physics Letters*, vol. 74, no. 8, pp. 1075–1077, 1999.

[48] H. Choi, J. Walpole, G. Turner, M. Conners, L. Missaggia, and M. Manfra, "GaInAsSb-AlGaAsSb tapered lasers emitting at 2.05 µm with 0.6-W diffraction-limited power," *IEEE Photonics Technology Letters*, vol. 10, no. 7, pp. 938–940, 1998.

[49] T. Chiu, J. Zyskind, and W. Tsang, "Molecular beam epitaxial growth of InGaAsSb on (100) GaSb with emission wavelength in the 2 to 2.5 µm range," *Journal of Electronic Materials*, vol. 16, no. 1, pp. 57–61, 1987.

[50] A. Härkönen, J. Rautiainen, L. Orsila, M. Guina, K. Rössner, M. Hümmer, T. Lehnhardt, M. Müller, A. Forchel, M. Fischer, J. Koeth, and O. G. Okhotnikov, "2-µm mode-locked semiconductor disk laser synchronously pumped using an amplified diode laser," *IEEE Photonics Technology Letters*, vol. 20, no. 15, pp. 1332 –1334, 2008.

[51] H. A. Macleod, *Thin-film optical filters*, 3rd ed. Institute of Physics Publishing, 2001.

[52] G. Rempe, R. J. Thompson, H. J. Kimble, and R. Lalezari, "Measurement of ultralow losses in an optical interferometer," *Optics Letters*, vol. 17, no. 5, pp. 363–365, 1992.

[53] P. Savolainen, "Puolijohdelasereiden peilipäätyjen pinnoitus," Master's thesis, Tampere University of Technology, 1992.

[54] A. Garnache, A. Ouvrard, L. Cerutti, D. Barat, A. Vicet, F. Genty, Y. Rouillard, D. Romanini, and E. Cerda-Méndez, "2–2.7µm single frequency tunable Sb-based lasers operating in CW at RT: Microcavity and external cavity VCSELs, DFB," *Proceedings of SPIE*, vol. 6184, pp. 61 840N1–61 840N15, 2006.

[55] H. P. Myers, *Introductory Solid State Physics*, 2nd ed. CRC Press, 2002.

[56] S. Corzine, R. Geels, J. Scott, R.-H. Yan, and L. Coldren, "Design of Fabry-Perot surface-emitting lasers with a periodic gain structure," *IEEE Journal of Quantum Electronics*, vol. 25, no. 6, pp. 1513–1524, 1989.

[57] M. Y. A. Raja, S. R. J. Brueck, M. Osinski, C. F. Schaus, J. G. McInerney, T. M. Brennan, and B. E. Hammons, "Surface-emitting, multiple quantum well GaAs/AlGaAs laser with wavelength-resonant periodic gain medium," *Applied Physics Letters*, vol. 53, no. 18, pp. 1678–1680, 1988.

[58] S. Calvez, J. Hastie, M. Guina, O. Okhotnikov, and M. Dawson, "Semiconductor disk lasers for the generation of visible and ultraviolet radiation," *Laser & Photonics Reviews*, vol. 3, no. 5, pp. 407–434, 2009.

[59] S.-S. Beyertt, M. Zorn, T. Kubler, H. Wenzel, M. Weyers, A. Giesen, G. Trankle, and U. Brauch, "Optical in-well pumping of a semiconductor disk laser with high optical efficiency," *IEEE Journal of Quantum Electronics*, vol. 41, no. 12, pp. 1439–1449, 2005.

[60] A. R. Albrecht, T. J. Rotter, C. P. Hains, A. Stintz, J. V. Moloney, K. J. Malloy, and G. Balakrishnan, "Multi-watt 1.25 µm quantum dot VECSEL," *Electronics Letters*, vol. 46, no. 12, pp. 856–857, 2010.

[61] B. A. Joyce, "Molecular beam epitaxy," *Reports on Progress in Physics*, vol. 48, pp. 1637–1697, 1985.

[62] J. R. Arthur, "Molecular beam epitaxy," *Surface Science*, vol. 500, no. 1–3, pp. 189–217, 2002.

[63] A. E. Siegman, *Lasers*. University Science Books, 1986.

[64] H. Kogelnik and T. Li, "Laser beams and resonators," *Applied Optics*, vol. 5, no. 10, pp. 1550–1567, 1966.

[65] A. Rantamäki, "Towards power scalable short pulse semiconductor disk lasers," Master's thesis, Tampere University of Technology, 2010.

[66] B. E. A. Saleh and M. C. Teich, *Fundamentals of Photonics*. John Wiley & Sons, Inc., 1991.

[67] E. Saarinen, "1 µm picosecond semiconductor lasers with vertical external cavity: Technology and characterization techniques," Master's thesis, Tampere University of Technology, 2005.

[68] A. E. Siegman, "How to (maybe) measure laser beam quality," in *DPSS (Diode Pumped Solid State) Lasers: applications and issues*. Optical Society of America, 1998, p. MQ1.

[69] D. Young, J. Scott, F. Peters, M. Peters, M. Majewski, B. Thibeault, S. Corzine, and L. Coldren, "Enhanced performance of offset-gain high-barrier vertical-cavity surface-emitting lasers," *IEEE Journal of Quantum Electronics*, vol. 29, no. 6, pp. 2013–2022, 1993.

[70] M. Kuznetsov, F. Hakimi, R. Sprague, and A. Mooradian, "Design and characteristics of high-power (>0.5-W CW) diode-pumped vertical-external-cavity surface-emitting semiconductor lasers with circular TEM_{00} beams," *IEEE Journal of Selected Topics in Quantum Electronics*, vol. 5, no. 3, pp. 561–573, 1999.

[71] A. Zakharian, J. Hader, J. Moloney, and S. Koch, "VECSEL threshold and output power-shutoff dependence on the carrier recombination rates," *IEEE Photonics Technology Letters*, vol. 17, no. 12, pp. 2511–2513, 2005.

[72] A. Sugimura, "Band-to-band auger effect in long wavelength multinary III-V alloy semiconductor lasers," *IEEE Journal of Quantum Electronics*, vol. 18, no. 3, pp. 352–363, 1982.

[73] A. Haug, "Auger recombination in quantum well semiconductors: calculation with realistic energy bands," *Semiconductor Science and Technology*, vol. 7, no. 11, pp. 1337–1340, 1992.

[74] M. Silver, E. O'Reilly, and A. Adams, "Determination of the wavelength dependence of auger recombination in long-wavelength quantum-well semiconductor lasers using hydrostatic pressure," *IEEE Journal of Quantum Electronics*, vol. 33, no. 9, pp. 1557–1566, 1997.

[75] A. Kemp, G. Valentine, J.-M. Hopkins, J. Hastie, S. Smith, S. Calvez, M. Dawson, and D. Burns, "Thermal management in vertical-external-cavity surface-emitting lasers: finite-element analysis of a heatspreader approach," *IEEE Journal of Quantum Electronics*, vol. 41, no. 2, pp. 148–155, 2005.

[76] A. Kemp, A. Maclean, J. Hastie, S. Smith, J.-M. Hopkins, S. Calvez, G. Valentine, M. Dawson, and D. Burns, "Thermal lensing, thermal management and transverse mode control in microchip VECSELs," *Applied Physics B: Lasers and Optics*, vol. 83, no. 2, pp. 189–194, 2006.

[77] A. C. Tropper, H. D. Foreman, A. Garnache, K. G. Wilcox, and S. H. Hoogland, "Vertical-external-cavity semiconductor lasers," *Journal of Physics D: Applied Physics*, vol. 37, no. 9, pp. R75–R85, 2004.

[78] E. F. Steigmeier and I. Kudman, "Thermal conductivity of III-V compounds at high temperatures," *Physical Review*, vol. 132, no. 2, pp. 508–512, 1963.

[79] http://www.diemat.com/docs/products/thermals/thermal_properties.php, [Online; accessed 15-March-2011].

[80] H. Morkoç, S. Strite, G. B. Gao, M. E. Lin, B. Sverdlov, and M. Burns, "Large-band-gap SiC, III-V nitride, and II-VI ZnSe-based semiconductor device technologies," *Journal of Applied Physics*, vol. 76, no. 3, pp. 1363–1398, 1994.

[81] G. L. Harris, *Properties of Silicon Carbide (EMIS Datareviews Series)*. INSPEC, U.K., 1995.

[82] T. R. Anthony, W. F. Banholzer, J. F. Fleischer, L. Wei, P. K. Kuo, R. L. Thomas, and R. W. Pryor, "Thermal diffusivity of isotopically enriched ^{12}C diamond," *Physical Review B*, vol. 42, no. 2, pp. 1104–1111, 1990.

[83] Z. L. Liau, "Semiconductor wafer bonding via liquid capillarity," *Applied Physics Letters*, vol. 77, no. 5, pp. 651–653, 2000.

[84] A. M. Zaitsev, *Optical Properties of Diamond: A Data Handbook*. Springer-Verlag Berlin Heidelberg, Germany, 2001.

[85] S. E. Coe and R. S. Sussmann, "Optical, thermal and mechanical properties of CVD diamond," *Diamond and Related Materials*, vol. 9, no. 9–10, pp. 1726–1729, 2000.

[86] J. Chilla, S. Butterworth, A. Zeitschel, J. Charles, A. Caprara, M. Reed, and L. Spinelli, "High power optically pumped semiconductor lasers." in *Proceedings of SPIE*, vol. 5332, 2004, p. 8.

[87] B. Rudin, A. Rutz, D. J. Maas, A.-R. Bellancourt, E. Gini, T. Südmeyer, and U. Keller, "Efficient high-power VECSEL generates 20 W continuous-wave radiation in a fundamental transverse mode," in *Advanced Solid-State Photonics*, 2009, p. ME2.

[88] T.-L. Wang, Y. Kaneda, J. Yarborough, J. Hader, J. Moloney, A. Chernikov, S. Chatterjee, S. Koch, B. Kunert, and W. Stolz, "High-power optically pumped semiconductor laser at 1040 nm," *IEEE Photonics Technology Letters*, vol. 22, no. 9, pp. 661–663, 2010.

[89] A. R. Lang, "Causes of birefringence in diamond," *Nature*, vol. 213, no. 5073, pp. 248–251, 1967.

[90] F. van Loon, A. J. Kemp, A. J. Maclean, S. Calvez, J.-M. Hopkins, J. E. Hastie, M. D. Dawson, and D. Burns, "Intracavity diamond heatspreaders in lasers: the effects of birefringence," *Optics Express*, vol. 14, no. 20, pp. 9250–9260, 2006.

[91] E. Hecht, *Optics*, 4th ed. Addison Wesley, San Fransisco, USA, 2002.

[92] K. Gardner, R. Abram, and E. Riis, "A birefringent etalon as single-mode selector in a laser cavity," *Optics Express*, vol. 12, no. 11, pp. 2365–2370, 2004.

[93] L. Fan, M. Fallahi, A. Zakharian, J. Hader, J. Moloney, R. Bedford, J. Murray, W. Stolz, and S. Koch, "Extended tunability in a two-chip VECSEL," *IEEE Photonics Technology Letters*, vol. 19, no. 8, pp. 544–546, 2007.

[94] K. S. Gardner, "Single frequency vertical external cavity surface emitting lasers," Ph.D. dissertation, Department of Physics, University of Strathclyde, 2007.

[95] A. Kemp, J.-M. Hopkins, A. Maclean, N. Schulz, M. Rattunde, J. Wagner, and D. Burns, "Thermal management in 2.3-µm semiconductor disk lasers: A finite element analysis," *IEEE Journal of Quantum Electronics*, vol. 44, no. 2, pp. 125–135, 2008.

[96] A. Garnache, A. Ouvrard, and D. Romanini, "Single-frequency operation of external-cavity VCSELs: Non-linear multimode temporal dynamics and quantum limit." *Optics Express*, vol. 15, no. 15, pp. 9403–9417, 2007.

[97] M. Born and E. Wolf, *Principles of optics: electromagnetic theory of propagation, interference and diffraction of light*, 7th ed. Cambridge University Press, U.K., 1999.

[98] M. C. Y. Huang, Y. Zhou, and C. J. Chang-Hasnain, "A surface-emitting laser incorporating a high-index-contrast subwavelength grating," *Nature Photonics*, vol. 1, no. 2, pp. 119–122, 2007.

[99] D. Fattal, J. Li, Z. Peng, M. Fiorentino, and R. G. Beausoleil, "Flat dielectric grating reflectors with focusing abilities," *Nature Photonics*, vol. 4, pp. 466–470, 2010.

[100] S. Giet, C.-L. Lee, S. Calvez, M. D. Dawson, N. Destouches, J.-C. Pommier, and O. Parriaux, "Stabilization of a semiconductor disk laser using an intracavity high reflectivity grating," *Optics Express*, vol. 15, no. 25, pp. 16 520–16 526, 2007.

[101] A. Mehta, R. Rumpf, Z. Roth, and E. Johnson, "Guided mode resonance filter as a spectrally selective feedback element in a double-cladding optical fiber laser," *IEEE Photonics Technology Letters*, vol. 19, no. 24, pp. 2030–2032, 2007.

[102] J. M. Kontio, J. Simonen, K. Leinonen, M. Kuittinen, and T. Niemi, "Broadband infrared mirror using guided-mode resonance in a subwavelength germanium grating," *Optics Letters*, vol. 35, no. 15, pp. 2564–2566, 2010.

[103] H. W. Icenogle, B. C. Platt, and W. L. Wolfe, "Refractive indexes and temperature coefficients of germanium and silicon," *Applied Optics*, vol. 15, no. 10, pp. 2348–2351, 1976.

[104] S. S. Wang and R. Magnusson, "Theory and applications of guided-mode resonance filters," *Applied Optics*, vol. 32, no. 14, pp. 2606–2613, 1993.

[105] R. Magnusson and S. Wang, "Resonance properties of dielectric waveguide gratings: theory and experiments at 4-18 GHz," *Applied Physics Letters*, vol. 61, no. 9, pp. 1022–1024, Apr. 1992.

[106] D. Marcuse, *Theory of dielectric optical waveguides*, 2nd ed. Academic Press, Boston, USA, 1991.

[107] D. Rosenblatt, A. Sharon, and A. Friesem, "Resonant grating waveguide structures," *IEEE Journal of Quantum Electronics*, vol. 33, no. 11, pp. 2038 –2059, Nov. 1997.

[108] T. Tamir, "Leaky waves in planar optical waveguides," *Nouvelle Revue d'Optique*, vol. 6, no. 5, pp. 273–284, 1975.

[109] S. S. Wang, R. Magnusson, J. S. Bagby, and M. G. Moharam, "Guided-mode resonances in planar dielectric-layer diffraction gratings," *Journal of the Optical Sociecty of America A*, vol. 7, no. 8, pp. 1470–1474, 1990.

[110] Y. Ding and R. Magnusson, "Resonant leaky-mode spectral-band engineering and device applications," *Optics Express*, vol. 12, no. 23, pp. 5661–5674, 2004.

[111] R. Magnusson and M. Shokooh-Saremi, "Physical basis for wideband resonant reflectors," *Optics Express*, vol. 16, no. 5, pp. 3456–3462, 2008.

[112] P. Smith, "Mode-locking of lasers," *Proceedings of the IEEE*, vol. 58, no. 9, pp. 1342–1357, 1970.

[113] H. Haus, "Mode-locking of lasers," *IEEE Journal of Selected Topics in Quantum Electronics*, vol. 6, no. 6, pp. 1173–1185, 2000.

[114] C. Rulliére, Ed., *Femtosecond Laser Pulses*, 2nd ed. Springer Science+Business Media, Inc., 2005.

[115] L. Cohen, "Generalization of the Wiener-Khinchin theorem," *IEEE Signal Processing Letters*, vol. 5, no. 11, pp. 292–294, 1998.

[116] V. Matsas, T. Newson, D. Richardson, and D. Payne, "Selfstarting passively mode-locked fibre ring soliton laser exploiting nonlinear polarisation rotation," *Electronics Letters*, vol. 28, no. 15, pp. 1391–1393, 1992.

[117] M. E. Fermann, M. J. Andrejco, Y. Silberberg, and M. L. Stock, "Passive mode locking by using nonlinear polarization evolution in a polarization-maintaining erbium-doped fiber," *Optics Letters*, vol. 18, no. 11, pp. 894–896, 1993.

[118] I. N. Duling III, "All-fiber ring soliton laser mode locked with a nonlinear mirror," *Optics Letters*, vol. 16, no. 8, pp. 539–541, 1991.

[119] D. Richardson, R. Laming, D. Payne, V. Matsas, and M. Phillips, "Self-starting, passively modelocked erbium fibre ring laser based on the amplifying Sagnac switch," *Electronics Letters*, vol. 27, no. 6, pp. 542 –544, 1991.

[120] U. Keller, D. A. B. Miller, G. D. Boyd, T. H. Chiu, J. F. Ferguson, and M. T. Asom, "Solid-state low-loss intracavity saturable absorber for Nd:YLF lasers: an antiresonant semiconductor Fabry–Pérot saturable absorber," *Optics Letters*, vol. 17, no. 7, pp. 505–507, 1992.

[121] D. Lorenser, H. Unold, D. Maas, A. Aschwanden, R. Grange, R. Paschotta, D. Ebling, E. Gini, and U. Keller, "Towards wafer-scale integration of high repetition rate passively mode-locked surface-emitting semiconductor lasers," *Applied Physics B: Lasers and Optics*, vol. 79, no. 8, pp. 927–932, 2004.

[122] C. E. Soccolich, M. N. Islam, M. G. Young, and B. I. Miller, "Bulk semiconductor saturable absorber for a NaCl color center laser," *Applied Physics Letters*, vol. 56, no. 22, pp. 2177–2179, 1990.

[123] L. Brovelli, I. Jung, D. Kopf, M. Kamp, M. Moser, F. Kartner, and U. Keller, "Self-starting soliton modelocked Ti-sapphire laser using a thin semiconductor saturable absorber," *Electronics Letters*, vol. 31, no. 4, pp. 287 –289, 1995.

[124] U. Keller and T. Chiu, "Resonant passive mode-locked Nd:YLF laser," *IEEE Journal of Quantum Electronics*, vol. 28, no. 7, pp. 1710–1721, 1992.

[125] S. C. Zeller, R. Grange, V. Liverini, A. Rutz, S. Schön, M. Haiml, U. Keller, S. Pawlik, and B. Schmidt, "A low-loss buried resonant GaInNAs SESAM for 1.3-µm Nd:YLF laser at 1.4 GHz," in *Advanced Solid-State Photonics*, 2006, p. TuA6.

[126] M. Guina, N. Xiang, and O. Okhotnikov, "Stretched-pulse fiber lasers based on semiconductor saturable absorbers," *Applied Physics B: Lasers and Optics*, vol. 74, pp. S193–S200, 2002.

[127] M. Guina, "Absorptive semiconductor reflectors for controlling dynamic properties of fiber lasers," Ph.D. dissertation, Tampere University of Technology, 2002.

[128] U. Keller, K. Weingarten, F. Kartner, D. Kopf, B. Braun, I. Jung, R. Fluck, C. Honninger, N. Matuschek, and J. Aus der Au, "Semiconductor saturable absorber mirrors (SESAM's) for femtosecond to nanosecond pulse generation

in solid-state lasers," *IEEE Journal of Selected Topics in Quantum Electronics*, vol. 2, no. 3, pp. 435–453, 1996.

[129] R. Paschotta and U. Keller, "Passive mode locking with slow saturable absorbers," *Applied Physics B: Lasers and Optics*, vol. 73, no. 7, pp. 653–662, 2001.

[130] E. L. Delpon, J. L. Oudar, N. Bouche, R. Raj, A. Shen, N. Stelmakh, and J. M. Lourtioz, "Ultrafast excitonic saturable absorption in ion-implanted InGaAs/InAlAs multiple quantum wells," *Applied Physics Letters*, vol. 72, no. 7, pp. 759–761, 1998.

[131] S. Gupta, J. Whitaker, and G. Mourou, "Ultrafast carrier dynamics in III-V semiconductors grown by molecular-beam epitaxy at very low substrate temperatures," *IEEE Journal of Quantum Electronics*, vol. 28, no. 10, pp. 2464–2472, 1992.

[132] S. Suomalainen, A. Vainionpää, O. Tengvall, T. Hakulinen, S. Karirinne, M. Guina, O. G. Okhotnikov, T. G. Euser, and W. L. Vos, "Long-wavelength fast semiconductor saturable absorber mirrors using metamorphic growth on GaAs substrates," *Applied Physics Letters*, vol. 87, no. 12, p. 121106, 2005.

[133] J. Gopinath, E. Thoen, E. Koontz, M. Grein, L. Kolodziejski, E. Ippen, and J. Donnelly, "Ultrafast recovery times in implanted semiconductor saturable absorber mirrors at 1.5 µm," in *Conference on Lasers and Electro-Optics*, 2001, pp. CWI4–1–CW4–3.

[134] U. Siegner, R. Fluck, G. Zhang, and U. Keller, "Ultrafast high-intensity nonlinear absorption dynamics in low-temperature grown gallium arsenide," *Applied Physics Letters*, vol. 69, no. 17, pp. 2566–2568, 1996.

[135] L. Gomes, "Ultrafast ytterbium fiber sources based on SESAM technology," Ph.D. dissertation, Tampere University of Technology, 2006.

[136] S. Kivistö, "Short pulse lasers using advanced fiber technology and saturable absorbers," Ph.D. dissertation, Tampere University of Technology, 2010.

[137] U. Keller, "Recent developments in compact ultrafast lasers," *Nature*, vol. 424, pp. 831–838, 2003.

[138] R. Grange, M. Haiml, R. Paschotta, G. Spühler, L. Krainer, M. Golling, O. Ostinelli, and U. Keller, "New regime of inverse saturable absorption for self-stabilizing passively mode-locked lasers," *Applied Physics B: Lasers and Optics*, vol. 80, no. 2, pp. 151–158, 2005, 10.1007/s00340-004-1622-3.

[139] R. Paschotta, *Field Guide to Laser Pulse Generation.* SPIE Press, Bellingham, WA, 2008.

[140] L. E. Hargrove, R. L. Fork, and M. A. Pollack, "Locking of He-Ne laser modes induced by synchronous intracavity modulation," *Applied Physics Letters*, vol. 5, no. 1, pp. 4–5, 1964.

[141] R. W. Boyd, *Nonlinear Optics*, 2nd ed. Academic press, 2003.

[142] C. R. Hugget, "Mode-locking of CW lasers by regenerative RF feedback," *Applied Physics Letters*, vol. 13, no. 5, pp. 186–187, 1968.

[143] P. M. W. French, "The generation of ultrashort laser pulses," *Reports on Progress in Physics*, vol. 58, no. 2, p. 169, 1995.

[144] C. Spielmann, F. Krausz, T. Brabec, E. Wintner, and A. J. Schmidt, "Femtosecond pulse generation from a synchronously pumped Ti:sapphire laser," *Optics Letters*, vol. 16, no. 15, pp. 1180–1182, 1991.

[145] W. H. Xiang, S. R. Friberg, K. Watanabe, S. Machida, Y. Sakai, H. Iwamura, and Y. Yamamoto, "Sub-100 femtosecond pulses from an external-cavity surface-emitting InGaAs/InP multiple quantum well laser with soliton-effect compression," *Applied Physics Letters*, vol. 59, no. 17, pp. 2076–2078, 1991.

[146] F. J. McClung and R. W. Hellwarth, "Giant optical pulsations from ruby," *Applied Optics*, vol. 1, no. S1, pp. 103–105, 1962.

[147] A. Fragemann, V. Pasiskevicius, and F. Laurell, "Optical parametric amplification of a gain-switched picosecond laser diode," *Optics Express*, vol. 13, no. 17, pp. 6482–6489, 2005.

[148] J.-M. Hopkins, N. Hempler, A. Kemp, B. Rösener, N. Schulz, M. Rattunde, J. Wagner, and D. Burns, "High-power, pulsed-pumped, 2.0 µm & 2.3 µm semiconductor disk lasers," in *Mid-Infrared Optoelectronics: Materials and Devices IX*, 2008.

[149] J. A. Armstrong, "Measurement of picosecond laser pulse widths," *Applied Physics Letters*, vol. 10, no. 1, pp. 16–18, 1967.

[150] F. Quercioli, B. Tiribilli, M. Vassalli, and F. Sbrana, "Autocorrelator designs for nonlinear optical microscopy," *Optical Engineering*, vol. 45, no. 6, p. 064303, 2006.

[151] A. Miller, D. T. Reid, and D. M. Finlayson, Eds., *Ultrafast Photonics.* Taylor & Francis, 2004.

[152] D. T. Reid, M. Padgett, C. McGowan, W. E. Sleat, and W. Sibbett, "Light-emitting diodes as measurement devices for femtosecond laser pulses," *Optics Letters*, vol. 22, no. 4, pp. 233–235, 1997.

[153] A. Gutierrez, P. Dorn, J. Zeller, D. King, L. F. Lester, W. Rudolph, and M. Sheik-Bahae, "Autocorrelation measurement of femtosecond laser pulses by use of a ZnSe two-photon detector array," *Optics Letters*, vol. 24, no. 16, pp. 1175–1177, 1999.

[154] E. Power, J. Pentland, J. Nees, C. P. Hauri, M. Merano, R. Lopez-Martens, and G. Mourou, "All-reflective high fringe contrast autocorrelator for measurement of ultrabroadband optical pulses," *Optics Letters*, vol. 31, no. 23, pp. 3514–3516, 2006.

[155] J. M. Roth, T. E. Murphy, and C. Xu, "Ultrasensitive and high-dynamic-range two-photon absorption in a GaAs photomultiplier tube," *Optics Letters*, vol. 27, no. 23, pp. 2076–2078, 2002.

[156] R. Ramaswami and K. N. Sivarajan, *Optical Networks: A Practical perspective*, 2nd ed. Morgan Kaufmann Publishers, 2002.

[157] G. P. Agrawal, *Fiber-Optic Communication Systems*, 3rd ed. John Wiley & Sons, Inc., 2002.

[158] "Corning® SMF-28™ optical fiber product information," http://www.photonics.byu.edu/FiberOpticConnectors.parts/images/smf28.pdf, [Online; accessed 21-May-2011].

[159] T. Miya, Y. Terunuma, T. Hosaka, and T. Miyashita, "Ultimate low-loss single-mode fibre at 1.55 µm," *Electronics Letters*, vol. 15, no. 4, pp. 106–108, 15 1979.

[160] F. Mitschke, *Fiber Optics: Physics and Technology.* Springer-Verlag Berlin Heidelberg, 2009.

[161] A. Härkönen, J. Paajaste, S. Suomalainen, J.-P. Alanko, C. Grebing, R. Koskinen, G. Steinmeyer, and M. Guina, "Picosecond passively mode-locked GaSb-based semiconductor disk laser operating at 2 µm," *Optics Letters*, vol. 35, no. 24, pp. 4090–4092, 2010.

[162] *MP 35E User Manual M-405 / M-410 / M-415 Series Linear Positioning Stages*, 3.3.3 ed., Physik Instrumente (PI) GmbH & Co. KG, Germany, 2008.

[163] "Newport UBBR2.5-1I Retroreflector specifications," http://search.newport.com/?q=*&x2=sku&q2=UBBR2.5-1I, [Online; accessed 6-April-2011].

[164] M. Kuznetsov, *Semiconductor disk lasers, Chapter 1: VECSEL semiconductor lasers: a path to high-power, quality beam and UV to IR wavelength by design*, O. G. Okhotnikov, Ed. WILEY-VCH Verlag GmbH & Co. KGaA Weinheim Germany, 2010.

[165] P. S. Zory, *Quantum well lasers (quantum electronics principles and applications)*. Academic Press, Inc., 1993.

[166] E. J. Saarinen, J. Lyytikäinen, and O. G. Okhotnikov, "Hysteresis and multiple pulsing in a semiconductor disk laser with a saturable absorber," *Physical Review E*, vol. 78, no. 1, p. 016207, 2008.

[167] J.-P. Alanko, C. Grebing, J. Paajaste, R. Koskinen, S. Suomalainen, A. Härkönen, G. Steinmeyer, and M. Guina, "430-fs pulses from a SESAM mode-locked GaSb disk laser emitting at 2 µm," in *Conference on Lasers and Electro-Optics*, 2011.

[168] H. Dyball, "GaSb lasers get pulses racing," *Electronics Letters*, vol. 47, no. 7, pp. 419–419, 2011.

APPENDIX A: GAIN MIRROR STRUCTURES USED IN THIS WORK

Comp	x(In)	x(Al)	n @ 2300 nm	OPL (nm)	d (nm)
		x 1 time			
GaSb cap	0,0 %	0,0 %	3,897	116,90	30,00
$Al_{0.85}Ga_{0.15}AsSb$ window	0,0 %	85,0 %	3,227	419,52	130,00
$Al_{0.30}Ga_{0.70}Sb$ barrier outer 2	0,0 %	30,2 %	3,589	520,98	145,17
$In_{0.35}Ga_{0.65}AsSb$ QW	35,0 %	0,0 %	3,780	37,80	10,00
$Al_{0.30}Ga_{0.70}Sb$ barrier	0,0 %	30,2 %	3,589	35,89	10,00
$In_{0.35}Ga_{0.65}AsSb$ QW	35,0 %	0,0 %	3,780	37,80	10,00
$Al_{0.30}Ga_{0.70}Sb$ barrier	0,0 %	30,2 %	3,589	35,89	10,00
$In_{0.35}Ga_{0.65}AsSb$ QW	35,0 %	0,0 %	3,780	37,80	10,00
		x 2 times			
$Al_{0.30}Ga_{0.70}Sb$ barrier THICK	0,0 %	30,2 %	3,589	964,84	268,85
$In_{0.35}Ga_{0.65}AsSb$ QW	35,0 %	0,0 %	3,780	37,80	10,00
$Al_{0.30}Ga_{0.70}Sb$ barrier	0,0 %	30,2 %	3,589	35,89	10,00
$In_{0.35}Ga_{0.65}AsSb$ QW	35,0 %	0,0 %	3,780	37,80	10,00
$Al_{0.30}Ga_{0.70}Sb$ barrier	0,0 %	30,2 %	3,589	35,89	10,00
$In_{0.35}Ga_{0.65}AsSb$ QW	35,0 %	0,0 %	3,780	37,80	10,00
		x 1 time			
Al0.30Ga0.70Sb barrier outer 1	0,0 %	30,2 %	3,589	1057,43	294,65
AlAsSb DBR	0,0 %	100,0 %	3,163	575,00	181,77
		x 21 times			
GaSb DBR	0,0 %	0,0 %	3,897	575,00	147,56
AlAsSb DBR	0,0 %	100,0 %	3,163	575,00	181,77
		x 1 time			
GaSb buffer	0,0 %	0,0 %	3,897	389,66	100,00
n-GaSb substrate					500 µm

Figure A.1: Structure of the 2.35 µm gain mirror.

Comp	x(In)	x(Al)	n @ 2000 nm	OPL (nm)	d (nm)
		x 1 time			
GaSb cap	0,0 %	0,0 %	3,965	118,94	30,00
AlAsSb cladding	0,0 %	100,0 %	2,903	381,07	131,25
GaSb barrier outer	0,0 %	0,0 %	3,965	912,69	230,21
InGaSb QW	21,9 %	0,0 %	3,972	31,78	8,00
GaSb barrier	0,0 %	0,0 %	3,965	39,65	10,00
InGaSb QW	21,9 %	0,0 %	3,972	31,78	8,00
GaSb barrier	0,0 %	0,0 %	3,965	39,65	10,00
InGaSb QW	21,9 %	0,0 %	3,972	31,78	8,00
		x 4 times			
GaSb barrier thick	0,0 %	0,0 %	3,965	825,37	208,19
InGaSb QW	21,9 %	0,0 %	3,972	31,78	8,00
GaSb barrier	0,0 %	0,0 %	3,965	39,65	10,00
InGaSb QW	21,9 %	0,0 %	3,972	31,78	8,00
GaSb barrier	0,0 %	0,0 %	3,965	39,65	10,00
InGaSb QW	21,9 %	0,0 %	3,972	31,78	8,00
		x 1 time			
GaSb barrier outer	0,0 %	0,0 %	3,965	912,69	230,21
AlAsSb DBR	0,0 %	100,0 %	2,903	500,00	172,21
		x 18 times			
GaSb DBR	0,0 %	0,0 %	3,965	490,20	123,65
AlAsSb DBR	0,0 %	100,0 %	2,903	490,21	168,84
		x 1 time			
GaSb buffer	0,0 %	0,0 %	3,965	396,45	100,00
n-GaSb substrate					500 µm

Figure A.2: Structure of the 2.0 µm gain mirror.

APPENDIX B: SESAM STRUCTURE USED IN THIS WORK

Comp	x(In)	x(Al)	n	OPL (nm)	d (nm)
		x 1 time			
GaSb barrier thick 2	0,0 %	0,0 %	3,965	1195,11	301,45
InGaSb QW	29,0 %	0,0 %	3,975	31,80	8,00
GaSb barrier	0,0 %	0,0 %	3,965	39,65	10,00
InGaSb QW	29,0 %	0,0 %	3,975	31,80	8,00
GaSb barrier	0,0 %	0,0 %	3,965	39,65	10,00
InGaSb QW	29,0 %	0,0 %	3,975	31,80	8,00
GaSb barrier thick 1	0,0 %	0,0 %	3,965	912,66	230,21
AlAsSb DBR	0,0 %	100,0 %	2,903	490,20	168,84
		x 18 times			
GaSb DBR	0,0 %	0,0 %	3,965	490,21	123,65
AlAsSb DBR	0,0 %	100,0 %	2,903	490,20	168,84
		x 1 time			
GaSb buffer	0,0 %	0,0 %	3,965	396,45	100,00
p-GaSb substrate					500 µm

Figure B.1: Structure of the SESAM with three quantum wells.